FORWARD CHARGE DISTRIBUTIONS ASSOCIATED WITH HADRONICALLY PRODUCED J/PSI PARTICLES

BY

HOWARD SCOTT BUDD

B. S., Pennsylvania State University, 1971
B. S., Pennsylvania State University, 1971
M. S., University of Illinois, 1972

THESIS

Submitted in partial fulfillment of the requirements
for the degree of Doctor of Philosophy in Physics
in the Graduate College of the
University of Illinois at Urbana-Champaign, 1983

Urbana, Illinois

PACS 13.90.+i

FORWARD CHARGE DISTRIBUTIONS ASSOCIATED WITH HADRONICALLY PRODUCED J/PSI PARTICLES

Howard Scott Budd, Ph. D.
Department of Physics
University of Illinois at Urbana-Champaign, 1983

We have measured the forward charge as a function of x_F of the psi for events produced by 225 Gev/c π^- Be interactions. The forward charge is the average difference between the number of positive hadrons and negative hadrons produced in the forward hemisphere. The standard Drell-Yan model predicts that the forward charge should become less negative as the x_F of the J/psi increases. The measured forward charge becomes more negative as the x_F of the J/psi increases although it is consistent with being flat as a function of x_F. Hence, the data is not consistent with any Drell-Yan type model which assumes the forward charge is not strongly dependent on the hadronic energy left over after the J/psi is formed.

ACKNOWLEDGEMENTS

This experiment would not have been possible without the accelerator personnel at Fermilab. I would like to thank the people of the Neutrino Department who gave the support necessary for Experiment 610 to run. I would like to thank all the collaborators of E610. In particular, I would like to individually thank the people listed below.

I would like to thank my advisor, Professor Louis Koester, for the advice, help, and encouragement he has given me in my graduate studies.

I would like to thank Professor Ulrich Kruse from whom I learned a great deal about building equipment.

I would also like to thank the Professors Lee Holloway and Robert Sard for their advice during the running and analysis of the experiment. Special thanks go to the Illinois graduate students on the experiment: Tom Graff, Pat Lukens, Steve Hahn, and Paul Schoessow. They were very helpful in both the setting up and analysis of the experiment.

I would also like to thank the following people on E610: Dan Bauer, John W. Cooper, Tom Kirk, Steven Pordes and Rajendran Raja.

The University of Illinois High Energy Group provides excellent facilities for analyzing data. I would like to thank Jerry Wray and David Lesny for making the facilities here user oriented.

I would like to thank Professor Lorella Jones for theoretical discussions involving the data.

I would like to thank the secretaries at Illinois, especially Dorothy Schoeps, for arranging many of the details involving

transportation and housing.

This thesis is dedicated to my parents Edward and Margaret Budd for the love and support they have shown me.

The work presented in this thesis was supported in part by the U.S. Department of Energy under Grant DE-AC02-76ER01195.

TABLE OF CONTENTS

1. INTRODUCTION 1

2. THEORY 2

3. APPARATUS 23

3.1 Beam 23

3.2 Beam Chambers and Hodoscopes 23

3.3 Beam Veto Counters 27

3.4 Target and Target Counters 27

3.5 80 cm Chambers 29

3.6 Chicago Cyclotron Magnet 29

3.7 University of Illinois Chambers 30

3.8 Drift Chambers 31

3.9 Hadron Hodoscope 32

3.10 Rochester Steel 32

3.11 Muon Hodoscope 34

3.12 Dimuon Trigger 34

4. ANALYSIS 37

4.1 Alignment 37

4.2 Beam Reconstruction 40

4.3 Vertex Finding 41

4.4 Upstream Trackfinding (Straight Line) 42

4.5 Downstream Trackfinding (Curved Tracks) 43

4.6 Determining Track Parameters 49

4.7 Muon Identification 52

4.8 Final J/psi Sample 53

5. RESULTS AND CONCLUSION 57

5.1 J/psi Events 58

5.2 Feynman X Dependence 58

5.3 Measurement of Forward Charge 62

5.4 Data 65

5.5 Decay from Higher Lying States 78

5.6 Comparison with WA11 79

5.7 Calculation of Forward Charge for the Four Bins ... 81

5.8 Failure of Drell-Yan Formalism 86

5.9 Conclusion 88

APPENDICES

A. TRACKFINDING 90

A.1 X Predicting Scheme 90

A.2 Vertical Focusing 98

A.3 Downstream Trackfinding 99

A.4 Weeding 103

A.5 Track Fitting 106

B. TRACKFINDING EFFICIENCY 108

C. MONTE CARLO PROGRAM 113

D. CHAMBER AND H HODOSCOPE EFFICIENCY 118

D.1 MWPC Efficiencies 118

D.2 Drift chamber efficiency 122

D.3 Efficiency of H Hodoscope 125

E. STANDARD TRACK TECHNIQUE 128

F. UNIVERSITY OF ILLINOIS MWPCS 131

F.1 Description of the Frames and Wire Planes 131

F.2 Support Wire 135

F.3 Prestressing 142

F.4 Winding 145

5.2 Feynman X Dependence 58

5.3 Measurement of Forward Charge 62

5.4 Data 65

5.5 Decay from Higher Lying States 78

5.6 Comparison with WA11 79

5.7 Calculation of Forward Charge for the Four Bins ... 81

5.8 Failure of Drell-Yan Formalism 86

5.9 Conclusion 88

APPENDICES

A. TRACKFINDING 90

A.1 X Predicting Scheme 90

A.2 Vertical Focusing 98

A.3 Downstream Trackfinding 99

A.4 Weeding 103

A.5 Track Fitting 106

B. TRACKFINDING EFFICIENCY 108

C. MONTE CARLO PROGRAM 113

D. CHAMBER AND H HODOSCOPE EFFICIENCY 118

D.1 MWPC Efficiencies 118

D.2 Drift chamber efficiency 122

D.3 Efficiency of H Hodoscope 125

E. STANDARD TRACK TECHNIQUE 128

F. UNIVERSITY OF ILLINOIS MWPCS 131

F.1 Description of the Frames and Wire Planes 131

F.2 Support Wire 135

F.3 Prestressing 142

F.4 Winding 145

F.5 Gluing 146

F.6 Cleaning 147

F.7 Flattening 148

F.8 Sealing 149

F.9 Chamber Operations 149

G. EQUIPMENT FILE 151

REFERENCES 164

VITA 166

CHAPTER 1

INTRODUCTION

The data used for this thesis were obtained during Experiment 610 with the Chicago Cyclotron Spectrometer at Fermilab. The experiment was carried out by a group of about 30 people from University of Illinois, Fermilab, University of Pennsylvania, Purdue University, and Tufts University.

The purpose of the experiment was to study the hadronic production of chi particles by their decay into $\psi\gamma$. To do this we used a 225 Gev/c π^- beam on a beryllium target. We triggered on a large angle muon pair. Unlike many dimuon experiments, there was no beam dump immediately downstream of the target. The open spectrometer enabled us to look at all particles produced in association with the J/psi, which is the subject of this thesis. For a discussion of the χ particles see the thesis of S. Hahn[1].

This thesis deals with what the forward-going charge can tell us about the J/psi production mechanism. The forward going charge is the average difference between the number of positive particles and negative particles produced in the forward hemisphere. Different theories of J/psi production predict different numbers for the forward going charge.

CHAPTER 2

THEORY

In 1974 a narrow resonant state, J/ψ, was found at both Brookhaven [2] and SLAC [3]. This state was produced by protons on a beryllium target at Brookhaven and by e^+e^- at SLAC. The J/ψ was determined to be a new vector meson with odd G parity and isospin 0.

The early information about the J/psi was obtained in e^+e^- collisions. These studies showed that the J/psi was made up of a new kind of quark and antiquark, which had been postulated earlier by theorists who felt that there should be a symmetry between the number of leptons and the number of quarks. This new quark "flavor" was called charm. The large mass of the charmed quark allowed theorists to use nonrelativistic quantum mechanics to calculate other $c\bar{c}$ states which were analogous to the various spin-orbital states of the hydrogen atom. Figure 2.1 lists these states along with their quantum numbers and their decay rates into other $c\bar{c}$ states or muons. Agreement between the theoretical prediction for these states and the experimental numbers, such as mass and width observed in e^+e^- collision experiments, confirms the fact that the J/psi is made up of a $c\bar{c}$ pair.

Our purpose for doing a J/psi experiment with a pion beam is to determine how the J/psi is produced hadronically. Many of the intrinsic properties of the J/psi are already known. It is hoped that J/psi production can be explained in terms of quantum chromodynamics, QCD, the only theory of the strong interaction.

Quantum chromodynamics assumes that hadrons are made up of spin 1/2 fermions called quarks which interact via spin 1 vector particles

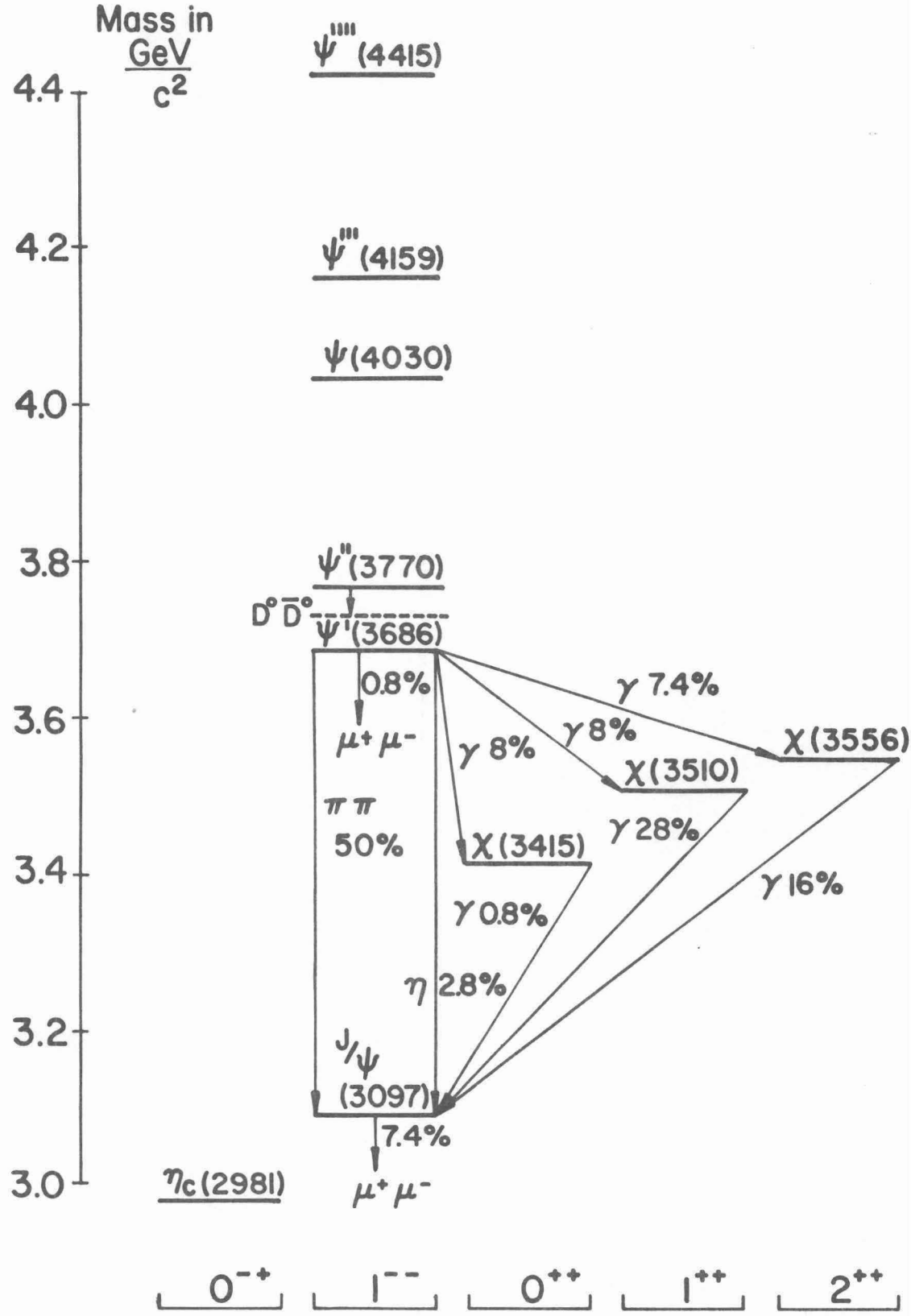

Figure 2.1
Charmonium spectrum

called gluons. The gluons propagate the force between particles which carry a quantum number called color. This theory is analogous to quantum electrodynamics where the electrons interact via photons. The photons are exchanged between particles which carry charge. One of the main differences between QCD and QED is that gluons carry color. Hence, they can interact among themselves. Experiments on deep inelastic scattering of leptons by hadrons indicate the existence of quarks. They also show that half the momentum of hadrons is carried by uncharged constituents, presumably gluons.

The models describing J/psi production are based on the generalized Drell-Yan model. The Drell-Yan model [4] explains the production of high mass, nonresonance, lepton pairs in hadronic interactions, (see Figure 2.2). The Drell-Yan model states that a quark from one hadron fuses with an antiquark from another hadron to form a virtual photon. This virtual photon decays into a lepton pair. We can write down the cross section for the production of these lepton pairs as:

$$\frac{d\sigma}{dq^2} = \left(\frac{4\pi\alpha^2}{3q^4}\right)\int_0^1 dx_1 \int_0^1 dx_2\, \delta\left(x_1 x_2 - \frac{q^2}{s}\right) \sum_{i=u,d,s} Q_i^2 F_i(x_1)\, \overline{F}_i(x_2)$$

where

1. q^2 is the invariant mass squared of the lepton pair.

2. x_1 (x_2) is the fraction of longitudinal momentum that quark 1 (2) is carrying in hadron 1 (2).

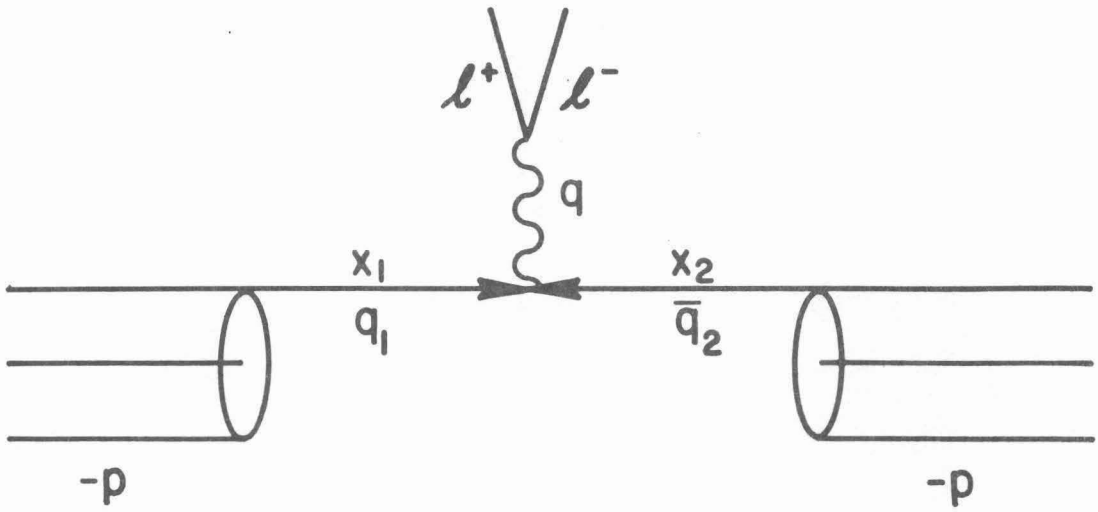

Figure 2.2
Production of Drell-Yan pairs by qq annihilation

3. Q_i is the charge of the quark of type i.

4. $F_i(x_1)$ is the momentum distribution for a quark of type i in hadron 1.

5. $\bar{F}_i(x_2)$ is the momentum distribution for an antiquark of type i in hadron 2. F and $\bar{F}$ can be calculated from deep inelastic lepton scattering.

6. α is the fine structure constant.

7. $\frac{4\pi\alpha^2}{3q^4}$ is a term from QED which gives $\left(\frac{d\sigma}{dq^2}\right)_{q\bar{q}\to\gamma\to\mu^+\mu^-}$

8. The double integral gives the probability a quark from one hadron and an antiquark from the other hadron meet with the right q^2.

The Drell-Yan model gives a good description of the Feynman x distribution and energy dependence of the production of nonresonance lepton pairs. However, higher order QCD corrections are needed in order to reproduce the correct cross section. Without these higher order corrections the calculated cross section is too low by about a factor of 2. These higher order corrections are also needed to explain the transverse momentum distribution of the Drell-Yan pairs.

The models used to explain the production of charmonium are very similar to the Drell-Yan model. In the Drell-Yan model a light quark and antiquark are used to create the lepton pair. In the charmonium production model the incoming partons which create the J/psi can either be a light quark and antiquark, or a charmed quark and antiquark, or two gluons. The virtual photon is replaced by a J/psi

or an object which eventually turns into a J/psi.

The production of charmonium can be broken down into two parts. The first part concerns which of the three types of parton pairs is used to create the heavy quark pair. (There are also models which predict charmonium production from a gluon and a quark. These models make predictions about J/psi production with high transverse momentum.) In the second part the incoming partons form either an object with color (a nonsinglet) or an object without color (a singlet). Since hadrons have no color, any colored object must have this color removed. Some models produce a colored object and remove the color by the emission of soft gluons. Other (singlet) models produce charmonium directly without involving the emission of soft gluons. In this thesis we will be mainly dealing with the first question about which parton is used to create the $c\bar{c}$ pair.

The cross section for charmonium production can be written as:

$$\frac{d\sigma}{dq^2} = \underbrace{\left[\frac{d\sigma(q^2)}{dq^2}\right]}_{\text{elementary process}} \int_0^1 dx_1 \int_0^1 dx_2 \, \delta\left(q^2/s - x_1 x_2\right) F_i(x_1) \bar{F}_i(x_2)$$

where

1. $\frac{d\sigma(q^2)}{dq^2}$ is calculated in the model under study.
2. F_i is the momentum distribution for either the quark or gluon used to create the $c\bar{c}$ pair.

A useful quantity which will be used later on is the Feynman x (x_F) of a particle. The Feynman x of a particle is the longitudinal momentum of the particle in the center of mass frame divided by its maximum possible longitudinal momentum. The Feynman x dependence of

a particle is determined by the structure functions of the incoming partons which created it.

One of the early models proposed to explain the production of charmonium was the charmed quark fusion model (see Figure 2.3). In this model a charmed quark from the sea of one hadron fuses with a charmed antiquark from the sea of the other hadron to form the $c\bar{c}$ pair. By assuming a coupling constant $g_c^2/4\pi \sim .5$ and a charmed quark-antiquark sea which has been suppressed by a factor 5., Sivers [5] derives a cross section for ψ production by hadrons with the order of magnitude observed experimentally.

Although this model gives the correct cross section, it has some problems. We will enumerate 3 of these problems. (1) This model predicts that charmed particles would be produced along with the J/psi. A variety of groups have searched for the associated production of charmed particles. Using a sample of 66,000 J/psis produced at 225 Gev/c by π^-, Anderson et. al. [6] searched for the associated production of charmed particles by looking at multimuon events. They reported $\sigma_{\psi D\bar{D}} / \sigma_{\psi} < .016$. Binkley et. al. [7] found $\sigma_{\psi D\bar{D}} / \sigma_{\psi} < .03$ for a 300 Gev/c neutron beam. One group at CERN, WA11, [8] tried to reconstruct charmed particles produced together with their 18,000 J/psis by 185 Gev/c π^- beam. Not finding any charmed particles, they set an upper limit of $\sigma_{\psi D\bar{D}} / \sigma_{\psi} < .08$. Donnachie and Landshoff [9] argue that the final state interactions which must be present below charm threshold will suppress the appearance of charmed particles. They estimate $\sigma_{\psi D\bar{D}} / \sigma_{\psi} \sim .03$ at $\sqrt{s} = 28$ Gev.

(2) In order for this model to give the correct x_F dependence, a

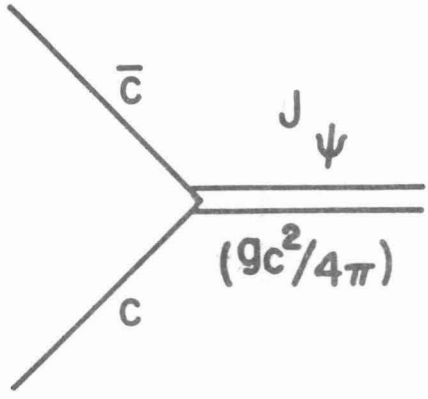

Figure 2.3
Charmonium production by charmed quark fusion

sea quark distribution of the form $(1-x)^5$ is needed [10]. Drell-Yan experiments [11] indicate that the exponent of (1-x) is between 8 and 9.

(3) Deep inelastic lepton scattering gives further evidence against the $c\bar{c}$ fusion model. The ability of the photon gluon fusion model to predict dimuon events in deep inelastic lepton scattering [13,14,15] indicates that the component of intrinsic charm in the hadron is very small.

The next model we will consider is the quark fusion model represented by Figures 2.4(a,b,c). Since hadrons are color singlets, Figure 2.4a shows that at least one gluon must be emitted to form a color singlet. In order to determine what charmonium states these diagrams will form we note that two gluons couple to states with even charge conjugation. Three gluons will couple to states with odd charge conjugation if the Feynman diagram used to form the states is similar to a QED diagram. Therefore, Figures 2.4a and 2.4b allow the production of chis only while Figure 2.4c allows the production of J/psis. Figures 2.4a and 2.4b would have to have another gluon emitted before they could form a J/psi.

Experimental data indicate that the J/psi is not produced directly by Figure 2.4c. The vertex $\psi q\bar{q}$ can be calculated by assuming that all J/psi production came from direct $q\bar{q}$ production by Figure 2.4c. The resulting vertex factor is about 450 times larger than the same vertex factor calculated from J/psi decay to hadrons [16]. Also the observed angular distribution of the $\psi \to \mu^+\mu^-$ decay disagrees with that predicted by Figure 2.4c. If Figure 2.4c were the dominant mechanism, then the decay distribution of the muon

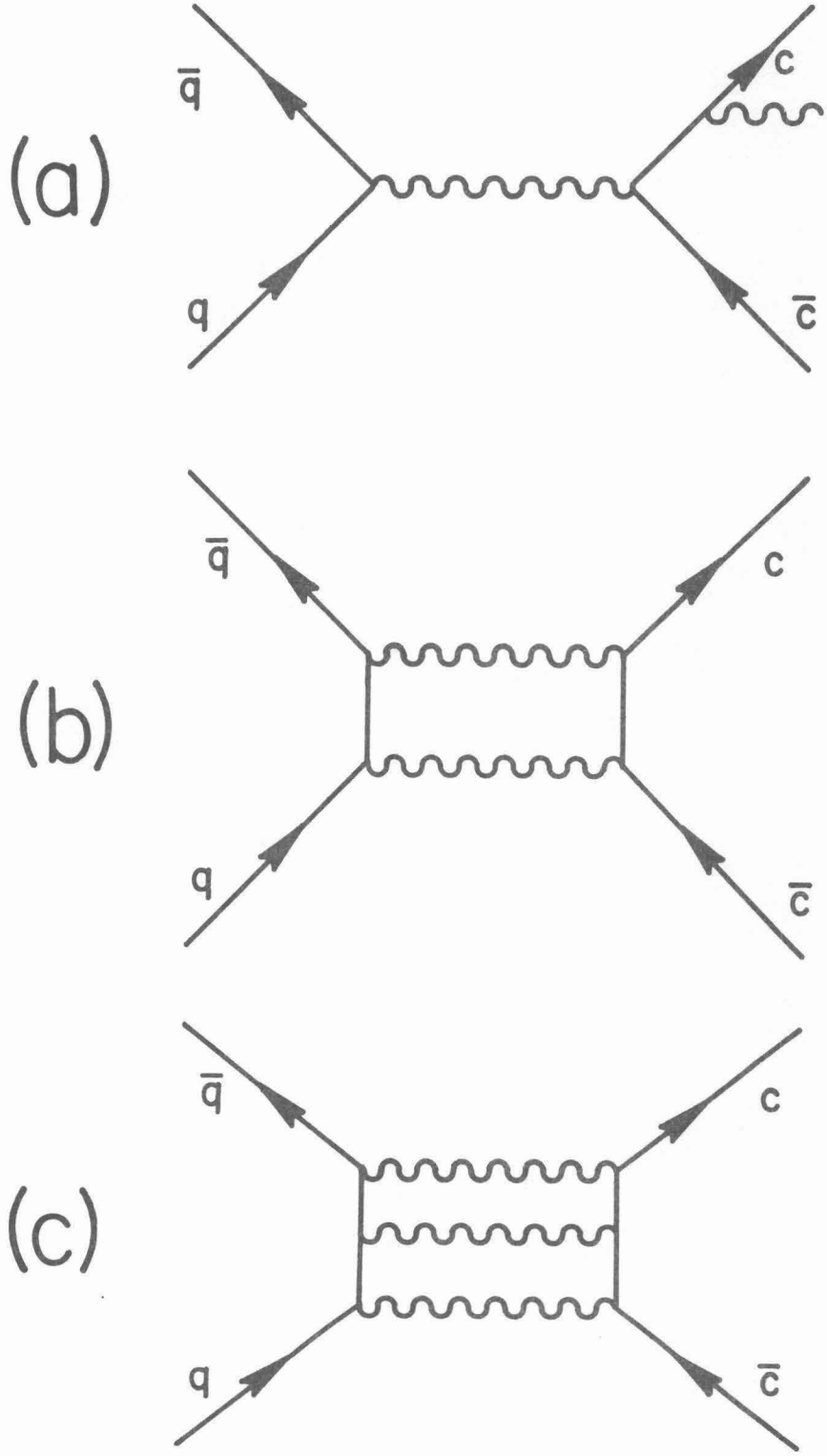

Figure 2.4
Charmonium production by $q\bar{q}$ fusion

relative to the incident $q\bar{q}$ should be $1 + a*\cos 2\theta$ with $a = 1$. Several groups have measured a. In the Collins Soper frame [17], G. E. Hogan et. al. [18] give $a = -.10 \pm .05$ for J/psi production by 200 Gev/c pions. Badier et. al. [19] state $a = .05 \pm .07$ for J/psi production by 200 Gev/c pions. We conclude that although Diagram 2.4c is suppressed, quark fusion is still possible in 4a and 4b which may lead to J/psi production if more gluons are emitted.

The third possible mechanism of J/psi production is gluon fusion. Deep inelastic lepton scattering indicates that 1/2 the momentum of a hadron is carried by gluons; therefore gluon fusion might play an important role in the production of charmonium. Carlson and Suaya [20,21] calculate that about 30% to 50% of the hadronically produced J/psis could come from the direct production of chis by 2 gluons. Figure 2.5(a,b,c) illustrates the production of chi particles. We note that Diagrams 2.5a and 2.5b may produce chis directly by gluon fusion. Gluon fusion can also occur by the fusion of 2 gluons to form a colored object. The colored object must then emit a gluon to form a color singlet. In this case Diagrams 2.5(a,b,c) are needed. The soft gluon which must be emitted is shown in Figure 2.5c. If in Diagrams 2.5a or 2.5b the gluons form a colored object and one gluon is emitted, the final product is a J/psi. Thus, J/psi versus chi production does not unambiguously indicate quark or gluon fusion.

The object of this thesis is to try to determine information about whether charmonium production by π^- at 225 Gev/c goes via quark fusion or gluon fusion or both by looking at the forward charge. In view of the problems listed above, we will no longer

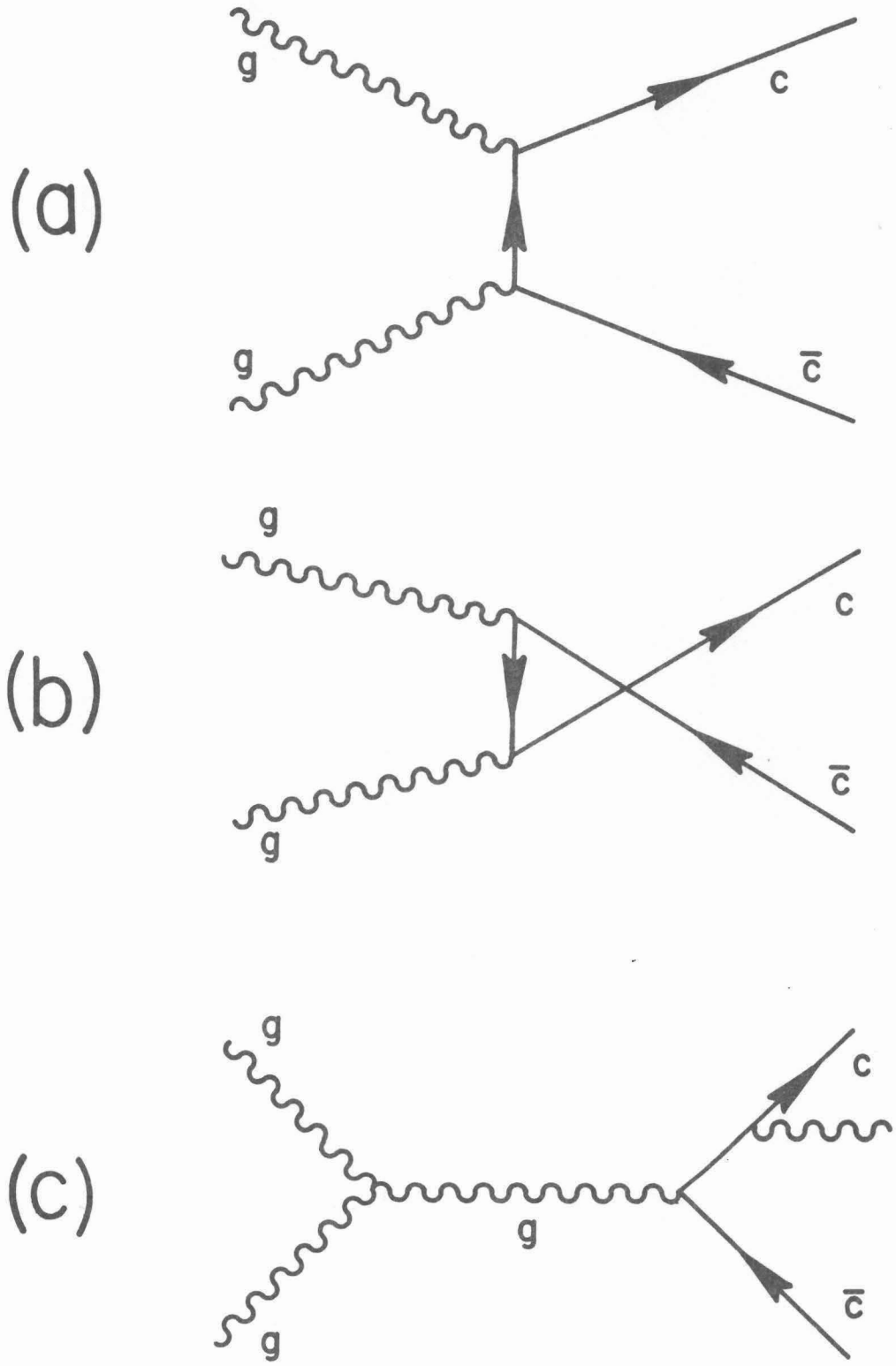

Figure 2.5
Charmonium production by gluon fusion

consider the charmed quark fusion model.

Many authors consider the production of J/psis by a combination of quark and gluon fusion [22,23,24]. Assuming that that both color singlet and color nonsinglet production will contribute, Gluck et. al. [22] calculate the production of J/psis by considering the Diagrams 2.4a and 2.5(a,b,c). Figure 2.6(a,b) is a plot of their calculation for 225 Gev/c π^- on carbon, of relative values of $d\sigma/dx_F$ for quark fusion, gluon fusion and the sum of these normalized to the data. The calculations for 6a and 6b use different sets of quark and gluon distribution functions. The distribution functions used for 6a were calculated by renormalization group techniques [25], while those for 6b were derived from simple counting rules [26,27]. In order to normalize these theoretical predictions to the experimental data, the predictions for Diagram 2.6a have been divided by 2 and those for 6b have been divided by 8. We note that in 6b gluon fusion is dominant at low x_F and quark fusion is dominant at high x_F. The crossover point between gluon fusion and quark fusion is at $x_F = 0.6$. The relative increase of quark fusion with Feynman x is due to the flatter distribution of quark distribution functions than gluon distribution functions. Counting rule arguments suggest valence quark distribution functions for pions go as (1-x), while gluon distribution functions go as $(1-x)^3$. Diagram 2.6b indicates that gluon fusion is an important component of J/psi production.

In determining whether quark fusion or gluon fusion is dominant by looking at the x_F distribution, we have to know the x_F distribution of the quarks and gluons in the hadron. The x_F valence

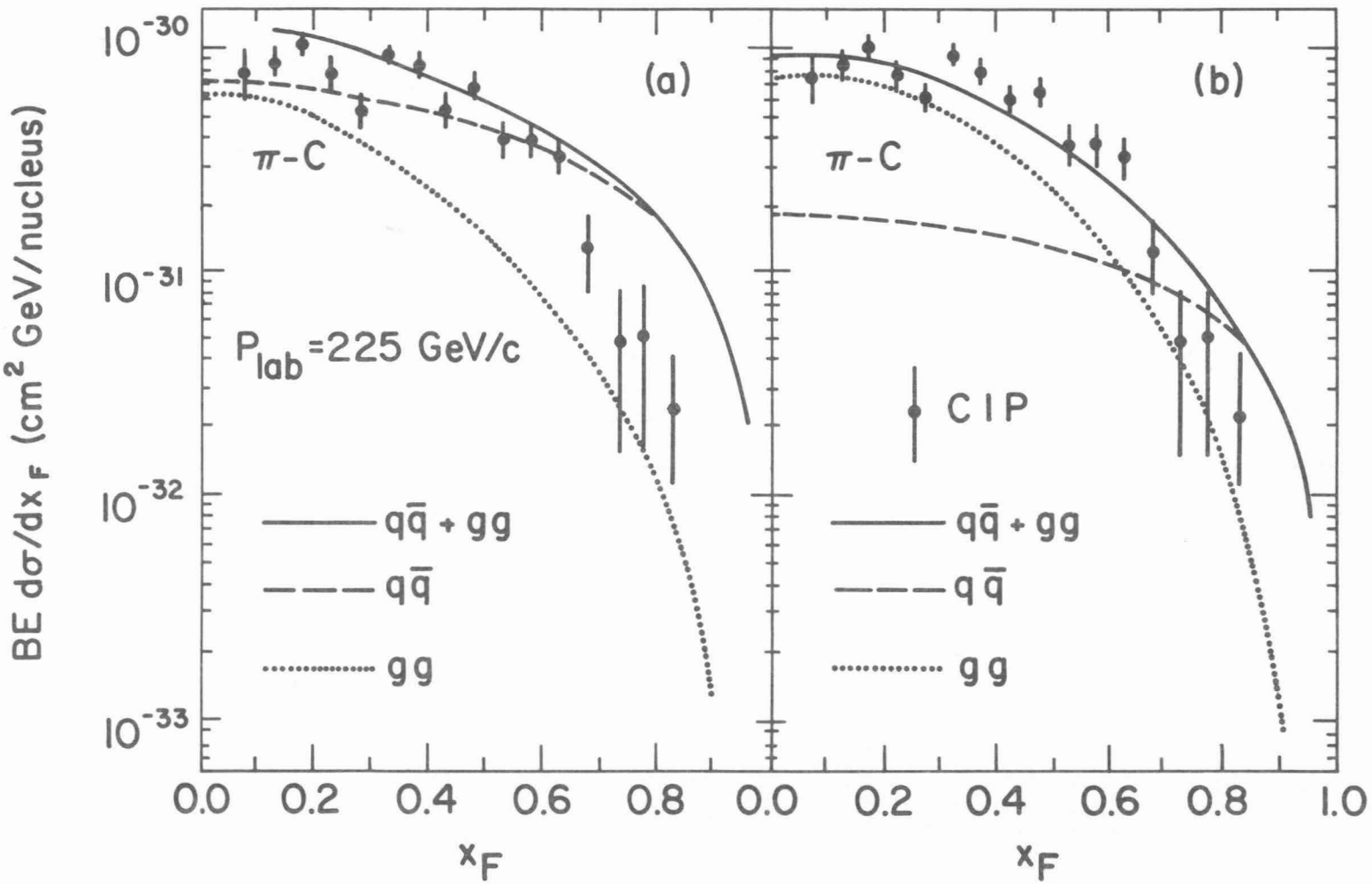

Figure 2.6
Calculation of BEdσ/dx_F vs x_F
(a) uses dynamical QCD structure functions
(b) uses counting rule structure functions
Figure taken from Reference 22

quark and sea quark distributions for nucleons have been determined by deep inelastic lepton scattering. They can also be calculated from the high mass Drell-Yan pairs produced in hadronic interactions. The valence quark and sea quark distribution functions from these two methods agree [28,29].

In order to get the quark distribution function for pions, pion production of high mass Drell-Yan pairs is used. This method gives (1-x) for the valence quark distribution function, which agrees with counting rules. Other methods [30,31] using the inclusive production of mesons also agree with the Drell-Yan result. However, one of these methods [30], states that almost all of the hadron momentum comes from the quarks and antiquarks. This disagrees with the result from deep inelastic lepton scattering mentioned above that 1/2 the hadron's momentum is carried by the gluons. The reliability of the Drell-Yan method for determining the quark distribution functions in pions is based on the agreement between the Drell-Yan method and deep inelastic scattering in nucleons.

Experimental determination of the gluon distribution function is on less firm ground. T. Weiler [32] assumes that production of J/psis by muons and photons proceeds by photon gluon fusion. From this assumption he is able to extract the gluon distribution function of a nucleon. He gets $(1-x)^{5.6}$, which is in agreement with counting rules. The other method of determining the gluon distribution function involves assuming that part or all of the hadronic production of J/psis comes from gluon fusion. The gluon distribution function can be calculated in the same way as quark distribution functions calculated in the Drell-Yan process. This process is the

only way so far of determining the gluon distribution function of the pion. Using hadronic production of J/psi data, Barger et. al. [24] calculate the gluon distribution functions of nucleons and pions. For nucleons they get $(1-x)^5$. For 225 Gev/c pions they claim that the gg and $q\bar{q}$ contribution to J/psi production are comparable. The gluon distribution function they calculate is $(1-x)^3$, in agreement with counting rules. In trying to use the Feynman x distribution to determine the production mechanism for the J/psi by π^-, we have to remember that the gluon distribution for the pion is not independently known.

The ratio of cross sections for J/psi production by various beam particles gives one of the best ways of determining the J/psi production mechanism. Figure 2.7 [22] gives calculated ratios of J/psi production by P, $\bar{P}$, $\pi^{\pm}$, and $K^{\pm}$ beams. Anderson et. al. [33] give the cross sections times branching ratio for ψ production by π^+, π^-, P and $\bar{P}$ beams on carbon at 225 Gev/c. They are:

	$B\sigma(\psi)$(nb/nucleus)
π^-	88 ± 12
π^+	82 ± 12
P	53 ± 7
$\bar{P}$	85 ± 4

These numbers compared with the graphs of Figure 2.7 indicate that the $q\bar{q}$ mechanism alone does not predict the observed result on carbon. The experiment NA3 [19] gives $\sigma(PP\to\psi)/\sigma(P\bar{P}\to\psi)$ to be .50 ± .08 at 150 Gev/c ($\sqrt{s}$ = 16.8 Gev) and .71 ± .16 at 200 Gev/c ($\sqrt{s}$ = 19.4 Gev). Experiment 537 at Fermilab [34] reports $\sigma_{\bar{p}}/\sigma_{\pi}$ = .88 ± .05, $\sigma_p/\sigma_{\bar{p}}$ = .53 ± .07 at P=150 Gev/c.

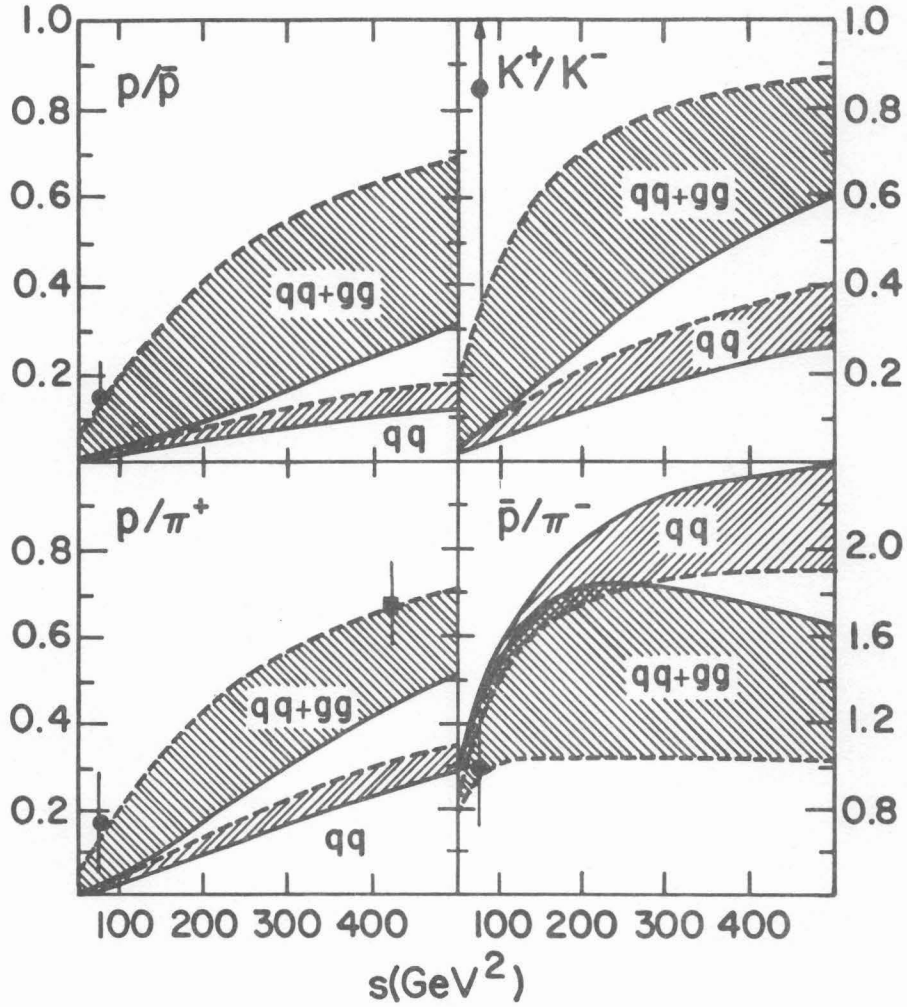

Figure 2.7
Prediction for the beam ratio of J/psi production using incident P, P, $\pi^{\mp}$, and $K^{\mp}$ beams.
Figure taken from Reference 22

The forward going charge for J/psi events produced by quark fusion should be different from the forward going charge for J/psi events produced by gluon fusion. Figure 2.8 illustrates quark fusion by a π^- beam. The pion consists of one $\bar{u}$ quark and one d quark. The $\bar{u}$ quark is removed in the production of the J/psi. This leaves only the d quark to fragment in the forward direction. Hence, we might expect the forward charge to be -1/3. Figure 2.9 illustrates gluon fusion by a π^- beam. In gluon fusion neither valence quark in the pion is removed to form the J/psi. In this case we might expect a charge of -1 in the forward direction. Because of the complex and not understood problem of forming hadrons from these quarks, we do not necessarily expect these numbers to be exactly -1/3 for quark fusion and -1 for gluon fusion. We do, however, expect the forward charge to be more negative for gluon fusion than for quark fusion.

V. Cerny et. al. [35] calculated dQ/dy using a simple quark parton model. Q is the number of positive particles minus the number of negative particles, and y is rapidity. They did this for both $\pi^- P \rightarrow \mu^+\mu^-$ + hadrons (quark fusion) and $\pi^- P \rightarrow$ hadrons at $\sqrt{s}$ = 7.56 Gev. They assumed the Drell-Yan pair to be produced at y = 0 with mass 2.56 Gev/c^2. When they calculated the net charge in the forward hemisphere for each process and compared, they found the difference

$$\langle Q_F \rangle_{\pi^- p \rightarrow \text{hadrons}} - \langle Q_F \rangle_{\pi^- p \rightarrow \mu^+\mu^- + \text{hadrons}} \sim -.7$$

This is approximately the charge of the $\bar{u}$ quark used to create the Drell-Yan pair. This model might be too simple to give the correct answer for the net charge in the forward direction, but it suggests that we should see a difference between quark and qluon

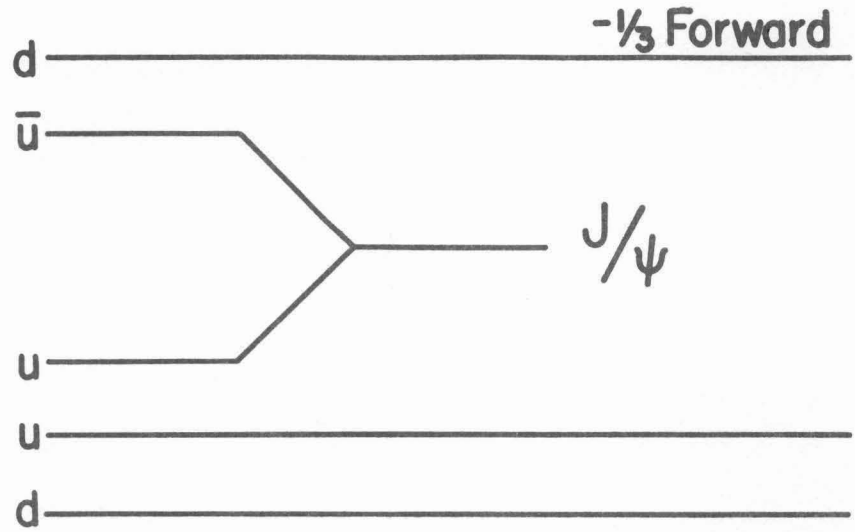

Figure 2.8
Forward charge for quark fusion

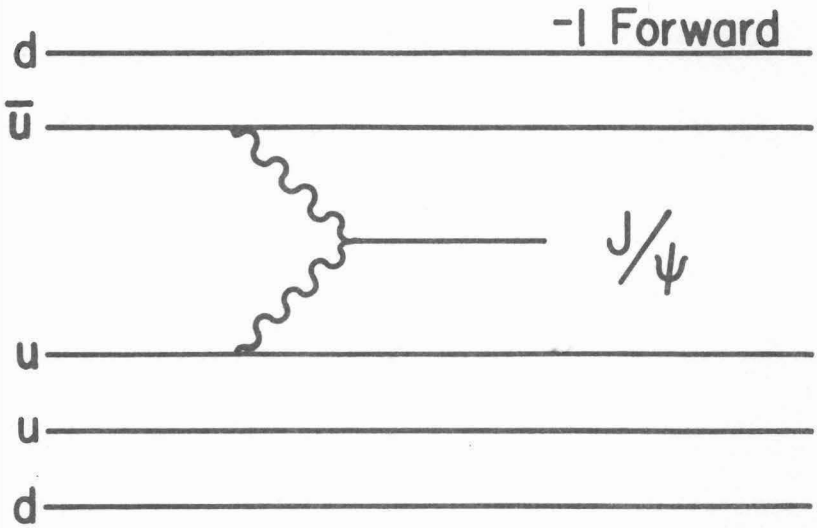

Figure 2.9
Forward charge for gluon fusion

fusion by looking at the forward charge. The next chapter describes the apparatus we used to measure the forward charge in hadronic J/psi production.

CHAPTER 3

APPARATUS

This section concerns the equipment relevant to this investigation, including the beam line, the beam tracking system, the chambers, and the hodoscopes. The equipment will be described from upstream to downstream. The multicell gas Cherenkov counter, described in P. Schoessow's thesis [36], and the lead glass detector, described in S. Hahn's thesis, were not involved in the present analysis.

The definition of the lab coordinate system is as follows. The beam travels in the + Z direction. The + Y direction is up. Looking downstream, the + X direction is left. This defines a right-handed coordinate system with the origin at the center of the Chicago Cyclotron Magnet (CCM).

3.1 Beam

The N1 beam line in the neutrino area at Fermilab provided 225 $\pm$ 2.5 Gev/c π^- mesons. During a previous experiment, E369, 3 beam Cherenkov counters measured the beam composition to be 97% π^-, 2% K^-, and .3% $\bar{P}$. These beam Cherenkov detectors were unavailable for E610, but the composition must be similar to that of E369. The typical intensity for E610 was 2.5 - 3.0 million particles per 1.5 second spill.

3.2 Beam Chambers and Hodoscopes

The incoming beam track was measured by a total of six beam chambers and their associated hodoscopes. Figure 3.2 illustrates the

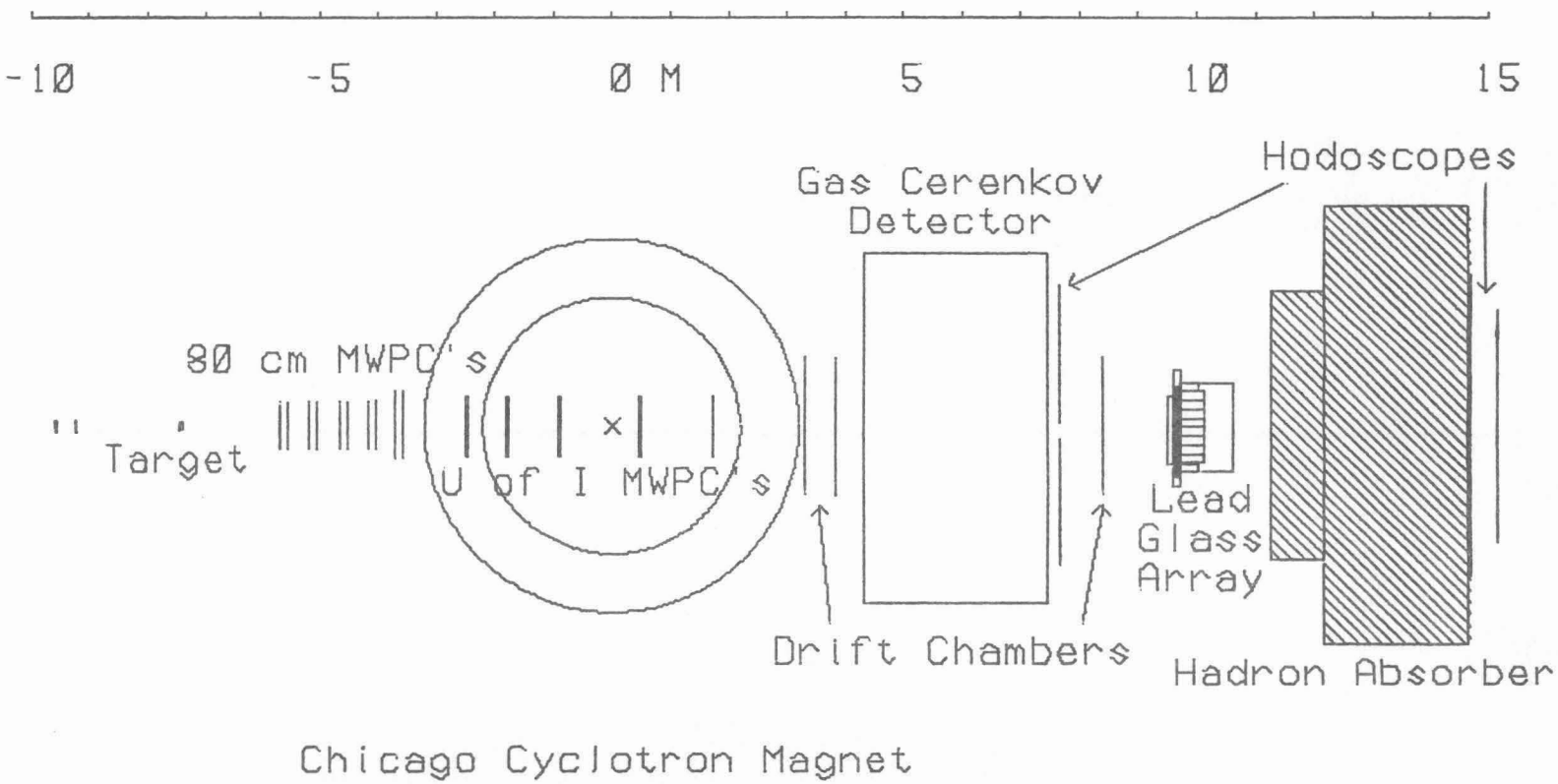

Figure 3.1
E610 Spectrometer

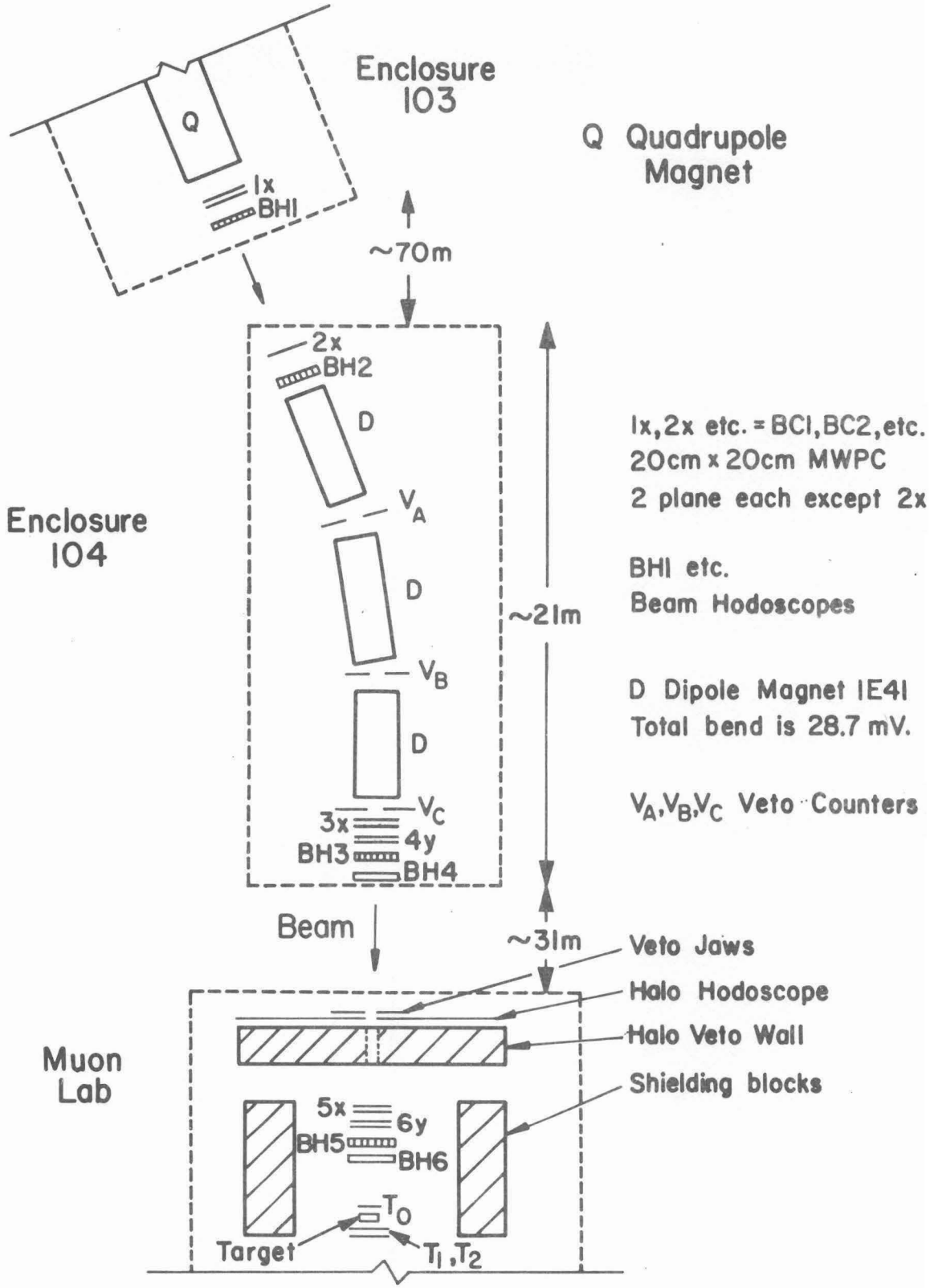

Figure 3.2
Downstream end of N1 beam line and target region
Not drawn to scale

positions of the beam chambers and hodoscopes in the beam line. Four of these chambers measured X coordinates, while two others measured Y coordinates. Two of the X-measuring chambers were upstream of the magnet 1E41. They had a 70 meter distance between them. The other two X-measuring chambers and two Y-measuring chambers were downstream of 1E41. The four X-measuring beam chambers could be used to reconstruct the beam momentum, since the magnet 1E41 bent in X. The chambers had an active area of 20 cm by 20 cm. They had a wire spacing of 1/12 of an inch. All the chambers except beam chamber 2 were actually double planes. The 2 planes were very close to each other and were staggered by half a wire spacing. The geometry of the beam chambers allowed the energy of the beam particle to be measured within .3%.

Immediately downstream of each beam chamber, a beam hodoscope measured the same coordinate and provided fast timing information. Each hodoscope consisted of 8 elements, each 1.8 cm wide in BH2 through BH6, and 2.5 cm wide in BH1.

These hodoscopes were in the trigger. A beam track for an event was required to have a hit in one of the central four elements of each of the X-measuring beam hodoscopes. The beam hodoscope hits were also latched and read into the computer.

The particle momentum was measured by the deflection in the magnet 1E41, the last bending magnet in the N1 beam line. It actually consisted of 3 main-ring-type magnets labeled D in Figure 3.2. Its current was read into our computer so that accurate determination of the beam energy could be made.

3.3 Beam Veto Counters

Immediately downstream of each of the 3 bending magnets (1E41) in Enclosure 104 were a set of veto counters. These counters would veto events with particles outside the magnet aperture.

In the Muon Lab, just upstream of the target the Halo Hodoscope (Figure 3.3) would veto events with a halo particle produced upstream of the Muon Lab. This hodoscope was about 5 meters wide by 3 meters high. It consisted of 20 counters and had a hole in it for the incoming beam. Covering up part of this hole was a set of four counters called the veto jaws. These counters defined a 4 inch square area the beam could go through without being vetoed. The veto jaws consisted of two 10 inch square counters placed above and below the beam hole and two 12 inch square counters placed to the right and to the left of the beam hole. Just downstream of the Halo Hodoscope was a 1 meter thick concrete wall to prevent backscattered particles from the target interaction from returning to the Halo Hodoscope.

3.4 Target and Target Counters

The target was six 1/2 inch thick pieces of beryllium taped together giving a total thickness of 3 inches of beryllium. This was approximately 12.5% of an interaction length. The target was 5 3/16 inches wide and 3 inches high. The target was attached to a set of pullies so that it could be moved in and out of the beam line while the beam was on. A mirror placed near the target enabled us to determine the positon of the target after it had been moved.

Three scintillation counters T0, T1, and T2 surrounded the target. The one upstream of the target, T0, was 2 inches in height

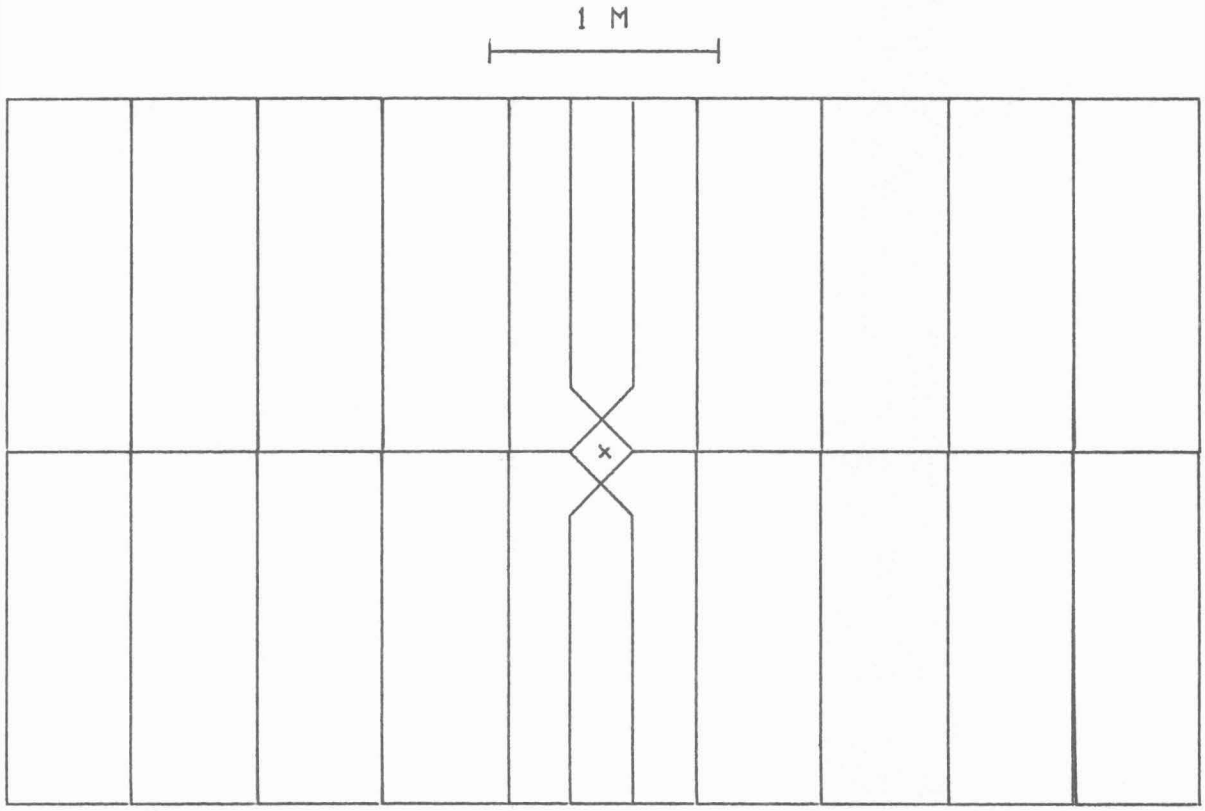

Figure 3.3
Halo Hodoscope

and 3 inches in width. A hit was required in this counter, so it defined the size of our interacting beam. This counter also defined the start time for the experiment. T1 and T2 were both 5 inch square counters. These counters indicated by pulse height whether an interaction had taken place in the target or not.

3.5 80 cm Chambers

Between 2 and 3 meters downstream of the target, and upstream of the CCM, were located the five 80 cm chambers. Each 80 cm chamber consisted of two measuring planes of wires perpendicular to each other. The first four chambers provided a total of four X and four Y measuring planes. The most downstream 80 cm chamber was tilted at a 45 degree angle to give two tilted planes. One of these tilted planes did not hold high voltage very well and had an efficiency of about 72%. This chamber sat on the edge of the CCM.

The 80 cm chambers after being used for two previous experiments were rebuilt for E610. Each plane had about 500 wires with a wire spacing of 1/16 of an inch. They had an active area of about 80 cm by 80 cm. These chambers operated well thoughout the experiment and had an average efficiency of 97%. For a more detailed description see the thesis of R. Hicks.

3.6 Chicago Cyclotron Magnet

The Chicago Cyclotron Magnet is the Muon Lab's most distinctive feature. The magnet was from the old 450 Mev Chicago Synchro - cyclotron. The magnet has a gap of 1.29 m and pole tip diameter of 4.32 m. We operated it at 4200 A which gave a magnet field of 14.3

kilogauss at the center of the magnet. The field is fairly constant from the center of the CCM to r = 1.5 m. The field falls off to 90%, 50% and 10% of its central value at distances of 1.7 m, 2.4 m, and 3.3 m, respectively, from the center of the magnet. The magnet gives a 2.15 Gev/c kick to a track passing through it. The CCM was rotationally symmetric to better than 1%.

3.7 University of Illinois Chambers

In the CCM were 5 multiwire proportional chambers built at the University of Illinois for E610. Each chamber contained 3 anode planes. Two of the planes were tilted 11° from the vertical in opposite directions. The wires in the other plane were horizontal and measured Y. Each tilted plane had 528 wires with a wire spacing of 1.96 mm. The wires were 98 cm long giving the plane an active area of .96 m by 1.06 m. The Y plane had 480 wires with a wire spacing of 2 mm. The wires are 1.26 meters long giving an active area of .96 m by 1.26 m. The separation between the anode planes was 1/2 inch.

The U of I chambers had some problems during their operation. Their efficiency was about 93%. The inefficiency was due in part to the high intensity of the beam. The chambers were noisy. About 30% of the time one of the planes would have a string of hits not associated with a track. These were called lightups. They ranged in size between a very small portion of a plane to about 1/3 the width of the plane. These lightups usually did not consist of a string of consecutive hits, but rather an area of high concentration of hits. If one of the planes in a chamber lit up, it was likely that another

plane in that chamber would lightup. A lightup in one chamber did not cause a lightup in another chamber. All in all, any one chamber had a lightup about 7% of the time. The origin of these lightups was never found. These lightups caused problems in the trackfinding. For a more complete discussion of the chambers and how they were built see Appendix F.

3.8 Drift Chambers

E610 had three drift chambers downstream of the CCM to complete the particle trajectories. Four drift chambers were built, but one of them, the most downstream one, never held high voltage for long periods of time. The drift cell size was 4 cm wide by 1.5 m high. A cell actually had 2 anode wires in it separated by .53 cm with a divider between them. This enabled easier resolution of the left right ambiguity. Each drift chamber contained 60 cells for a total active area of 1.5 m in Y by 2.4 m in X. The sense wires in the 2 central cells had 8 cm of deadener on them. The drift chambers were the only chambers in E610 with deadeners in the central region. The average efficiency of the drift chambers was 78%, excluding DC4.

The novel feature of these drift chambers is that they read out in both X and Y. For a discussion of how this was done see the thesis of P. Schoessow [36] and articles of M. Atac [37,38]. Unfortunately, the Y readout was transformer coupled through magnetic cores. The cores on the two most upstream chambers tended to be saturated by the fringe field of the CCM. Therefore, the Y readout did not work at all for the first drift chamber and was only 21% efficient for the second drift chamber. For the third chamber the Y

readout was only 64% efficient.

The Y readout was also necessary to determine which of the two wires in a cell had the hit. As stated in the previous paragraph this could be done 0%, 21%, and 64% of the time in Drift Chamber 1, 2 and 3, respectively. Because the two wires in each cell were ORed together, the inefficiency caused a 2-fold left-right ambiguity. Sometimes, the situation was worse. If the hit was closer than half the distance between the two anode wires of a cell, the ambiguity became 4-fold. The Y information was used to resolve ambiguities whenever possible but not for track coordinates.

3.9 Hadron Hodoscope

Between Drift Chambers 2 and 3 was the H Hodoscope (Figure 3.4), which consisted of 56 counters. Each counter was about 20 cm wide by 100 cm high, arranged to overlap so that there was no dead region. The active area of H was 2 m high by 4.5 m wide with a vertical gap 30 cm wide and a 3 cm high gap all the way across to allow the beam to pass through without producing secondaries that would damage the lead glass array behind it. The efficiency of H was near 99.94% for the area covered. H was used to help identify tracks by time correlation.

3.10 Rochester Steel

Downstream of all our chambers and our lead glass array (19 meters downstream of the target) was the Rochester Steel. This steel was approximately 3 m thick, 3 m high, and 6 m wide.

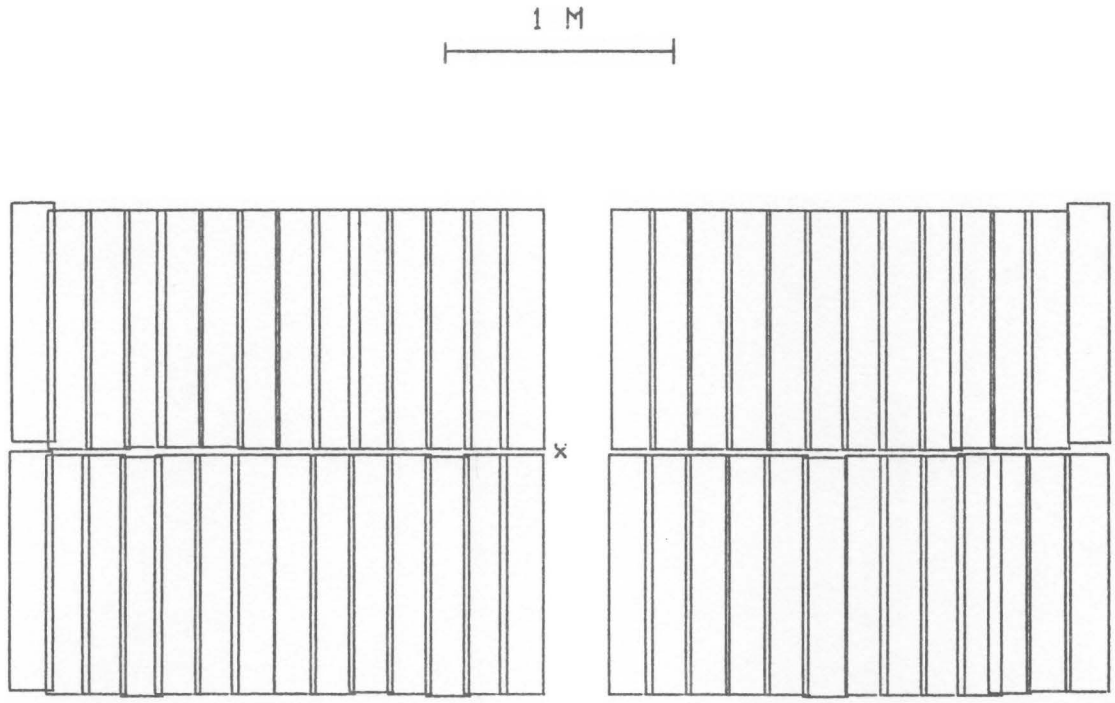

Figure 3.4
H Hodoscope.

3.11 Muon Hodoscope

Immediately downstream of the Rochester Steel was the M Hodoscope (Figure 3.5) consisting of 48 counters covering an area 2.4 m high by 5 m wide. A horizonal gap in the shape of a bow tie centered on the beam took advantage of the x-y correlation produced by the magnetic field to exclude low mass dimuon pairs from the trigger. High mass pairs would always be separated vertically enough to trigger. If they had large forward momentum, they would reach the center elements. If they had small forward momentum, the magnet deflected them away from the center where the gap was wider. In this way, the Feynman X acceptance for high mass dimuon pairs was favorable in the interval $0.1 < x_F < 1.0$ (see Figure 5.2).

The M′ hodoscope consisted of 8 counters 0.5 meter behind M. This was the only hodoscope, except for 2 beam hodoscopes, with horizontal elements. M′ covered an area of 0.7 m by 4 m. Because of the small size of the overlap between M and M′, M′ was not used in the analysis.

3.12 Dimuon Trigger

This section will give an elementary discussion of the dimuon trigger. For a more complete discussion of the trigger, including the logic diagrams, see the thesis of S. Hahn.

The dimuon trigger required a clean beam. A clean beam event included a hit in one of the central 4 elements of each of the X-measuring beam hodoscopes. It also required that none of the various beam veto counters had a hit. The target counter T0 had to have a hit. The counters T1 and T2 just downstream of the target

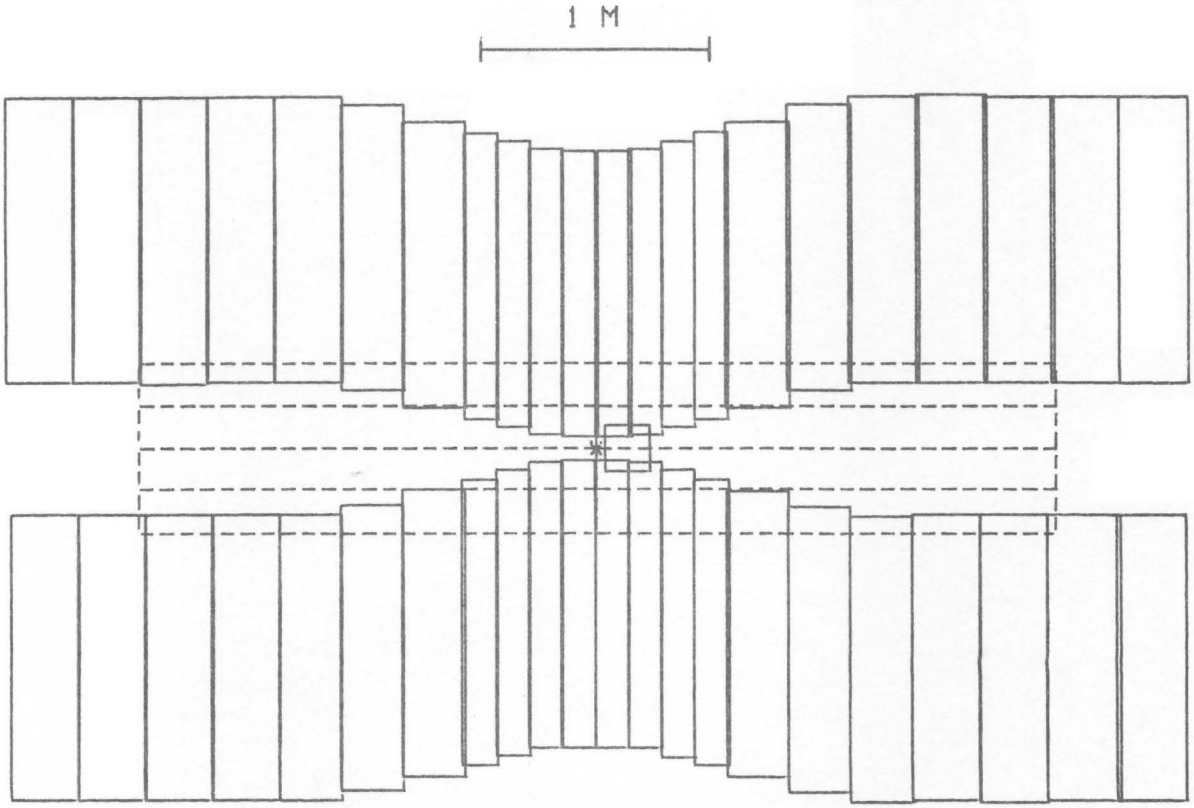

Figure 3.5
The solid lines represent M Hodoscope.
The dotted lines represent M′ Hodoscope.
The square box in the center represents the beam veto.

were both required to have a pulse height equivalent to three particles.

The dimuon trigger satisfied the clean beam requirement and had two hits in opposite quadrants of the M hodoscope. The trigger required either a hit in the upper left hand quadrant and lower right quadrant or a hit in the upper right hand quadrant and lower left hand quadrant. In order to prevent a punch-through beam particle from causing a trigger, an 8 inch square counter (bigger than the bow tie gap) was put behind M to act as a beam veto (Figure 3.5). If this counter had a hit, then the event was vetoed. The dimuon trigger also required a hit in the H Hodoscope.

CHAPTER 4

ANALYSIS

The analysis of data consisted mainly of finding tracks of particles associated with J/psi production. Two kinds of trackfinding were involved. The first trackfinder simply looked for two opposite sign muons. These muons which triggered the events had momenta greater than 6 Gev/c; hence this trackfinder did not need to determine momenta precisely or to find low momentum tracks.

The first trackfinder reconstructed the tracks for the 3.5 million triggers to determine if they had 2 or more muons. The trackfinder was only called on those events with hits in the M counter which satisfied the opposite quadrant requirement. If the event had 1 or more opposite sign dimuon pairs, the event along with the tracking information was written out to another tape. This pass though the data was called the second pass.

The second trackfinder reanalyzed the dimuon events with the capability of measuring momenta precisely and of finding tracks with momenta down to 1 Gev/c. There are only two major differences between these two trackfinders. The second trackfinder has a better predicting scheme for low momentum tracks and a better algorithm for removing bogus tracks. Details of this trackfinder are given in Appendix A. The various steps in the analysis are outlined in the following sections 4.1 - 4.8.

4.1 Alignment

The locations of all the chambers were needed for the data analysis. The six beam chambers were surveyed relative to the N1

beam line. The center of the CCM was the origin of coordinates, with X directed horizontally to the beam left, Y up and Z in the beam direction. This coordinate system was actually defined by the four beam chambers BC3 - BC6 downsteam of the 1E41 bending magnet because they were surveyed and because their 30 meter separation provided a long lever arm (Figure 3.2). Subsequent measurements indicated that the origin of this coordinate system was within 1.5 cm of the CCM center. The surveyed location of BC1 was used together with those of BC3 and BC5 to correct that of BC2 by linking upstream and downstream tracks in the center of 1E41.

The X and Y coordinates of the 80 cm chambers, UI chambers, and drift chambers were determined by beam tracks found in the last four beam chambers. The azimuthal orientations of the chamber planes were determined by a T. Graff program using straight line tracks (not beam tracks) found in the 80 cm and UI chambers. The algorithm involves minimizing a quantity χ^2 defined by

$$\chi^2(\theta,\delta) = \sum_{i=1}^{\#\text{ of events}} \left[u_i - (x_i \cos\theta + y_i \sin\theta + \delta) \right]^2 / wt$$

with respect to δ and θ.

1. The sum is over many straight line tracks.

2. u_i is the coordinate measured perpendicular to the wires. x_i and y_i are the X and Y of the straight line track at that plane.

3. θ is the angle between the wires and the X axis.

4. δ is the offset distance of the plane in the u direction.

5. wt is proportional to the wire spacing.

The chambers were aligned by this procedure using electrons from our electron calibration, halo muons, and interaction events with CCM off. There was good agreement in the alignment using data taken at different times. The alignment of the 80 cm chambers, UI chambers, drift chambers and p-tubes was fine tuned this way.

The alignment had several problems associated with it. Since the alignment was started in the beam chambers, the final alignment may not have the XY origin of our coodinate system at the center of the CCM. The origin of our coordinate system should coincide with the center of the CCM because data from the CCM field are used to calculate momenta. Alignment done in E673, the next experiment after E610, indicates our Y origin is within 1 cm from the center of the CCM. The method of positioning of the UI chambers in the magnet indicates our X origin agrees with the CCM origin within 2 cm. A second problem deals with the matching of tracks up and downstream of the CCM when the CCM is on. The average difference between the up and downstream impact parameters is .7 mm for both + and - tracks. The upstream impact parameter is calculated using the interaction vertex and the 80 cm chambers. The downstream impact parameters are calculated using the drift chambers. A third problem deals with the difference in bending between + and - particles in the CCM. We can use an upstream track and a point in UI5 to make a prediction for the

hits in the other UI chambers. If we look at the difference between the predicted hit and the nearest actual hit, we find + particles bend slightly differently from - particles. The difference is about 0.9 mm in UI4 for tracks between 15 Gev/c and 25 Gev/c. It is as if the CCM is not symmetric in X along the beam line. We searched for explanations of problems 2 and 3, but never found them.

4.2 Beam Reconstruction

The purpose of the beam reconstruction is to determine the beam energy and starting point for the vertex finder. To compute the beam energy BC1, BC2, BC3, BC5, and their associated hodoscopes are used. To compute the X beam track for the vertex, BC3 and BC5 are used. To compute the Y beam track for the vertex, BC4 and BC6 are used. To get the points for the calculation of the beam parameters, the beam hodoscopes are scanned for hits. If the associated beam chambers have hits behind the hit hodoscope elements, then these hits are used. If the hit hodoscope element has no chamber hit behind it, then the center of the hodoscope element is used. If no hodoscope element fired, then all the beam chamber hits are used. The beam chambers had as many stale hits in them as real hits. This is the reason behind using beam chamber hits which are screened by a hodoscope element.

In order to try to remove bogus hits associated with the X measuring chambers, the beam tracks upstream and downstream of 1E41 are projected into 1E41. If at least one upstream and downstream track match up, then only those hits associated with matched upstream and downstream tracks are kept. If no track matches up, all points

are kept. The remaining points in each plane are averaged if the distance between them differs by less than a hodoscope element. If the points in the chamber differ by greater than a hodoscope element then that plane is rejected. Using the remaining hits, one beam track is computed. The algorithm is able to compute a starting value for the vertex finder about 98% of the time.

4.3 Vertex Finding

The upstream trackfinding was designed to find all tracks that came from the primary vertex. These routines were written by people at Fermilab, mainly S. Pordes and R. Raja. The vertex finding and upstream trackfinding are done separately in X and Y. The upstream trackfinder requires a good vertex to find all tracks. Hence, the interaction vertex is found before the upstream trackfinding is done.

The vertex finding starts with trackfinding in the 80 cm chambers. First the four X planes and four Y planes are scanned for 4-point straight line tracks which project to within 5 cm of the beam vertex. The tracks are found by using two planes to define a road. A search into the 2 other planes is made. If hits are found and the track passes a chi-squared cut, the track is stored. Once a track is found, its hits are removed from the track buffer. These tracks are used to find the interaction vertex.

The vertex finder uses these tracks to find the largest cluster of the tracks at the center of the target. The cluster of tracks also includes the beam track if it is found. The largest cluster is the greatest number of tracks which are all within 0.6 cm of each other at the Z center of the target. The vertex is the average of

this set of tracks at the Z coordinate of the target center. This vertex is good enough for the upstream trackfinder to find tracks.

4.4 Upstream Trackfinding (Straight Line)

The 80 cm X and Y planes are in the field-free region. Even very low momentum tracks do not bend at all in these planes. Very low momentum tracks will bend slightly in X before they reach the tilted 80 cm planes. For muon finding, this bending can be ignored. However, a 5 Gev/c track will bend 1 cm in X before it reaches UI1. Tracks with momentum greater than 6 Gev/c do not bend very much in Y as they pass though the CCM. Hence, we can treat the Y tracks in the 80 cm planes and the UI planes as straight line tracks.

The upstream trackfinder finds tracks coming from the vertex found above based on the following angle method. The X view uses the four X 80 cm planes while the Y view uses the four Y 80 cm planes and the five UI Y planes. The trackfinder starts by converting all hits to angles relative to the Z axis measured at the vertex and listing them in order of increasing angle for each plane. The minimum angles of all the planes are compared to find the smallest of all. Next, the minimum angle hit in each plane is tested to see if it is in the road defined by the smallest angle hit. If enough hits are in the road, the track is sent off to the fitter to see if it is real. The track needs at least 2 hits in X. In Y it needs to have hits in 60% of the chambers it goes through. If the track has only 2 hits in X, it must point to within .5 cm from the primary vertex. If the track is saved, the hits are removed from the track buffer. If the track is not saved, the smallest angle hit is removed from the track

buffer. The process starts again with a new search for a hit with the next smallest angle. This process is a fast way of finding all vertex associated tracks.

Because the vertex is very important to the trackfinding, the tracks which are vertex associated are used to compute a new vertex. This is done by simply averaging the X Y coordinates of the tracks at the Z center of the target. If the vertex is changed by more than 0.4 cm, the upstream trackfinding is redone with the new vertex. The method is relatively quick and finds almost all vertex associated tracks.

4.5 Downstream Trackfinding (Curved Tracks)

The purpose of downstream trackfinding is to determine which upstream X tracks are matched with which Y tracks and to determine the momentum of the track. The downstream trackfinding was done in the UI chambers in the CCM. No trackfinding was done in the drift chamber, because the drift chamber efficiency was about 78%. In contrast, the efficiency of the UI chambers was about 93%. The drift chambers were used to help determine if tracks were real and to get a better determination of the momentum. I wrote the downstream trackfinding. Some of the ideas for the trackfinder were taken from downstream trackfinders written by R. Raja and P. Schoessow.

The standard track method was used to make predictions in all the UI chambers using a hit in the magnet and an upstream track. The method assumes that the ratio of the deflection of a track at one chamber to that at another chamber is a constant. This statement is shown in Appendix E. Let $X_S(I)$ be the X coordinate in UI chamber I

for a track which will be used as our standard track. $X_S(I)$ can be taken either from our data or derived using a routine which swims tracks through a CCM magnet map by solving Maxwell's equations. Let $S_0(I)$ be the X coordinate for the straight line projection of this upstream track in chamber I. The constants $S_X(I)$, where $S_X(I) = X_S(I) - S_0(I)$, (I = 1, 5), are stored in the trackfinder. These constants are just the deflection from a straight line of a track which we are using as our standard track. The standard track technique makes an X track prediction in one chamber using the upstream X track and X hit in another chamber by the following method. Let $X_0(I)$ be the X coordinate of an upstream track projected into chamber I. From a hit X(I) in chamber I, we can predict a hit X(J) in chamber J by Formula 4.1.

$$X(J) = X_0(J) + (X(I)-X_0(I))\ S_X(J)/S_X(I) \qquad (4.1)$$

For tracks with momentum greater than 6 Gev/c, Formula 4.1 was shown to predict the position of a hit within 2 mm. Almost all muons which get through the CCM have momentum greater than 6 Gev/c. The method used for particles with momentum less than 6 Gev/c will be discussed in Appendix A.

The idea for the downstream trackfinder is to search for the hits for the entire track using the upstream track and one point in the magnet, called the seed point. The trackfinder first pairs an upstream X track with an upstream Y track. Each upstream X and Y track is projected into the two tilted 80 cm planes. Because the fringe field of the CCM is very small at these chambers, a straight line projection using the upstream tracks is adaquate. (Only for tracks with a momentum below 2-3 Gev/c does the bending of the track

before these chambers become important.) Next, hits are searched for in both planes near the predicted value. If a hit is within 0.3 cm of the predicted value, the hit is saved. The attempt to find a downstream track associated with this upstream X Y pair continues regardless of whether hits are found in these tilted planes.

The tilted plane in UI5 with the smaller number of hits is tested to see if any of its hits forms a seed point for a downsteam track. Figure 4.1 is an example to illustrate the trackfinding. The hit wires for the U and V planes are shown. In this case the U plane has 3 hits and the V plane has 4 hits. Hence, the hits U_1, U_2 and U_3 are tested to see if they are seed points for a downstream track.

The use of a seed point to find a downstream track works as follows. Using the upstream X and Y track and the standard track technique, a prediction is made from the U point to the V plane. This is done by first using the U hit and the upstream Y track projected into the U plane to compute an X coordinate at the U plane. A predicted X coordinate is made in the V plane, which is one inch away from the U plane, using the standard track technique, the upstream X track and the computed X hit in the U plane. Next, using the upstream Y track projected in the V plane, the X prediction at the V plane is converted into a V prediction. If there is a hit within 0.4 cm of the prediction, then the U and V hits are called a matched pair and are used to make prediction in the other planes. In Figure 4.1 using the dotted line as the upstream Y track projection, the hit U_1 and the hit V_1 will form a matched pair. The hits U_3 and V_4 also form a matched pair. The hit U_2 has no matched hit. If no V hit is found, then the U point is abandoned and the trackfinder goes

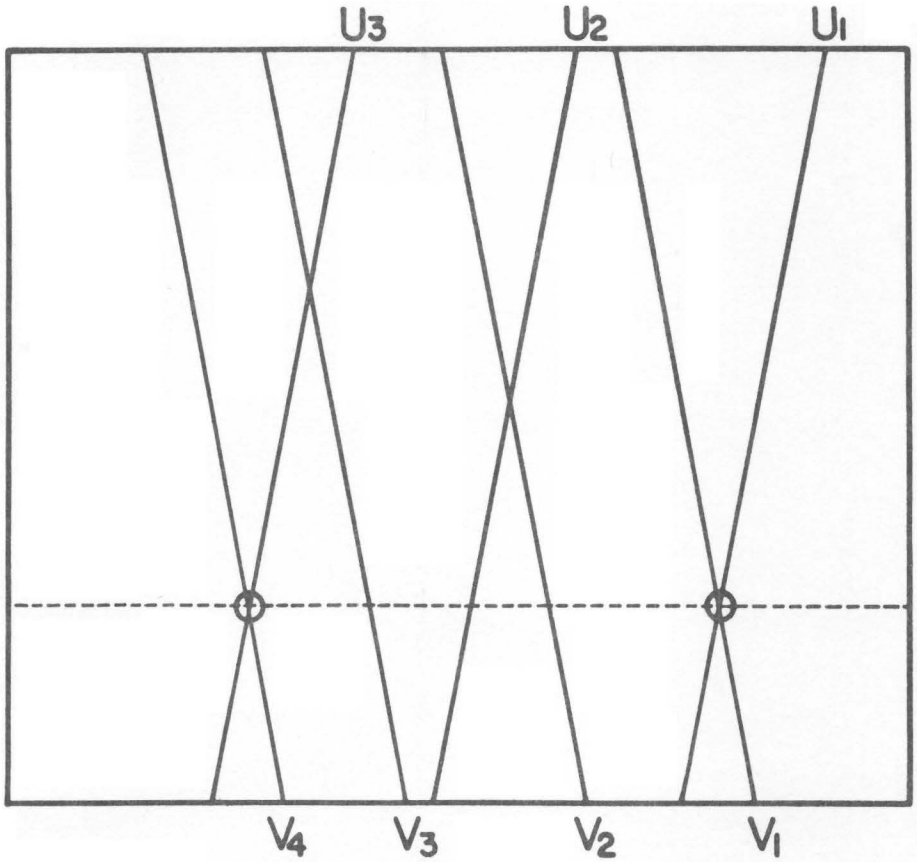

Each tilted line represents a U or V hit for a UI chamber (Y hits are not shown)

The dotted line is the upstream Y track projected into this chamber

Beam is into the paper

O indicates a matched UV hit

Figure 4.1
U and V hits in a UI chamber

on the the next U hit. If a matched V hit is found, then an X hit is computed at UI5 using both the U and the V hit. We note that the Y information is needed to match the hits, but it is not needed to compute the X from the U and V hit. Next, using this X hit and the upstream tracks, a prediction is made in all the UV UI planes using the standard track technique. As stated before, the upstream Y track projected into the U or V plane along with the X prediction at that plane are needed to make a U or V prediction. Next, the planes are searched for hits near their predicted value. If the hits are within the windows, they are saved. All windows upstream of the matched hit are 0.6 cm. The windows downstream of the seed point (if the seed chamber is upstream of UI5) are a function of how far the prediction is being made. They range from .9 cm to 2.0 cm. See Appendix A for a table of the windows. If a track has hits in both U and V planes of a chamber, those hits are required to be a matched pair, otherwise the worse hit is rejected. A track is saved if its total number of hits divided by the number of planes traversed exceeds 0.6.

The maximum number of tilted planes a track could traverse was ten UI tilted planes and two 80 cm planes. However, because one of the tilted 80 cm planes did not hold high voltage very well, its efficiency was only 72%. Because of this problem, the two 80 cm tilted planes are merged as one plane. A hit in both planes counts as one hit. A hit in one plane and miss in the other plane counts as one hit. If the track went through the tilted 80 cm planes and neither plane has a hit, this is counted as one miss. Therefore, the maximum number of hits and tilted planes a track could go through is 11, not 12.

This track is compared with previously found tracks to see if it is real. If two tracks share an upstream X track and a hit in the tilted planes of UI chamber 3, 4 or 5, the trackfinder discards one of the tracks. The better track is picked by checking, in order, the number of planes hit, the efficiency, and the chisquared. The better track is kept and the worse is removed. For full trackfinding, the weeding algorithm is more complicated. The noise in the chambers and the inefficiencies in the chambers contribute to bogus tracks being found. The weeding will be discussed in Appendix A.

After all the U hits in UI5 (or V hits if that plane had the fewer number of hits) are tested, the trackfinder then tests all the hits in either the U or V plane of UI4 to determine if they will form a track using the same procedure. If no downstream track is found using UI4 or UI5 with this particular upstream X and Y track, then the trackfinder searches UI3 for seed points. After searching for seed points for this upstream X and Y track pair, the trackfinder pairs another upstream X and Y track together and starts the process over again by searching for seed points in UI5. The process stops when all upstream X tracks have been paired with all upstream Y tracks.

To speed up trackfinding the following was done. Before a seed point is checked to see if it has a matched hit in the other tilted plane, a rough calculation of the momentum is made using the hit and upstream track. If the momentum is less than 6 Gev/c, the trackfinder goes on to the next point.

Trackfinding was fairly fast. The time for trackfinding, calculating track parameters and determining whether the event has

two muons took only 110 ms per event. This was certainly fast enough to process our 3.5 million triggers.

4.6 Determining Track Parameters

The slope and intercept of the track downstream of the CCM are determined using a simple hard edge fit. It assumes the track in the CCM is parallel to the upstream track at the hard edge. The method calculates downstream slopes and intercepts which are systematically wrong if the standard values of the hard edge radius and magnetic field are used. In order to correct the problem, the hard edge radius is multiplied by a constant while the magnetic field is divided by the same constant, thus keeping magnetic field path integral constant. The constant is a function of the most downstream chamber with a hit for the track. If a track has a hit in UI5, then the constant is 1.095, while if the most downstream hit is UI4 the constant is 1.08. The constants were derived to make the best possible prediction in DC1 and DC2.

The drift chambers were used to get a better determination of momentum and downstream track parameters. They also helped to test for real tracks. The analysis of the drift chambers was done mostly by D. Bauer and P. Schoessow. The determination of drift velocity and resolution of the drift chambers is discussed in the thesis of P. Schoessow [36]. As stated before, the alignment was accomplished with straight-through tracks. We shall now explain how the drift chambers were used in the trackfinding.

The tracks are projected into the drift chambers to look for hits in a 2 step process. First a road is defined in the drift

chambers by continuing the downstream track. The hit in the road of the most upstream chamber is used to correct the downstream track. The corrected track is used to search for hits in the remaining drift chambers. Finally, downstream track parameters are determined by fitting the drift chamber points with the upstream impact parameter.

In order to compute the momentum of the track, a global fit is performed which uses information in all the chambers plus the vertex. This fit also gives a better determination of the upstream slope and intercept. A short description of the procedure will be given. For a more detailed description of the fit see the thesis of P. Schoessow.

The procedure involves minimizing a sum of the squares of the predicted coordinates minus the observed hits. This quantity is given by:

$$\chi^2 = \sum_{i}^{\text{chambers}} \left(X_{PR}^{i}(a,b,c,d,q) - X_{M}^{i} \right)^2 / \sigma_i^2$$

where

1. The sum is over the hit chambers.

2. a, b, c, and d are the upstream X slope, upstream Y slope, upstream X intercept and upstream Y intercept respectively.

3. q is 1/p where p is the momentum of the track.

4. $X_{PR}^{i}(a,b,c,d,q)$ is the predicted coordinate at chamber i. X_{PR}^{i} can either be an X or Y coordinate.

5. X_M^i is the hit at chamber i.

6. σ_i is proportional to the wire spacing.

This problem can be solved by linearizing $X_{PR}^i(a,b,c,d,q)$ about some point (a_0,b_0,c_0,d_0,q_0), at which point χ^2 becomes.

$$\chi^2 = \sum_i \Big[X_{PR}^i(a_0,b_0,c_0,d_0,q_0) + \frac{\partial X_{PR}^i}{\partial a}\delta a + \frac{\partial X_{PR}^i}{\partial b}\delta b + \frac{\partial X_{PR}^i}{\partial c}\delta c + \frac{\partial X_{PR}^i}{\partial d}\delta d + \frac{\partial X_{PR}^i}{\partial q}\delta q - X_M^i \Big]^2$$

This problem reduces to finding δa to δq. For our final J/psi sample $X_{PR}^i(a_0,b_0,c_0,d_0,q_0)$ was evaluated by swimming the track through the magnet using a magnet map. The derivatives upstream of the magnet can be taken analytically. The derivatives in the magnet and downstream of the magnet were done numerically. The derivatives downstream of the magnet were based on the hard edge. The derivatives in the magnet were based on quadratic approximations to the hard edge developed by T. Kirk. The fitting procedure reduced the FWHM of the J/psi from about 105 Mev to about 66 Mev.

This magnet map used above was based on a measurement made of the CCM field for E98, the first experiment to use the CCM as a spectrometer. If we use constants based on this magnet map, the computed mass of the J/psi appears too be about .8% too low. This problem was solved by increasing the magnet field by .8%. Our measured masses of the ω, ϕ, and K_S are given below. For comparison with the standard masses, we have included the masses from the Particle Data Book. (See thesis of P. Schoessow)

Particle	Decay Channel	E610 Mass(Mev/c^2)	Particle Data Mass
ϕ	$\mu^+\mu^-$	1023 ± 1	1019.6 ± .1
ϕ	K^+K^-	1019 ± 1	1019.6 ± .1
ω	$\mu^+\mu^-$	784 ± 1	782.6 ± .2
K_S	$\pi^+\pi^-$	497.5 ±.4	497.7 ± .1

Our measured masses of the various particles appear very close to their data book values. In conclusion, we feel we understand the CCM field well enough to compute accurately.

4.7 Muon Identification.

Muons were identified by hits in the M hodoscope. A muon track was required to be inside or within a certain distance of the boundary of a hit M counter. For the second pass the distance was 7.1 cm in X and 3.6 cm in Y. This was the only requirement for a track to be called a muon during the second pass. For our final J/psi sample the window width was (1 + 20/P) cm. P is the momentum of the track in Gev/c. The quantity 20/P takes into account the multiple scatter in the 3 meters of steel in front of the M hodoscope. For the final J/psi sample 3 other cuts were used. 1) The TDC for the M counter hit was checked to see if it was in time. Since four M counters were ganged into same TDC, a check was made of the other three M counters to see if they had a hit. If one of these had a hit, the TDC was not checked. 2) If the track was inside an H counter by 1 cm, then that H counter had to have a hit. The H Hodoscope did not cover the entire middle section of the lab. It had a horizontal gap 3 cm high and a vertical gap 30 cm wide where the

beam went through (see Figure 3.4). For this reason an H Hodoscope hit was not required. 3) The upstream tracks found in the 80 cm chambers and Y planes of the UI chambers were required to be within 0.8 cm of the primary vertex. This cut did not remove very many tracks because the trackfinder only found vertex associated tracks anyway.

These muons were combined to form muon pairs. Figure 4.2 gives the dimuon mass spectrum from the second pass. With the exception of the resonances ω, ϕ, and ψ, almost all dimuon pairs are either pions and kaons decaying in flight or hadrons punching through the steel. The prompt dimuon continuum was very small as can be seen by comparing our data with that from Anderson et. al. [33]. Their experiment was also performed with the CCM. They studied the rate of prompt dimuon production with a 2 meter piece of steel just downstream of the target to absorb everything but muons. They, therefore, should only see prompt dimuon pairs. Their data give the ratio of the rate of production of nonresonant prompt dimuons to J/psis. Our ratio of nonresonant dimuons to J/psis indicates that only 3% of our dimuon continuum was prompt.

4.8 Final J/psi Sample

The sample of all dimuon events was condensed to 5 tapes of 52,000 two-muon events with mass greater than 2 Gev/c^2. This sample was further condensed to one tape of about 7000 two-muon events with a mass greater than 2.4 Gev/c^2. The trackfinder described in Appendix A was called on this set of events to create the final J/psi sample. Although the low momentum part has no effect on the muons,

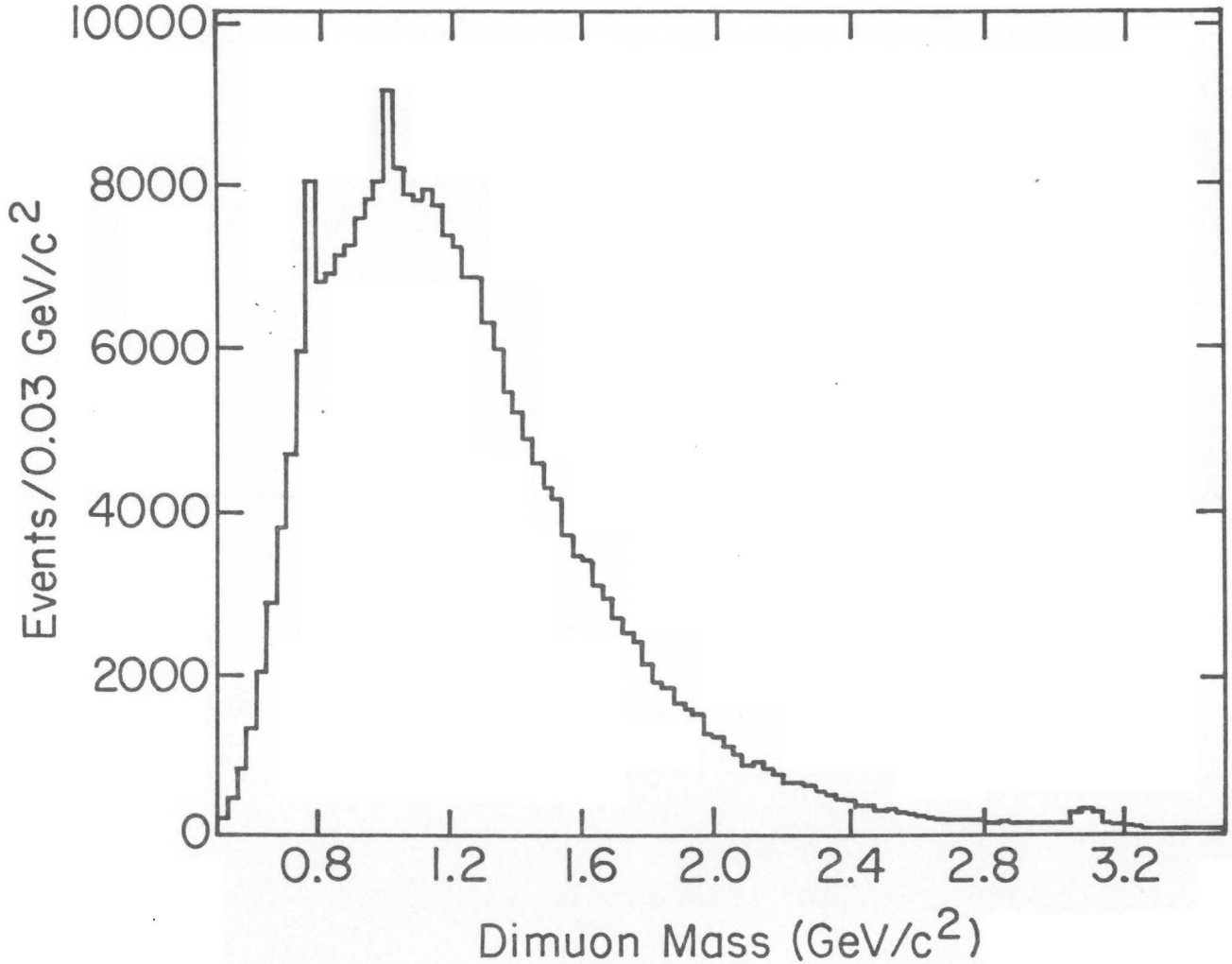

Figure 4.2
The dimuon mass spectrum

the additional weeding in it reduced the background. The track parameters were calculated as accurately as possible by the following procedure. First the muon track was fit using the vertex, the 80 cm points and the UI chamber points. This enabled accurate calculations of the upstream track parameters and the momentum. Next, the track was swum into the drift chambers using a magnet swimmer and a magnet map. This was done to help resolve the 2-fold and 4-fold drift chamber ambiguity described in the apparatus section. The drift chamber hits were searched for using the same two step process previously described. Next, the track was refit using the vertex, the 80 cm points, the UI points and the drift chambers points. Although this procedure used a large amount of computer time per event, the small size of the final J/psi sample justified its use. In order to remove bogus dimuon pairs with one of the muons as a beam particle punching through the steel, the following cut was used. Let P_1 and P_2 be the total momentum of the negative muon and positive muon, respectively. We required

$$(P_2 - P_1)/(P_2 + P_1) > -0.7$$

This removed about 3% of the J/psis with a 34% reduction in the background.

Figure 4.3 is a plot of the dimuon pairs near the J/psi. The background was fitted to a falling exponential. If the J/psi is fitted using one gaussian, then the FWHM of the peak is 66 Mev. One guassian does not fit the peak very well. This is due to wrong and bad drift chamber hits being used. A fit using 2 guassians with the same mean and different FWHM gives a better fit. The FWHM of the two gaussians are 51 Mev and 172 Mev. The fit gives 1264 J/psis.

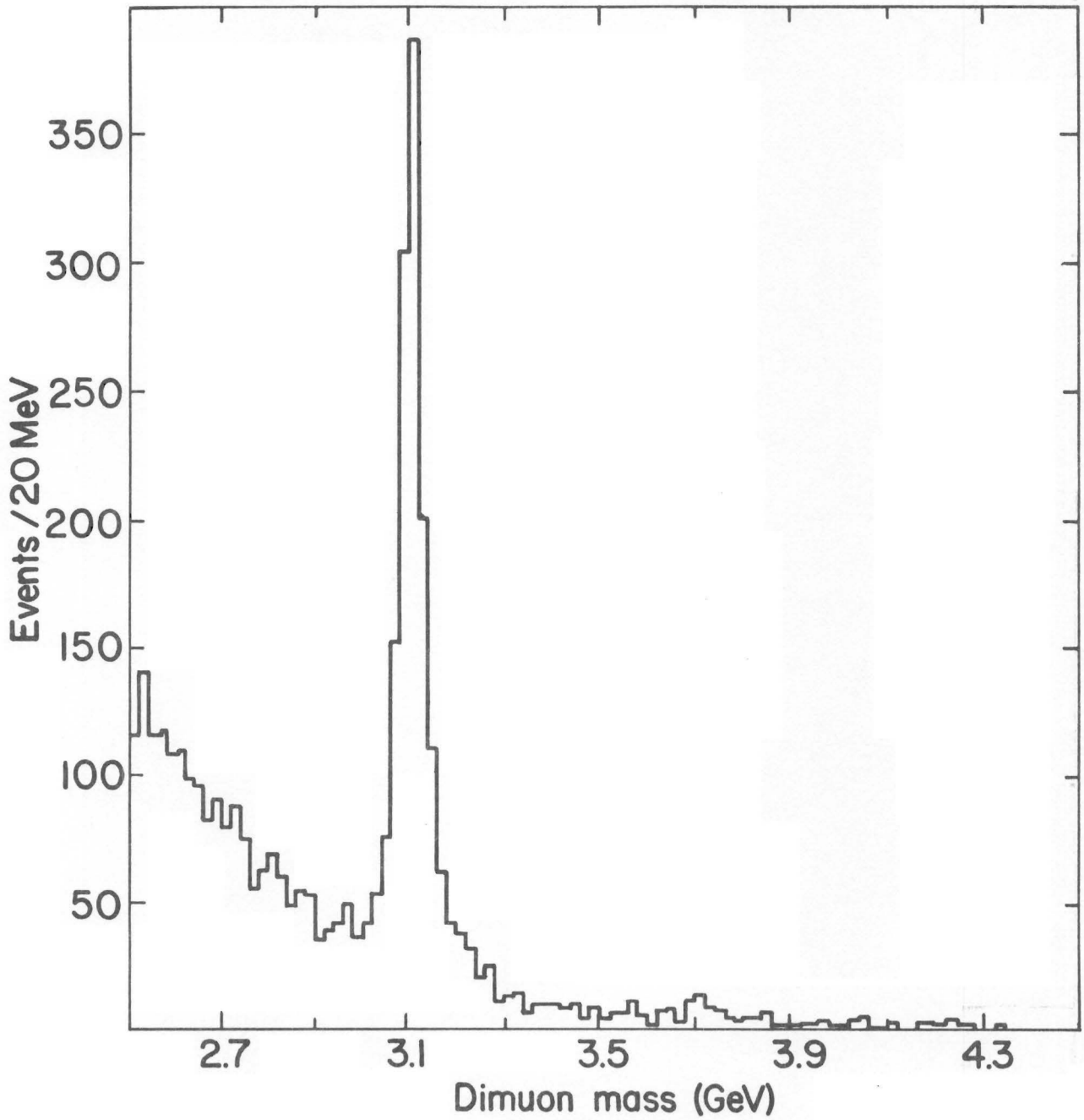

Figure 4.3
The dimuon mass near the J/psi

CHAPTER 5

RESULTS AND CONCLUSION

If J/psi production proceeds by both quark fusion and gluon fusion, then the forward charge should change as a function of the x_F of the J/psi. Arguments presented in the theory section predict that at low x_F gluon fusion would dominate and the forward charge would approach -1. At high x_F, quark fusion would dominate, and the forward charge would be -1/3. Several things could affect these numbers. First, gluon fusion might not completely dominate at low x_F or quark fusion might not completely dominate at high x_F. Second, the process of forming hadrons from these beam quarks may change the numbers from -1 and -1/3. Nevertheless, we expect the forward going charge to become more positive as the x_F of the J/psi increases.

In this thesis, we want to measure the forward charge as a function of the x_F of the J/psi. Rather than trying to measure absolute values, we compare this distribution from events in the J/psi mass region with those in the control region just below the J/psi mass. We then compare the forward charge averaged over the x_F interval with the forward charge of hadrons from all target interactions, not triggered on dimuons. In making the comparisons between different sets of data, we eliminate some of the systematic errors that could be associated with our analysis. Problems with the acceptance for finding all tracks, trackfinding inefficiencies and reinteraction of pions in the target become smaller. We make no claim that we are measuring the charge of a quark or the charge of the beam jet.

5.1 J/psi Events

Figure 4.2 shows the dimuon mass plot with the J/psi peak. The FWHM of the J/psi is 66 Mev. This J/psi sample used for this anaylsis contains 1340 dimuons with masses between 3.02 Gev/c^2 and 3.18 Gev/c^2. In this sample approximately 14% of the events are background. Approximately 97% of the background is caused by either pion or kaon decay or hadron punch through. The nonresonance region around the J/psi is also about 97% hadron punch through or hadron decay in flight. The remaining 3% are Drell-Yan pairs.

5.2 Feynman X Dependence

Figure 5.1 shows the raw x_F dependence of the above sample. We note that the distribution extends beyond $x_F = 0.6$, where Figure 2.6(b) in Chapter 2 indicates gluon fusion and quark fusion become equal. The sharp rise in the number of our raw events near $x = 0$ reflects our acceptance (see Figure 5.2), but the fall off near $x_F = 1$ results from a falling cross section.

The flatness in the acceptance from $x_F = .5$ to $x_F = 1$ is a design feature of the bow tie shape of the Muon Hodoscope. If the gap between the upper and lower sets of counters had been constant at all X positions, then the x_F acceptance would have fallen off at high x_F.

Figure 5.3 gives the acceptance corrected x_F dependence of our sample. The curve superimposed on the data is a fit to the data which will be described below.

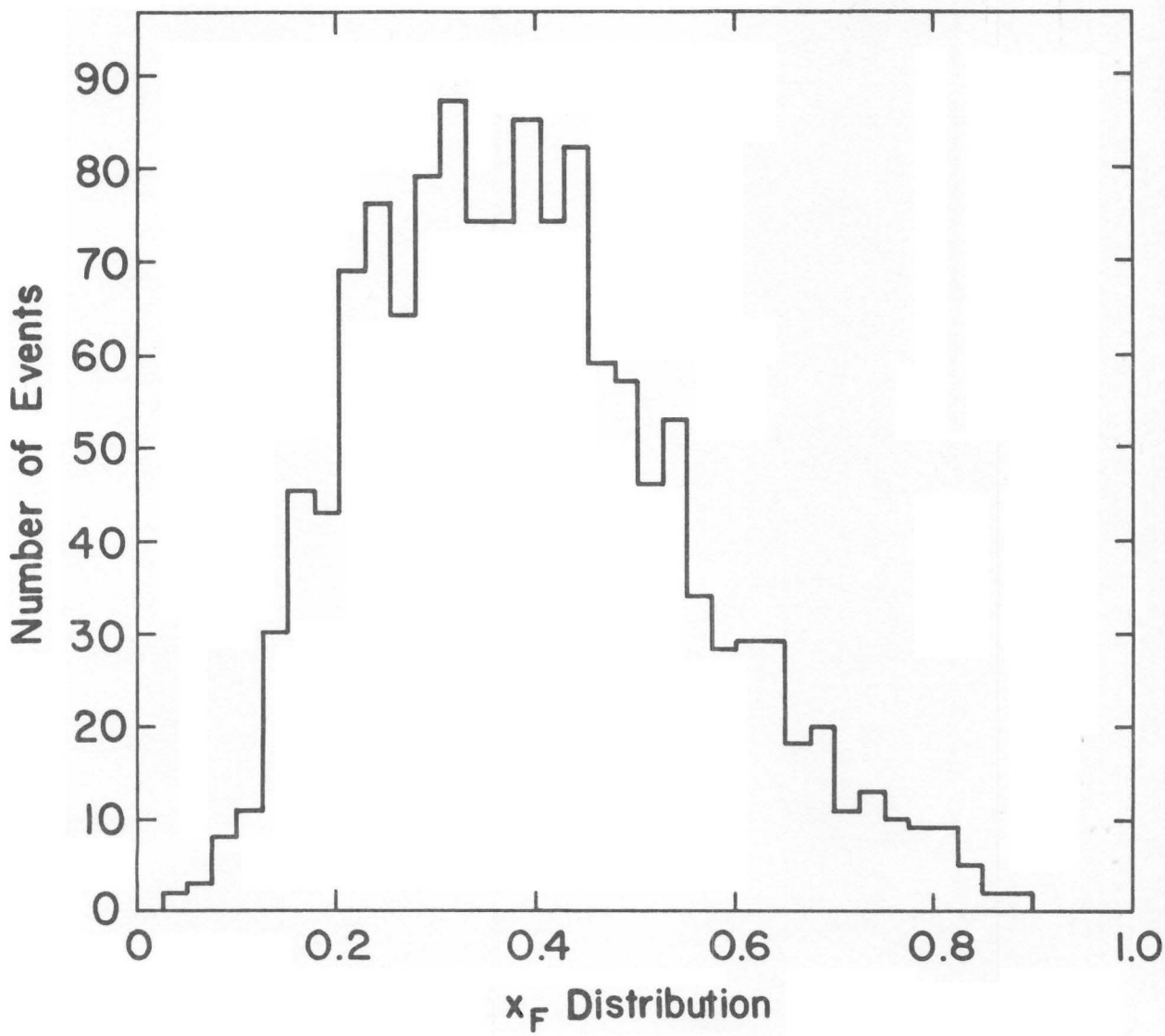

Figure 5.1
x_F of J/psi events with no acceptance correction

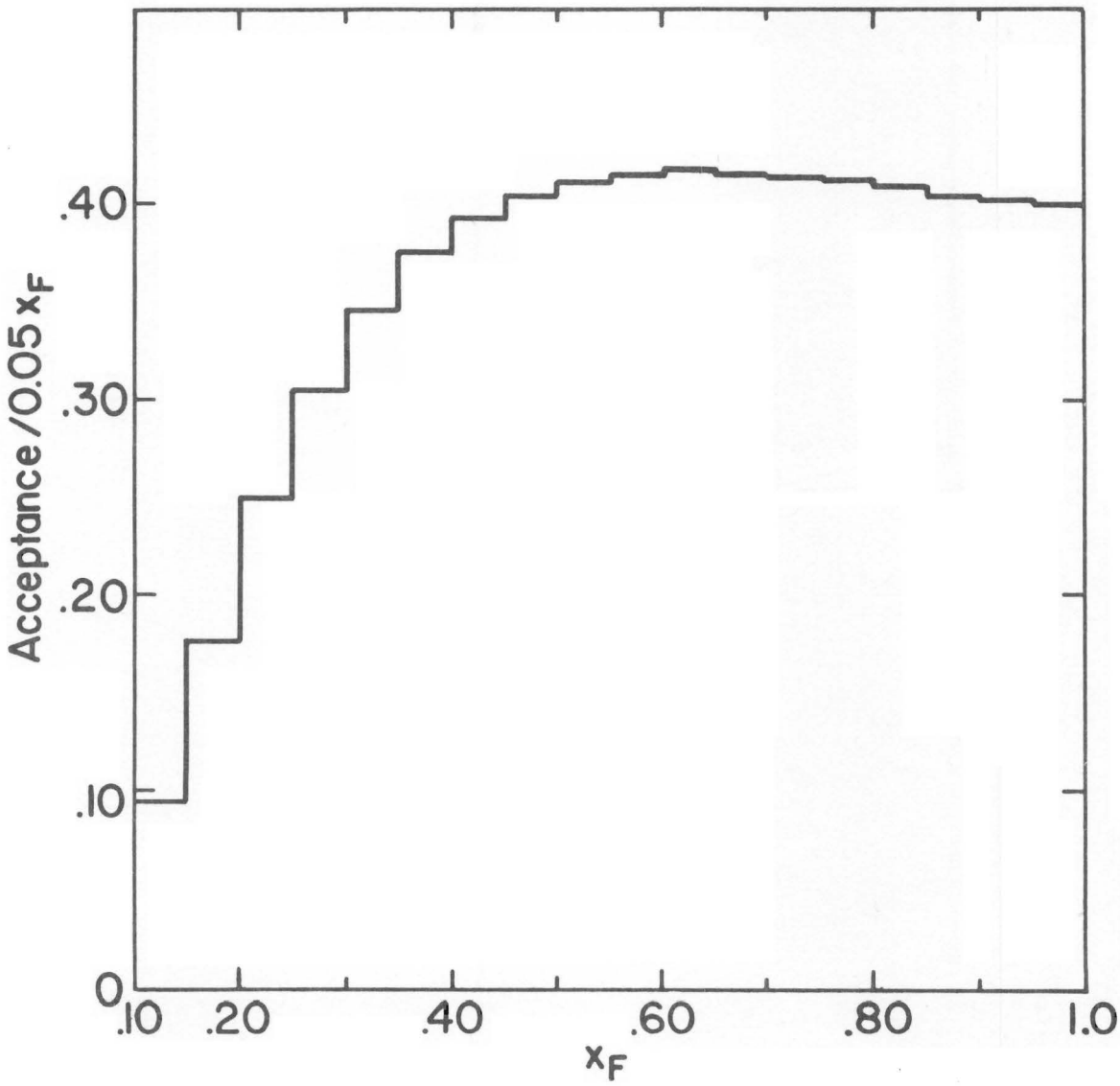

Figure 5.2
J/psi acceptance as a function of x_F

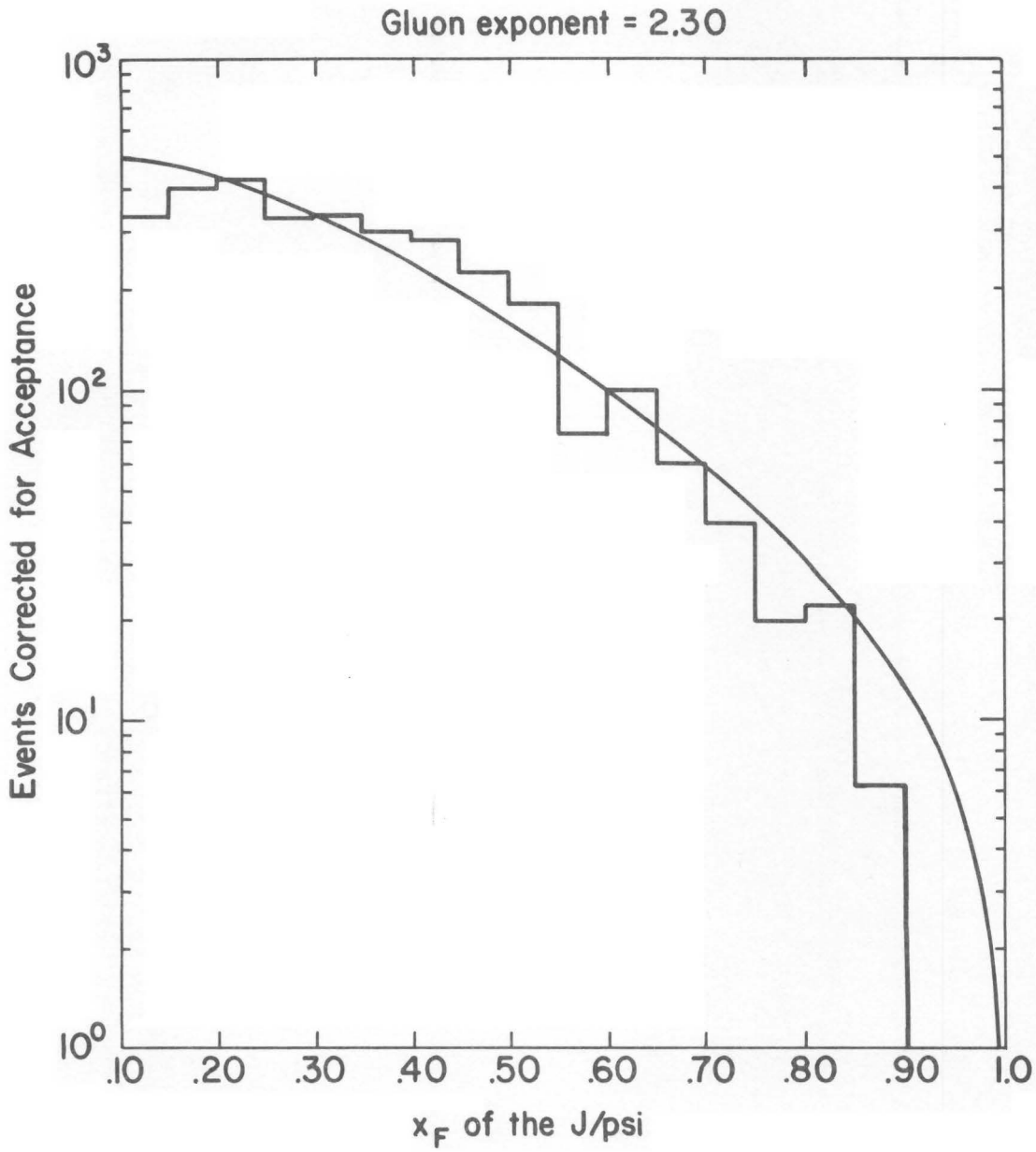

Figure 5.3
x_F of J/psi event with acceptance correction

5.3 Measurement of Forward Charge

In order to determine the forward charge, three methods are used. The first, called charge sum, is to sum up the charge of all the hadrons in the forward direction, i. e. with rapidity in the center of mass frame greater than 0. The "charge measure" was developed by Teper and Maxwell [39] in order to compute the charge of a jet which starts from a fast quark. They felt the method was a way of telling whether an individual jet at Petra started from a quark or antiquark. The method is the following. Let q_1, q_2, ..., q_N be the charges of the hadrons in the forward hemisphere ordered by decreasing rapidity. Let q_1 be the charge of the hadron with the highest rapidity and q_N be the charge of the hadron with lowest rapidity. The charge measure is defined as

$$Q_{CM} = q_1 + \frac{N-1}{N} q_2 + \frac{N-2}{N} q_3 + \cdots + \frac{q_N}{N} \tag{5.1}$$

This method gives the most weight to the leading hadron. The third method, called leading hadron, is to take the charge of the hadron with the highest rapidity as the forward charge. For all three of these methods if there is no hadron in the forward direction, then the forward charge is zero.

A Monte Carlo program determines what effect the acceptance has on the forward charge. The program, described in Appendix C, creates a 3-parameter lookup table which gives the acceptance probability as a function of rapidity y, transverse momentum p_T, and charge q. Figures 5.4 and 5.5 are plots of the acceptance vs p_T and rapidity. Figure 5.4 is the acceptance for negative particles, while Figure 5.5 is for positive particles. The step size in p_T was the same for the lookup table and the two figures, while the step size in rapidity was

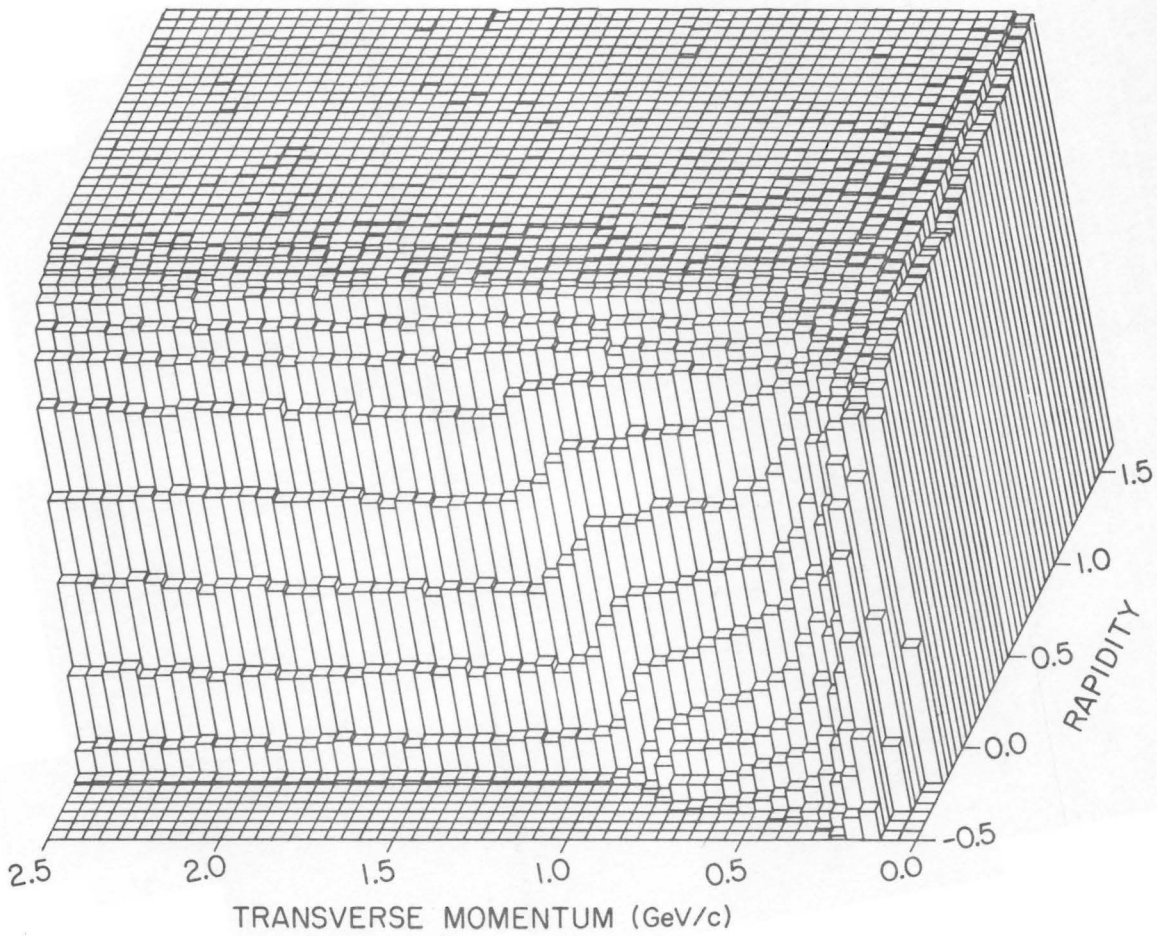

Figure 5.4
Acceptance vs p_T and rapidity, Q = -1

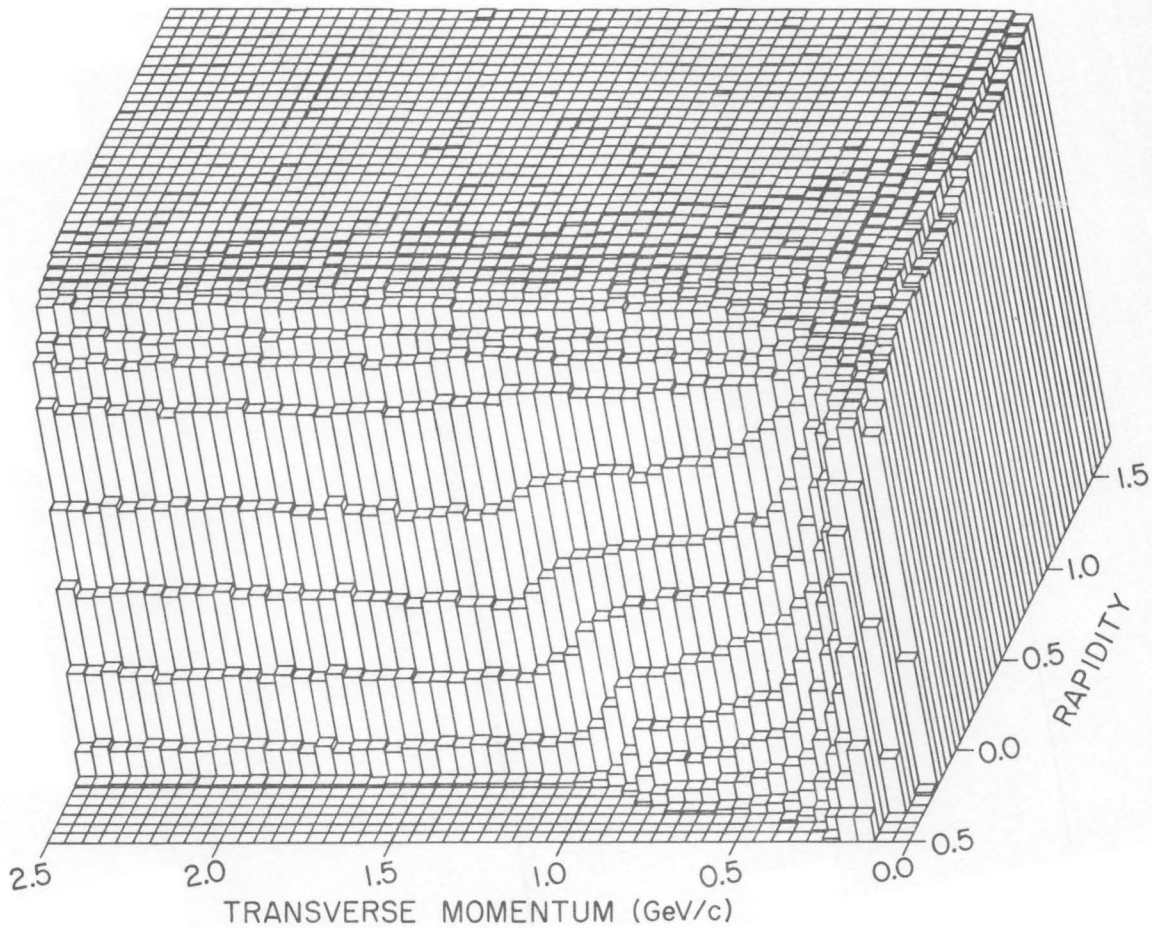

Figure 5.5
Acceptance vs P_T and rapidity, Q = 1

twice as large in the figures as it was in the lookup table. At a rapidity of 0.0 the average acceptance is about 73%. The acceptance at $y = p_T = 0$ is about 90% and falls off gradually to 55% at $y = 0$, $p_T = 2.5$ Gev/c. The acceptance rises to over 96% at $y = .3$ and to about 99% at $y = 1.0$. The acceptance program was carried out to a rapidity of 4.9 in the center of mass frame. The acceptance vs rapidity was fairly flat for rapidity greater than .5.

The charge distribution can be corrected for acceptance by the following procedure. After a track is found, the rapidity and p_T are computed. Then using the lookup table, the acceptance for finding a track with that x_F, p_T and charge is found. We then divide the charge by the acceptance to get the acceptance corrected charge, which is used in place of the true charge in the formulas. This procedure gives us the acceptance corrected forward charge. For instance, acceptance corrected forward charge via method 1 is the following:

$$Q = \frac{q_1}{a_1} + \frac{q_2}{a_2} + \dots + \frac{q_N}{a_N}$$

where a_i is the acceptance for the particle i with charge q_i. This method takes into account any charge bias that could have been introduced either by geometric acceptance or by variations in chamber efficiencies.

5.4 Data

All the tracks found by the trackfinder as described in Appendix A are used to compute the forward charge with 2 exceptions. The following tracks are not used.

1. The two muons comprising the dimuon are not used. A third muon, if it is there, is treated as a hadron. As stated in the theory section, the probability of an additional prompt muon in J/psi production is very small, less than 1%. Approximately 6% of our J/psi events have a third muon. In almost all cases this third muon is either a hadron punch through or pion decay in flight rather than a prompt muon. Hence, these muons are treated as hadrons.

2. If the track points farther than 0.8 cm in X or Y away from the primary vertex, the track is not used.

The forward charge distributions are shown for the total J/psi sample in Figures 5.6 to 5.11. Figure 5.6 is a histogram of the forward charge computed by summing the charges in the forward direction. The number of entries is 1340. The average is -.378 with a standard deviation of 1.37. Figure 5.7 is the acceptance corrected version of 5.6. Its average is -.377 with a standard deviation of 1.42. Figure 5.8 is a histogram of the charge measure (defined by Equation 1 above) for each event. The average of the histogram is -.294 with a standard deviation of 1.04. Figure 5.9 is a histogram of the acceptance corrected charge measure. Its average is -.297 with a standard deviation of 1.04. Figure 5.10 and 5.11 are histograms of the forward charge computed by using the leading hadron method. Figure 5.10 used the raw data while Figure 5.11 is corrected for acceptance. The average of Figure 5.10 is -.197 with a standard deviation of .98. The average of Figure 5.11 is -.201 with a

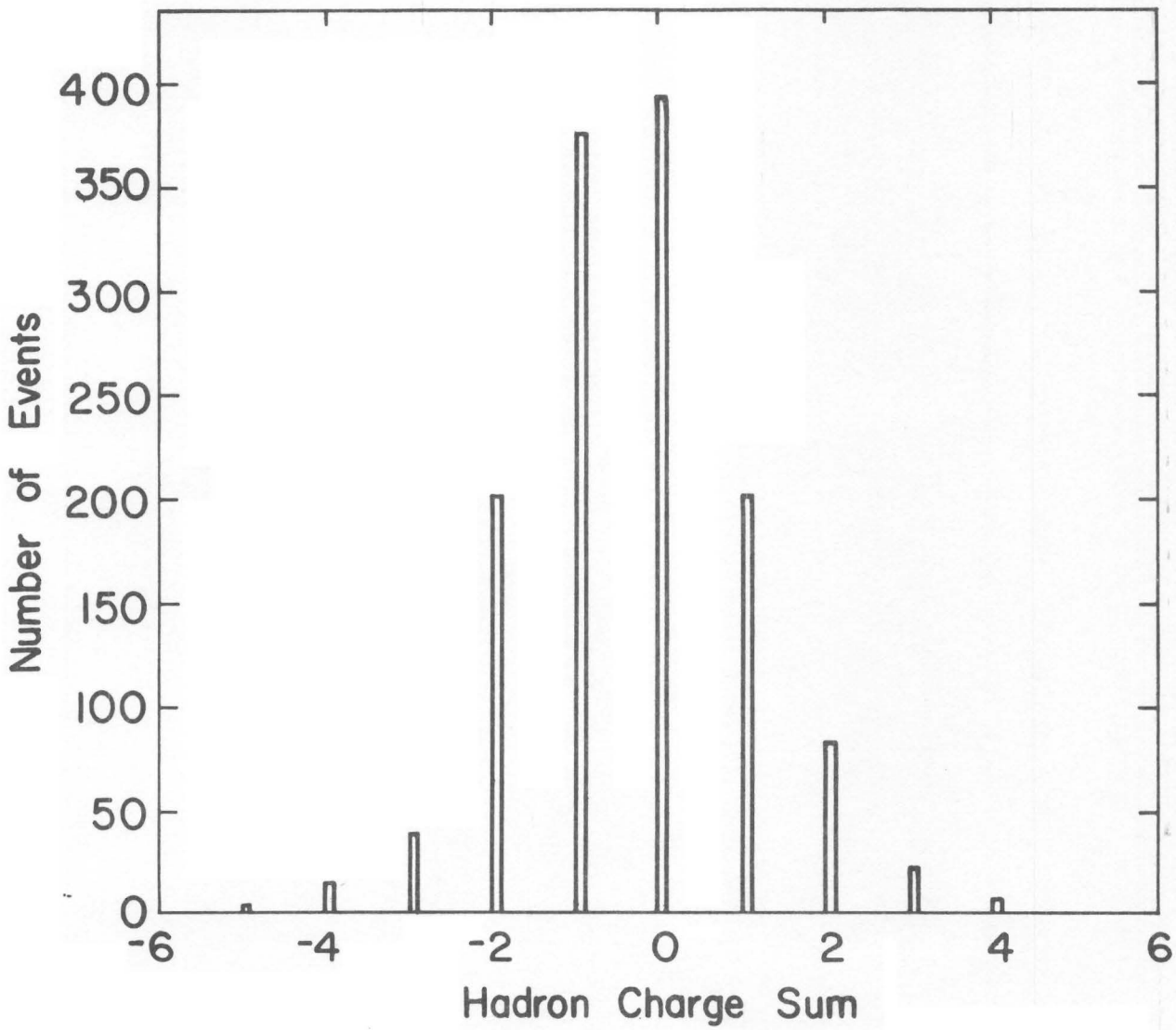

Figure 5.6
Charge sum in forward hemisphere for J/psi events

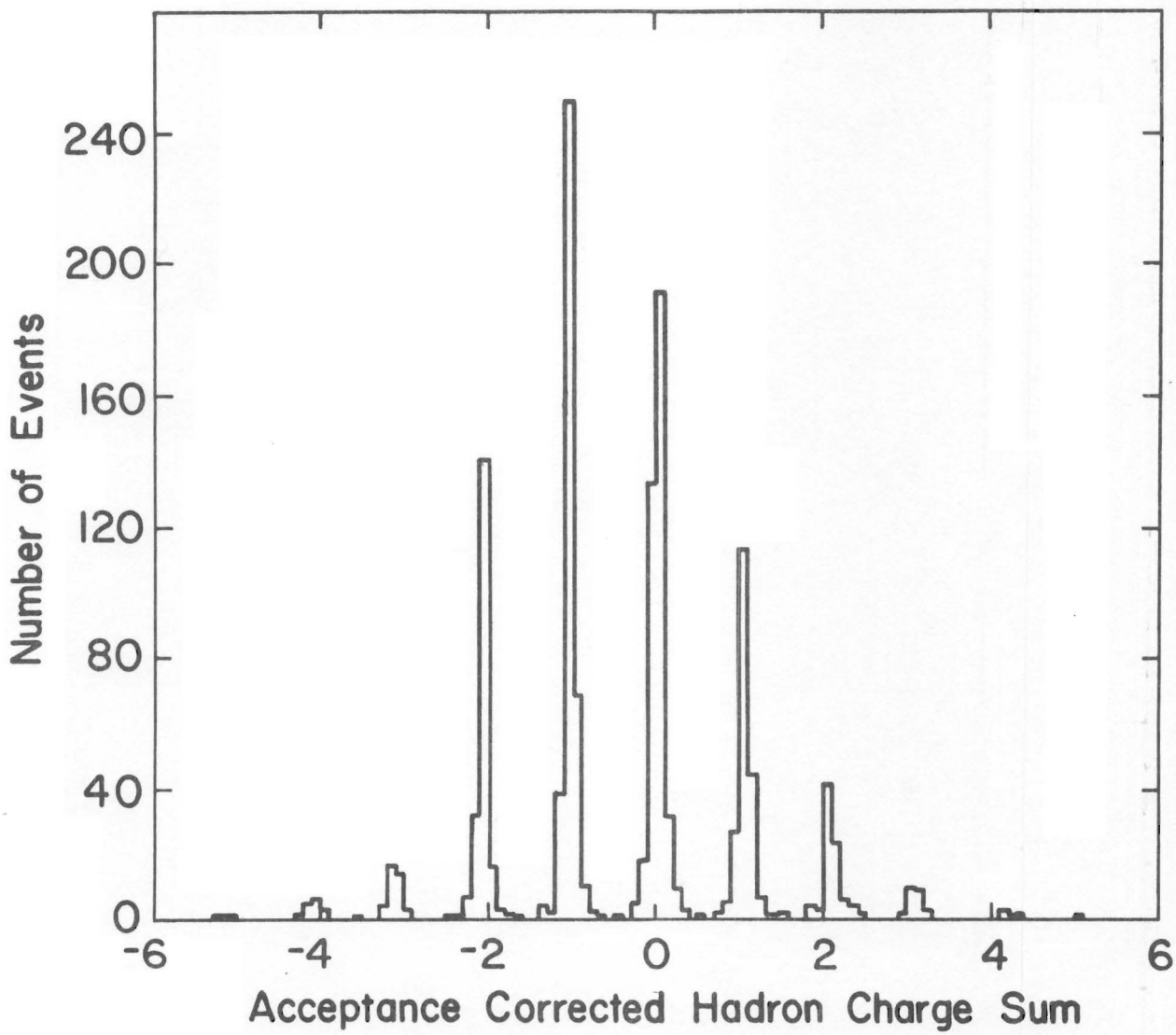

Figure 5.7
Acceptance corrected charge sum in
forward hemisphere for J/psi events

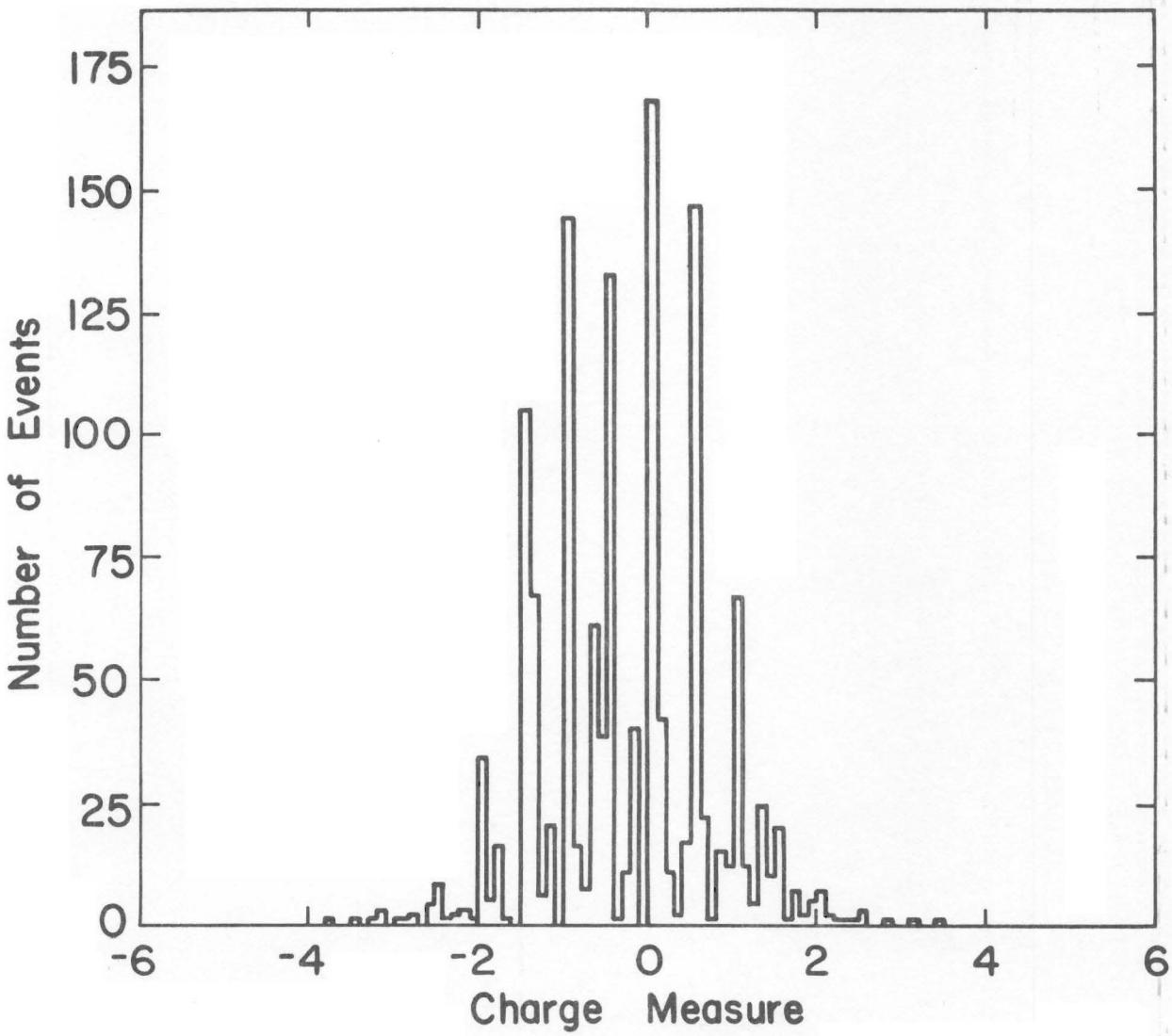

Figure 5.8
Charge measure in forward hemisphere for J/psi events

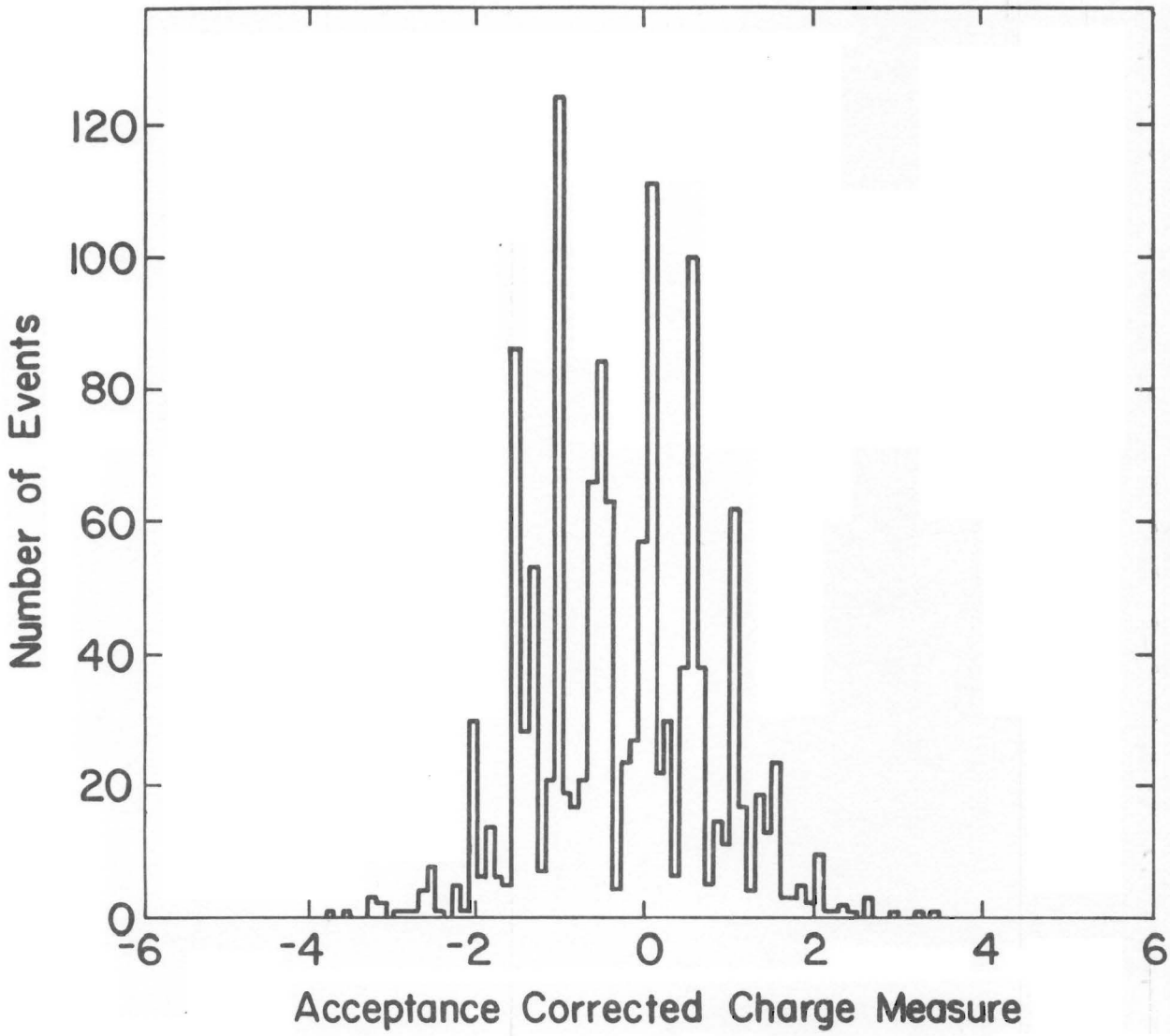

Figure 5.9
Acceptance corrected charge measure
in forward hemisphere for J/psi events

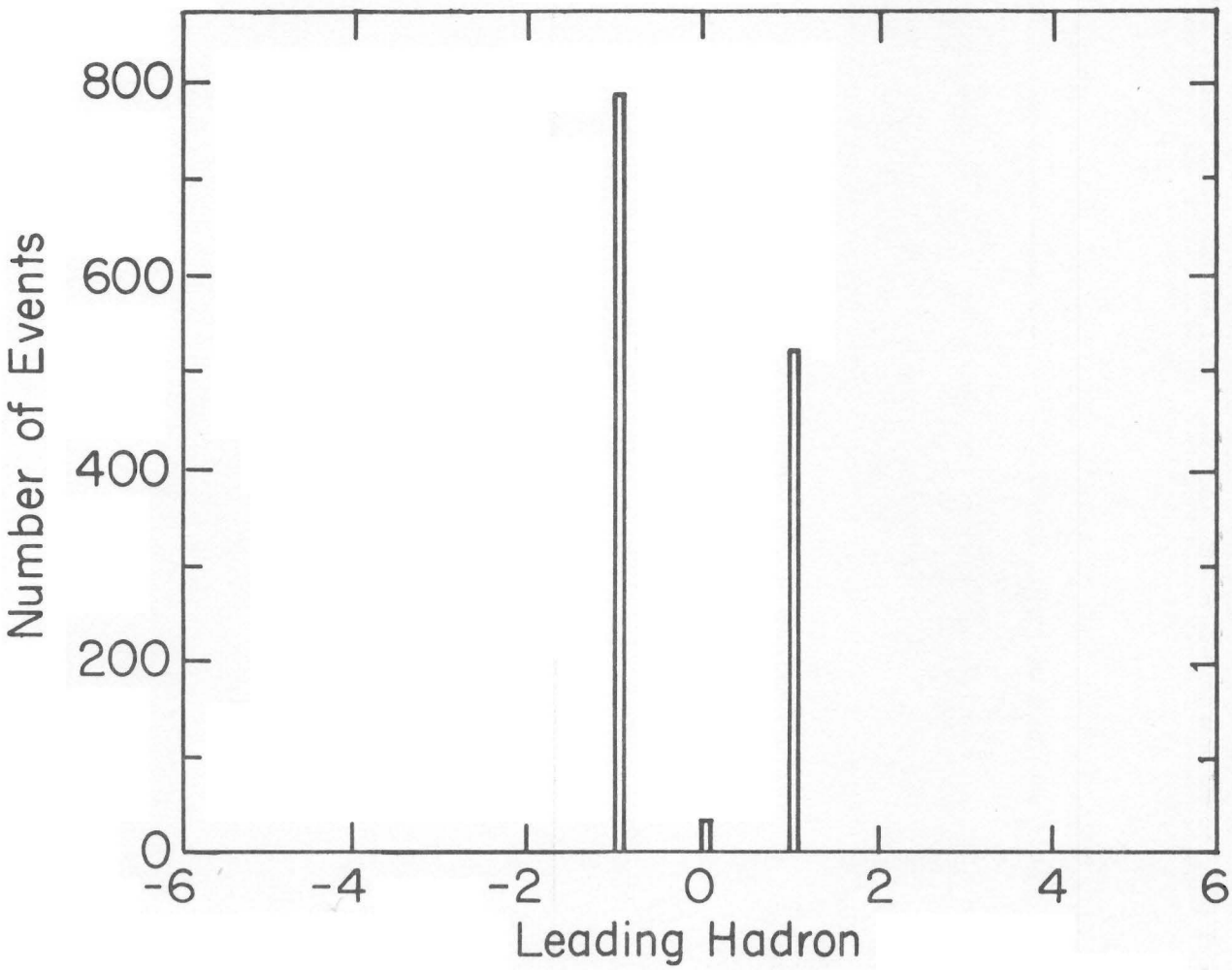

Figure 5.10
Leading Hadron for J/psi events

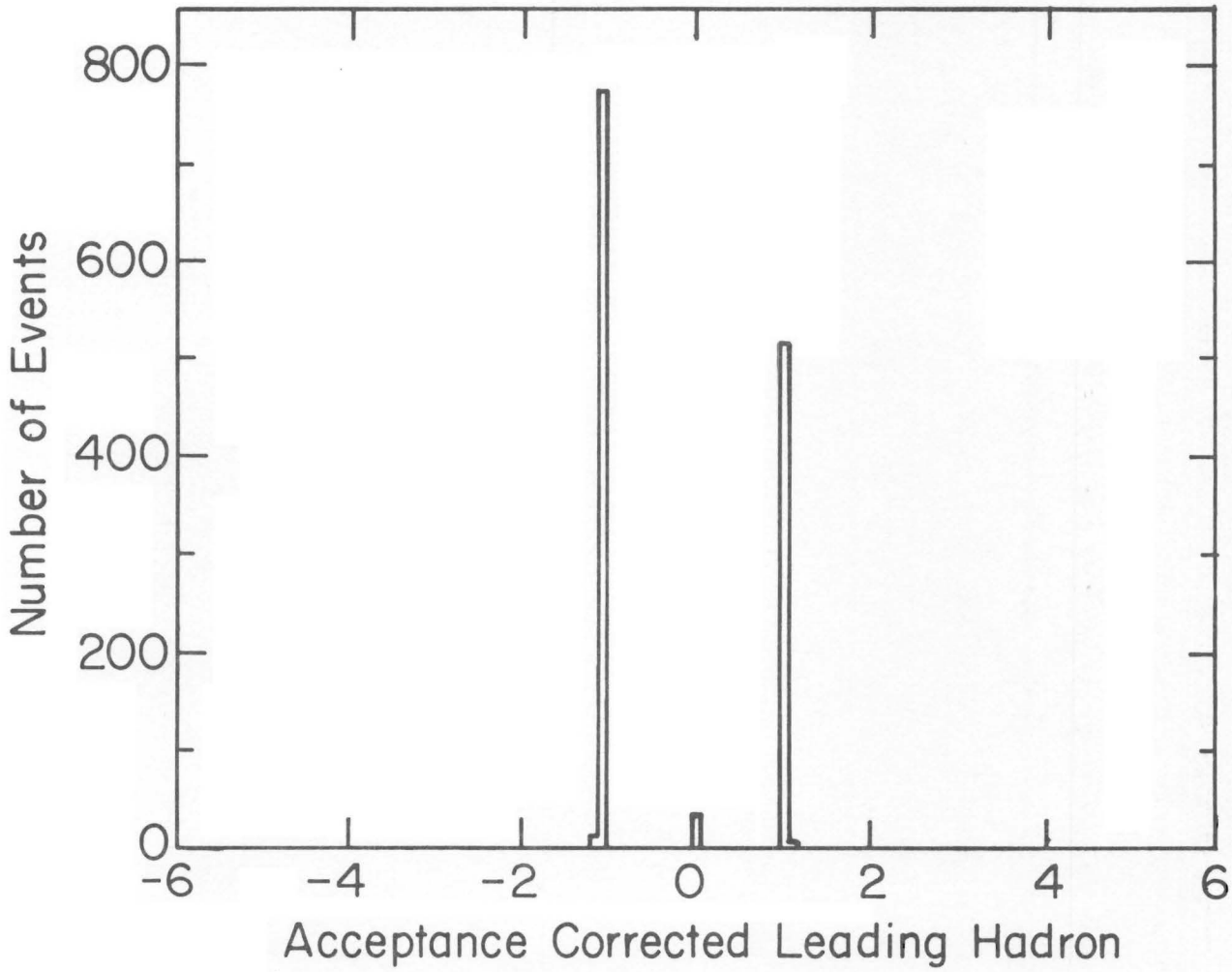

Figure 5.11
Acceptance corrected leading hadron for J/psi events

standard deviation of .99.

The above numbers show that correcting the forward charge for acceptance makes no difference. This fact is true for all the charge distributions involved in this thesis. Hence, from now on we shall ignore the acceptance corrections.

Figures 5.6 through 5.11 illustrate how we compute our statistical errors. The standard deviation for Figure 5.6 is 1.37. With 1340 events in the plot, the statistical error in the average forward charge of -.376 is $1.37/\sqrt{1340} = .037$. The statistical error of the charge measure is $1.04/\sqrt{1340} = .028$. The error for the leading hadron method is calculated the following way. We assume the distribution of + and - particles behaves according to a binomial distribution. For this error analysis we assume that the leading particle is either positive or negative. That is not quite true because about 3% of the J/psi events have no hadron in the forward direction. Let P+ be the probability that an event will have a leading positive particle. Because we do not measure neutral particles and assume there is always a leading hadron, P- = 1 - P+. For our data P- = .602 and P+ = .398. Hence, $< Q_{LP} > = (P+) - (P-) = -.204$. Let σ_P be the one sigma error on P+. Then the formula for a 1 sigma error on a binomial distribution is

$$\sigma_P = \sqrt{(P+*P-)/N} = .0135$$

If σ_P is added to P+ and subtracted from P-, then the forward charge changed by 1 sigma becomes

$$< Q_{LP} > = -0.204-2.(\sigma_P) = -.204-.027 = -.231$$

Hence, the 1 sigma error on the forward charge is .027. These methods of computing error were used for all the forward charge

numbers we quote.

In order to compute the forward charge as a function of x_F, we divided the J/psi data into four x_F bins. The average x_F and limits of the bins are the following.

TABLE 1

AVERAGE X_F	LOW X_F	HIGH X_F	# OF EVENTS
0.22	0.00	0.30	424
0.37	0.30	0.44	436
0.49	0.44	0.55	236
0.66	0.55	1.00	202

Figure 5.12 (a,b,c) are plots of the forward charge for the 4 bins using the 3 previously described methods. Approximately 14% of the J/psi events are background. A number for the forward charge for the background has been computed and subtracted from the raw numbers to give the numbers in the plots. This subtraction will be described later.

For each of the plots 5.12(a,b,c) the forward charge is more negative in the high x_F bin than the low x_F bin. The effect seems to be a 2 sigma effect using the charge sum method. The effect is about 1.5 sigma and 1 sigma using the charge measure and leading hadron, respectively.

The nonresonance dimuon pairs near the J/psi mass arise from either meson decay in flight or hadron punch through. The associated forward charge should be similar to the forward charge from an ordinary hadronic interaction run. A separate "interaction run" was made in which the trigger was was simply a large pulse height in the counters immediately downstream of the target. The forward charge accompanying dimuons with mass between 2.5 Gev/c^2 and 2.9 Gev/c^2 is

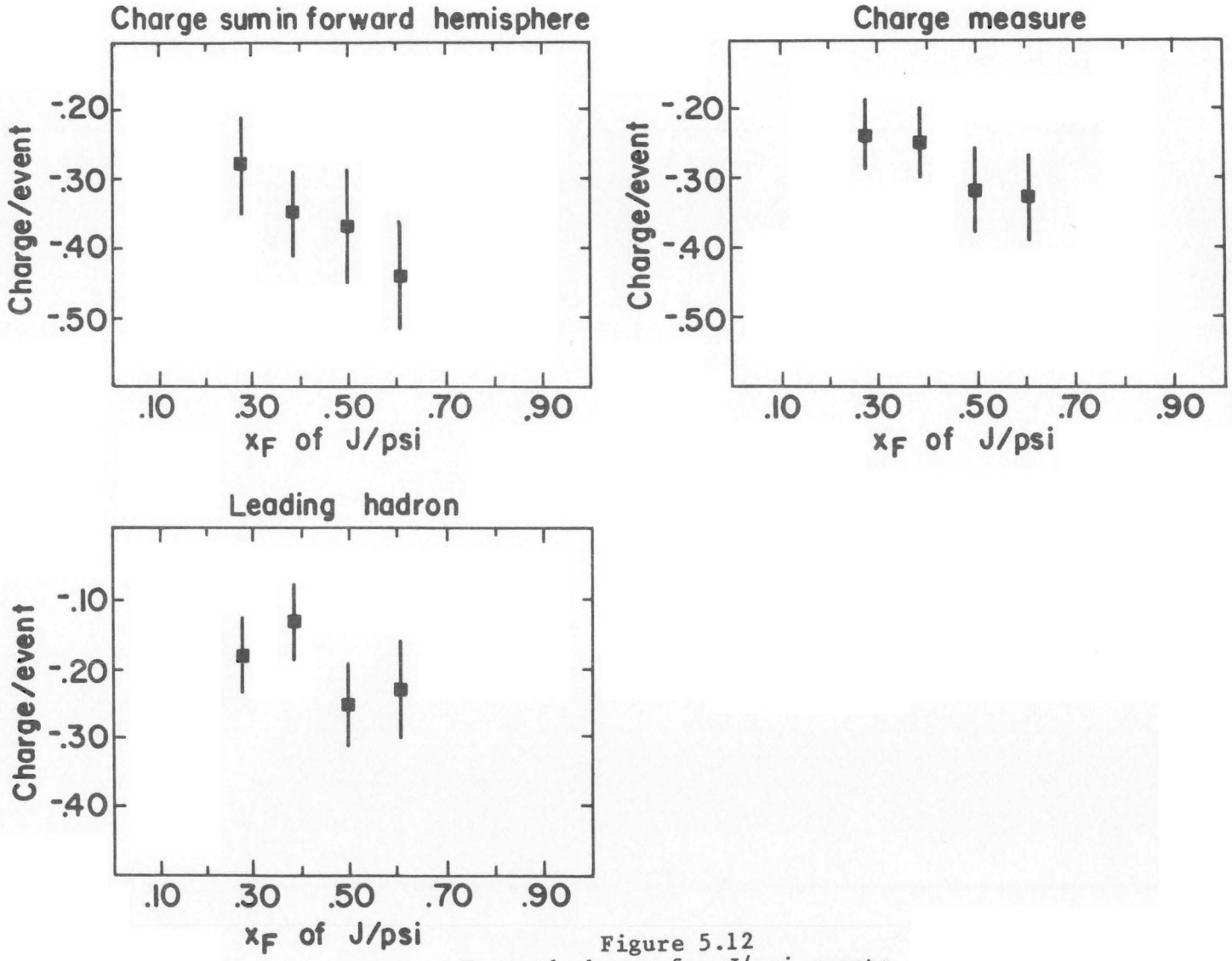

Figure 5.12
Forward charge for J/psi events
as a function of x_F of the J/psi

given below along with the forward charge from an interaction run. We have also included the raw J/psi numbers.

TABLE 2

Forward charge averaged over x_F

DATA	SUM HADRONS	CHARGE MEASURE	LEADING HADRON
PSI	-.38 ± .04	-.29 ± .03	-.20 ± .03
CONTROL DIMU	-.57 ± .03	-.43 ± .02	-.28 ± .02
INTERACTION	-.62 ± .02	-.46 ± .01	-.25 ± .01

About 3% of the dimuon data consists of Drell-Yan pairs. If the dimuon sample were pure hadron decay in flight or hadron punch through, then its forward charges would be about .015 more negative.

Figure 5.13(a,b,c) is a plot of the forward charge vs x_F of the dimuons using data from the dimuon control region. The definition of the bins is the same as for the J/psi data. The forward charge vs x_F is consistent with being flat in x_F.

The running conditions for the dimuon data and the interaction data were different. During the dimuon running, the intensity was about 2.5 million incident π^- during a 1.5 second spill. The high intensity caused the efficiency in the beam region to be lower than in the nonbeam region. Also, the intensity caused the efficiency of the chambers to fall slightly. The intensity for an interaction run was about 50,000 per 1.5 second spill; hence the efficiency of the chambers did not drop in the beam region. We note, however, that the forward charge for an interaction run is similar to that for dimuons between 2.5 and 2.9 Gev/c^2. This indicates that the drop of efficiency in the beam region did not affect the measurement of the forward charge. This conclusion agrees with the Monte Carlo result

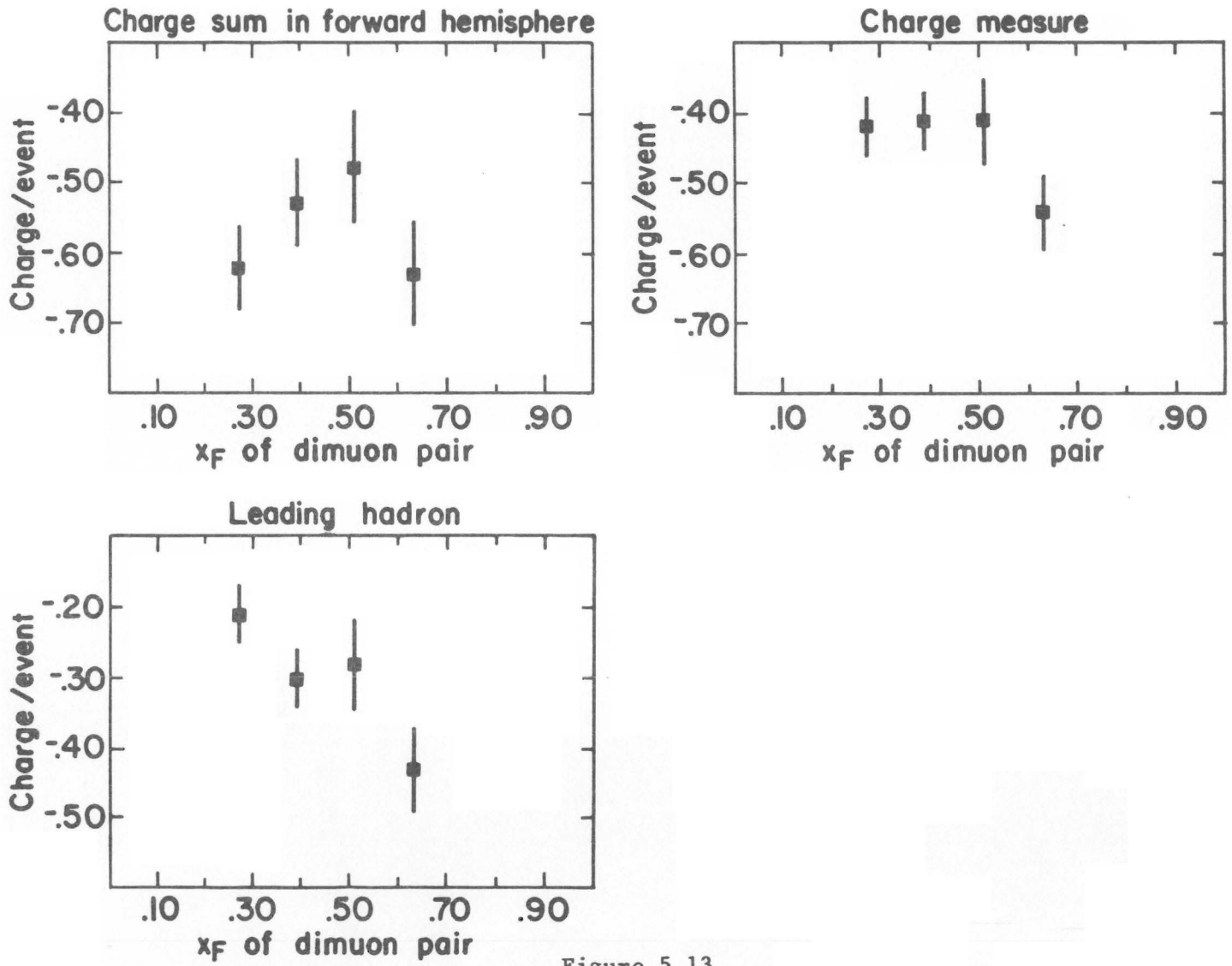

Figure 5.13
Forward charge for dimuons with $2.5 < M_{\mu^+\mu^-} < 2.9$
as a function of x_F

that the apparatus has no charge bias.

The forward charges for the J/psi plotted in Figure 5.12 were corrected for background. Approximately 14% of the dimuon events with a mass between 3.02 and 3.18 are background. We assume these background events have the same charge sum as events in the control region, i.e. -.57. The raw charge sum, $< Q_{RCS} >$, for each bin were corrected to get the plotted charge sum, $< Q_{CS} >$ using the following formula.

$$0.86 < Q_{CS} > + (0.14)(-0.57) = < Q_{RCS} >$$

Solving for $< Q_{CS} >$ we get

$$< Q_{CS} > = (< Q_{RCS} > + (.14)(.57))/.86 \qquad (5.2)$$

$< Q_{CS} >$ is the charge sum for the bin if all the events in the bin were J/psi events. To get the background corrected charge measure, we use Formula 5.2 with -0.57 replaced by -.43 and $< Q_{RCS} >$ replaced by the raw charge measure. The charge for the leading hadron plotted in 5.12c is also corrected for background by the same procedure.

5.5 Decay from Higher Lying States

As discussed in the thesis of S. Hahn, approximately 40% of the psis are not produced directly. About 30% of them come from the decay of $\chi \rightarrow \psi\gamma$, and about 10% of them come from the decay $\psi' \rightarrow \psi\pi\pi$. In our plots of x_F vs forward charge, the relevant x_F is the x_F of the object which was produced via quark or gluon fusion. We don't know this number for those 40% of the events in which the ψ was not produced directly. A Monte Carlo program was written in order to determine the difference in x_F between the $c\bar{c}$ pair produced and the J/psi we measure. We have generated both ψ' and χ

production with the following x_F and p_T distributions [18].

$$x_F \sim (1 - x_F - .2)^{1.65}$$

$$p_T \sim p_T * \exp(-1.98 p_T)$$

We then let the ψ' decay into $\psi\pi^+\pi^-$ and χ decay into $\psi\gamma$. We then determined whether the ψ would be accepted by our apparatus by decaying it into $\mu^+\mu^-$. All decays were isotropic. If the J/psi was accepted, we calculated the x_F of the J/psi. The difference between the x_F of the generated ψ' or χ and the x_F of the ψ is the error in our x_F measurement. The average x_F of the ψ is about 0.05 $\pm$ .05 lower than the x_F of the higher lying states. The average difference between the x_F of the ψ' or χ and the ψ for the 4 bins is given in the table below.

TABLE 3

BIN	$\langle x_F \psi \rangle$	$\langle x_F \chi \rangle - \langle x_F \psi \rangle$	$\langle x_F \psi' \rangle - \langle x_F \psi \rangle$
1	0.22	0.028	0.040
2	0.37	0.046	0.066
3	0.49	0.057	0.087
4	0.66	0.063	0.100

J/psi production from higher lying states smears out and decreases the measured x_F.

5.6 Comparison with WA11

The WA11 experiment at CERN [40] reported the forward charge computed by the charge sum method for J/psis, dimuons with mass greater than 3.85 Gev/c^2, and an interaction run. WA11 used a 190 Gev/c π^- beam on a Be target. This is the only other experiment at present which has studied dimuon production by a hadron beam without a beam dump immediately downstream of the target. They

have approximately 42,000 J/psis and about 2000 dimuon pairs with mass above 3.85 Gev/c^2 which they state are Drell-Yan pairs. They estimate a 15% contamination in their J/psis and Drell-Yan pairs. Their results for the charge in the forward direction for the Drell-Yan, J/psis, and interaction are $-.36 \pm .05$, $-.60 \pm .08$, $-.76 \pm .1$. These numbers have been corrected for experimental efficiency. The overall normalization of their numbers seems about .15e more negative than ours. The reason for this discrepancy is not clear. Since our target was a solid block of Be representing 12.5% of an interaction length, we might expect 6% of the hadrons to interact again and dilute the charge. The WA11 target had a total of 14% of an interaction length segmented in 3 pieces. The segmenting of the target may have resulted in fewer secondary interactions. Whereas WA11 made a correction to their forward charge because of deadeners in the beam region, we found no charge bias due to reduced efficiency in the beam region. Problems for either experiment in understanding the acceptance could cause the forward charges to differ.

An important point of their data is the difference between the J/psi, Drell-Yan and interaction events. They see a difference in forward charge between J/psi events and interaction data of -.16e. Our difference is $-.23 \pm .05$. They see a difference in forward charge between interaction data and Drell-Yan, which is quark fusion, of -.4. If their Drell-Yan sample had been pure, then the difference in forward charge between their Drell-Yan data and interaction data would have been -.47.

5.7 Calculation of Forward Charge for the Four Bins

As stated in the theory section, J/psi production is dominated by gluon fusion at low x_F and quark fusion at high x_F. This should lead to a rise in the forward charge as the x_F of the J/psi increases. To determine the amount the forward charge should change in our four x_F bins due to the change in the amount of quark fusion, we have theoretically calculated the percentages of quark fusion to gluon fusion in our four x_F bins. To do this, we have used the model described by Gluck et. al. [22], Jones and Wyld [23], and Barger et. al. [24]. In this model they have assumed J/psi production takes place by both quark and gluon fusion via Diagrams 2.4a and 2.5(a,b,c). We will give the equation to calculate the rates of quark and gluon fusion in our data.

The production of J/psis via quark fusion comes from the fusion of a quark and an antiquark with combined energy equivalent to a mass between the J/psi mass and the mass of a pair of charmed mesons. We have the following cross section

$$\frac{d\sigma^{\pi p}}{dx_F} = \sum_{q=u,d,s} \int_{4m_c^2}^{4m'^2} dQ^2\, \sigma^{q\bar{q}\to c\bar{c}}(Q^2)\, \frac{1}{Q^2}\, \frac{x_\pi x_p}{x_\pi + x_p}$$

$$\left[q_\pi(x_\pi)\, \bar{q}_p(x_p) + \bar{q}_\pi(x_\pi)\, q_p(x_p) \right]$$

where

1. $m_C = 1.55$ Gev/c^2, the charmed quark mass

2. $m' = 1.853$ Gev/c^2

3. $x_{\pi,p} = (\mathrm{sqrt}(x_F^2 \pm 4Q^2/s) + x_F)/2.$

4. q_π and q_p are the quark distribution functions for pions and protons.

The cross section for J/psi production by gluon fusion is

$$\frac{d\sigma_{gg}^{\pi p}}{dx_F} = \int_{4m_c^2}^{4m'^2} dQ^2 \sigma^{gg\to c\bar{c}}(Q^2) \frac{1}{Q^2} \frac{x_\pi x_p}{x_\pi + x_p} G_\pi(x_\pi, Q^2) G_p(x_p, Q^2)$$

where G_π and G_p are the gluon distribution functions for the pion and proton. Using the Feynman graphs 2.4(a) and 2.5(a,b,c) $\sigma^{gg\to c\bar{c}}(Q^2)$ and $\sigma^{q\bar{q}\to c\bar{c}}(Q^2)$ can be evaluated. They are

$$\sigma^{q\bar{q}\to c\bar{c}} = \frac{2}{9} \frac{4\pi\alpha_s^2}{3Q^2} \left(1 + \frac{\gamma}{2}\right)(1-\gamma)^{1/2}$$

and

$$\sigma^{gg\to c\bar{c}} = \frac{\pi\alpha_s^2}{3Q^2} \left[\left(1 + \gamma + \frac{\gamma^2}{16}\right) \ln\left(\frac{1 + (1-\gamma)^{1/2}}{1 - (1-\gamma)^{1/2}}\right) - \left(\frac{7}{4} + \frac{31}{16}\gamma\right)(1-\gamma)^{1/2}\right]$$

where

1. α_s is the strong coupling constant. For computing the percentage of quark fusion to gluon fusion this constant drops out.

2. $\gamma = 4mc^2/Q^2$

The quark distribution functions were taken from NA3 [5]. The proton valence quark distribution functions are

$$u_p(x) = 2.25x^{-.5}(1-x)^{3.2}$$

$$d_p(x) = 1.25x^{-.5}(1-x)^{4.2}$$

The proton sea quark distribution functions are

$$\bar{u}_p(x) = \bar{d}_p(x) = 2s_p(x) = 2\bar{s}_p(x) = .37(1-x)^{9.4}$$

For the π^-, the valence quark distribution functions are the following.

$$d_{\pi}(x) = \bar{u}_{\pi}(x) = .55x^{-0.6}(1-x)^{0.9}$$

The pion sea quark distribution functions are the following.

$$\bar{d}_{\pi}(x) = u_{\pi}(x) = 2s_{\pi}(x) = 2\bar{s}_{\pi}(x) = .19x^{-1}(1-x)^{5}$$

For the gluon distribution function we take the following. (These gluon distribution functions assume half the momentum of the hadron is carried by gluons.)

$$G_{p,\pi}(x) = ((n+1)/2)x^{-1}(1-x)^{n}$$

For protons we let n = 5 as derived by V. Barger et. al. [24] For pions we let n = 2, 2.38, 3, and 4. V. Barger derived n = 3 while NA3 [41] derived n = 2.38.

Figure 5.14 is a plot of $d\sigma/dx_F$ (arbitrary normalization) for $c\bar{c}$ production from gluon fusion, pion $\bar{u}$ production, pion d production, and pion sea production. Again we see that around $x_F = 0.6$, quark fusion starts becoming the dominant mechanism. For this plot the pion gluon distribution exponent is 3.0. The total percentage of quark fusion and gluon fusion is 37% and 63%, respectively.

Using the above formulas, we have studied our x_F dependence of our J/psis to determine if it is consistent with NA3's result. As previously stated Figure 5.3 gives the acceptance corrected x_F dependence of the data. The curve superimposed on the data is a sum of the theoretical predictions using the above equations for quark fusion and gluon fusion with the gluon distribution exponent = 2.3. In order to determine this exponent, we have done a fit to the data via the following procedure. The fit was made using data from $0.1 < x_F < 0.9$. (If the limits had been from $0.0 < x_F < 1.0$, the result would not have changed). First, we pick a power of the gluon

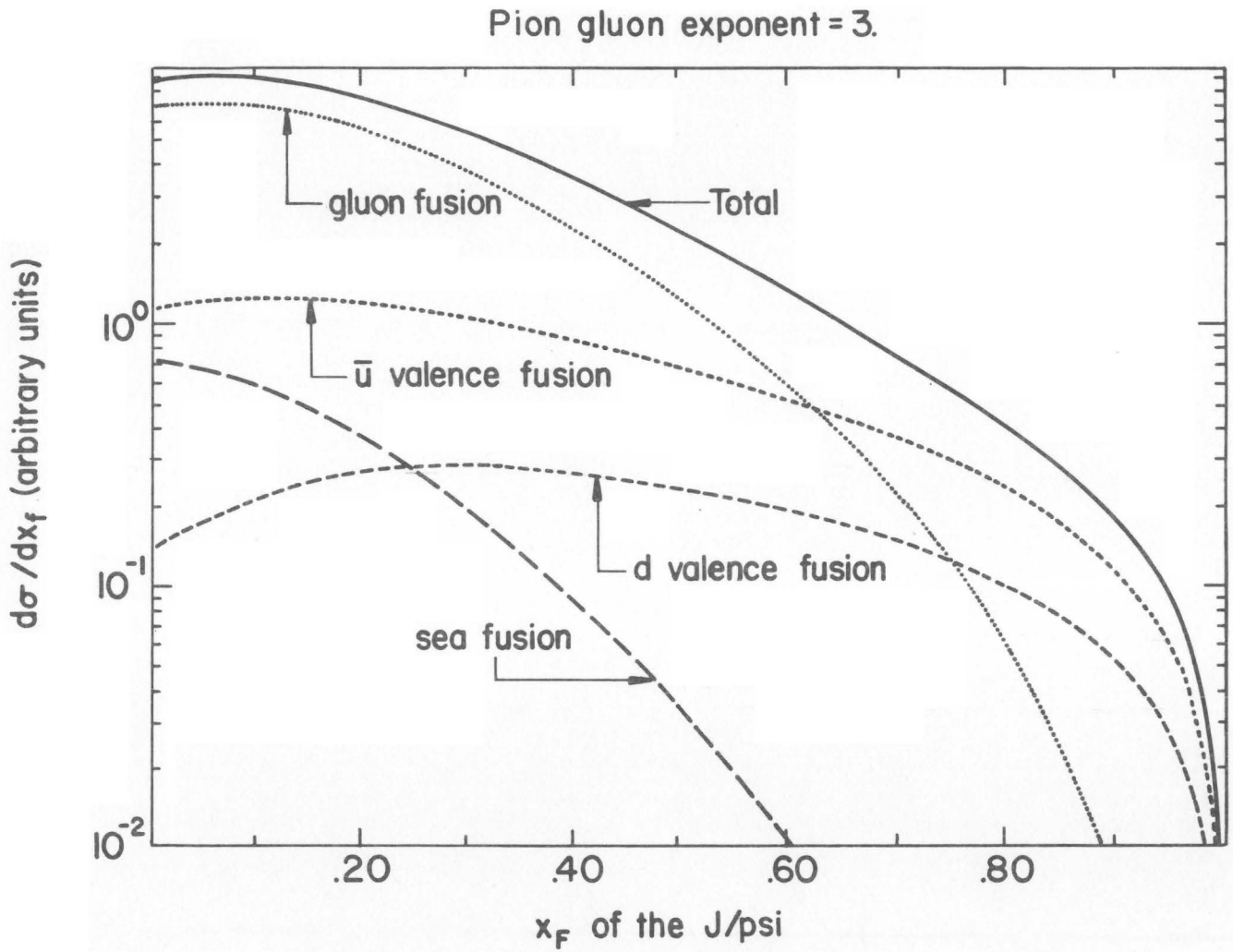

Figure 5.14
Calculation of $d\sigma/dx_F$ vs x_F for J/psi production by gluon fusion, $\bar{u}$ valence fusion, d valence fusion and sea fusion

distribution exponent. Next, the overall normalization of the curve was determined by requiring the total area of the data to be equal to the integral of the curve. Next, a chi squared was computed. The chi squared was minimized for the gluon exponent equal 2.3. This is consistent with NA3's value of 2.38. For the calculations that follow we will use NA3's gluon distribution because their distribution was based on over a million J/psis while ours is based on only about 1200 J/psis.

We used the above formulas and the raw x_F distribution to calculate the rate of quark and gluon fusion in the four bins. To do this the raw J/psi x_F distribution is binned in units of .01. The percentage of gluon, π^- $\bar{u}$ valence, π^- d valence, and π^- sea production is calculated for each x_F bin. Next the percentages of gluon, $\bar{u}$, d, and sea fusion are weighted by the number of events in the bin. Then all the bins in the interval are summed up to give the total percentages of the 4 contributions.

In order to calculate the forward charge for each bin, we assume that J/psi production via gluons and π^- sea quark gives the same forward charge as the interaction data or control region data. The forward charge for the control region data after correcting for the Drell-Yan contamination is -.59, and the forward charge for the interaction region is -.62. Hence, we take the forward charge for gluon fusion and sea fusion as -.6. We assume the difference between quark fusion and gluon fusion is -.47 as given by WA11. Hence, we assume a J/psi event produced by a $\bar{u}$ valence quark or a d valence quark will give a forward charge of -.13 and -.365, respectively. Let P_G, P_U, P_D and P_S be the percentages of gluon fusion, $\bar{u}$ fusion, d

fusion and sea fusion. Since we have assumed that only quark fusion and gluon fusion take place, we have the following condition.

$P_G + P_U + P_D + P_S = 1$

The calculated charge sum is

$< Q_{CS} > = -.6P_G - .13P_U - .365P_D - .6P_S$

This procedure was used to calculate the charge sum for the four x_F bins. The results are given in Figure 5.15(a,b,c,d). Counting rules gives n = 3 for the pion gluon distribution exponent. Because our spectrometer accepts J/psis with $x_F > 0.1$, the value of x for the proton parton which contributes to the cross section for gluon fusion and quark fusion is usually between 0.0 and 0.1. Hence, our results given in Figure 5.15 are fairly insensitive to the proton gluon distribution exponent. This calculation of the forward charge shows that as x_F increases the forward charge becomes less negative.

5.8 Failure of Drell-Yan Formalism

According to Duke and Teper [42], Drell-Yan formalism breaks down when

$M^4/(s*x_F^2) < \langle u_T^2 \rangle$

where

1. M is the mass of the dimuon

2. x_F is the Feynman x of the dimuon

3. $\langle u_T^2 \rangle$ is the square of the average transverse mass; i. e. let u be the mass of the incident quark and p_T be its transverse momentum; then $u_T^2 = u^2 + p_T^2$

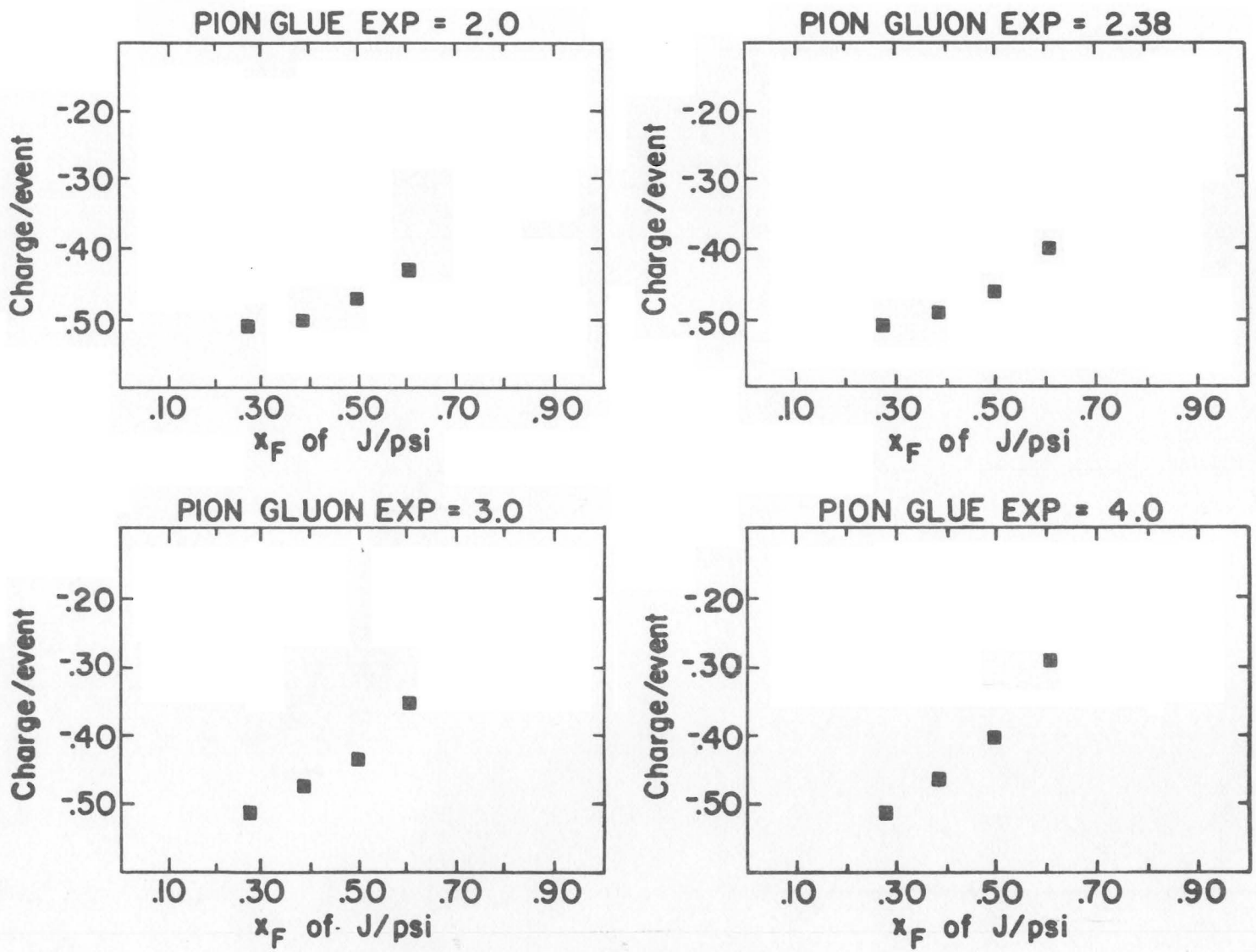

Figure 5.15
Calculation of hadron charge sum vs x_F using four different pion gluon distribution functions

The model we are using is based on the Drell-Yan formalism, as are almost all J/psi production models. Hence, the Drell-Yan formalism breaks down for E610 when

$x_F > \mathrm{sqrt}(m^4/(s*\langle u_T^2\rangle)) \sim 0.5$

where we let $\langle u_T^2\rangle \sim (1\ \mathrm{Gev})^2$

For J/psis with x_F above .5, Duke and Teper claim that the production takes place via partons within the same hadron, in our case the pion. At this point very little work has been done applying the ideas of Duke and Teper to either Drell-Yan production or J/psi production. Hence, we will no longer pursue their ideas. We only note that theoretical objections have been raised in applying the model just described to data with an x_F above 0.5.

5.9 Conclusion

The forward charge for the J/psi events becomes more negative as the x_F of the J/psi increases. This contradicts the model we have constructed. The data will contradict any Drell-Yan type model in which the forward charge is independent of the left over energy of the hadronic system. As described in the theory section, the comparison of cross section by different beam particles shows that gluon fusion plays an important role in J/psi production. The difference in forward charge between the J/psi data and the interaction and control region data shows that quark fusion must also play a role in J/psi production. Since the quark distribution function is flatter as a function of x_F than the gluon distribution function, we expect the rate of quark fusion to increase as a function of x_F of the J/psi. This fact is independent of the exact

details of $\sigma^{q\bar{q}\to c\bar{c}}$ or $\sigma^{gg\to c\bar{c}}$ which we used in our specific model. The use of the model, however, gives us an idea how much we expect the forward charge to change from our low bin to our high bin. Therefore, in any Drell-Yan type model in which the forward charge is not strongly dependent on the left over hadronic energy, we expect the forward charge to become more positive as the x_F of the J/psi increases. This is not seen in the data. As suggested by Duke and Teper, there may be something wrong with applying the Drell-Yan formalism to J/psi production at high x_F.

APPENDIX A

TRACKFINDING

In this appendix we will discuss the trackfinder which finds all tracks, not just muons. The trackfinding described in the analysis section was used to find muons. The beam reconstruction, vertex finding and upstream trackfinding were exactly the same for both trackfinders. The downstream trackfinder used to find all the tracks was basically the same as that used to find the muons except for a few changes made to enable it to find all the tracks. One change involved the predicting scheme and another change involved the procedure which tossed out bogus tracks. In this section we will describe the X and Y predicting schemes needed for the trackfinding in the CCM. We will then describe the downstream trackfinding.

The definition of the coordinate system for this section is the same as that given in the beginning of Chapter 3. The origin of the coordinate system is at the exact center of the CCM. The beam travels in the + Z direction. The + Y direction is up. Looking downstream the X direction is left. All distance units in this appendix are cm.

A.1 X Predicting Scheme

In the analysis we used all tracks in the forward hemisphere to compute the forward going charge. Since $\gamma_{CM} = 10.5$, a pion produced at rest in the center of mass system will have momentum > 1.5 Gev/c in the laboratory system. Therefore, the trackfinder should be designed to find all tracks with momenta > 1.5 Gev/c. The predicting scheme should be able to make predictions to all other planes in the

magnet using an upstream XY space track and an X coordinate in the magnet. The accuracy of the predictions should be less than 1 wire spacing, which is 0.2 cm.

The predicting scheme is based on the standard track method as described in Section 4.5. The notation we use for this appendix is same as that in Section 4.5. The trackfinder used for the second pass had only one standard track. One standard track was sufficient for finding tracks down to 6 Gev/c. The assumption of the standard track method is that the ratio of the deflection of a track at one chamber to that at another chamber is a constant. For low momentum tracks with large deflections, this assumption breaks down. This ratio is a function of the momenta and upstream slopes of the track. To enable the trackfinder to find tracks down to 1.5 Gev/c, 50 standard tracks were used. The momentum of the stored tracks was P = 50/K Gev/c where K runs from 1 to 50. These tracks were derived by using a routine which swims a particle of momentum P through the CCM by solving Maxwell's equations. The momentum of the standard track used to make a prediction for a track was close to the momentum of the track.

We will first discuss making predictions for tracks whose upstream Y slope is 0 and give an example showing how well predictions can be made. Later, we will give an example and show how the upstream Y slope can be used to make more accurate predictions for those tracks whose Y slope is large.

The swum standard tracks originated at the center of the target, had an upstream X slope (θ_X) of -.08 and an upstream Y slope (θ_Y) of 0.0, and were positively charged. The slope, $\theta_X = -.08$, was

picked to enable these swum tracks to go though as many of the UI chambers as possible for a track of a fixed momentum. Tracks accepted by our spectrometer have θ_X values which range between $\pm$ 0.1, so that the standard tracks have nearly the widest angle a track can have and still be accepted. By symmetry of the CCM field around the plane x = 0, the geometry of a positive track with $\theta_X = -.08$ is the same as the geometry of a negative track with $\theta_X = .08$. Hence, we need only concern ourselves with positive tracks.

Below is an example of how predictions can be made for tracks with momentum 3.33 Gev/c using a track with momentum 3.33 Gev/c and $\theta_X = -.08$ and $\theta_Y = 0.0$. All tracks given below originate at the center of the target, i. e. at (x,y,z) = (0.0,0.0,-741.0). The X coordinates in the UI chambers for a track P = 3.33 Gev/c and $\theta_X = -.08$ are the following:

UI1	UI2	UI3	UI4	UI5
-37.92	-39.42	-33.70	-4.72	45.06

The Z coordinates for the UI chambers are

UI1	UI2	UI3	UI4	UI5
-248.5	-180.2	-90.2	47.3	171.8

Using these numbers and Z = -741.0 for the target, we get coordinates for a track with $\theta_X = -.08$ and no deflection by the CCM as the following:

UI1	UI2	UI3	UI4	UI5
-39.40	-44.86	-52.06	-63.06	-73.03

The difference between each pair of numbers is stored as the standard track, $S_X(I)$. They are the following:

TABLE 1

UI1	UI2	UI3	UI4	UI5
1.48	5.44	18.36	58.34	118.09

We will now show how well these numbers can be used to make predictions for tracks with momentum 3.33 Gev/c and $\theta_X = -.1, -.04$ and .02. The X coordinates for a track of momentum 3.33 Gev/c and $\theta_X = -.1$ are the following:

UI1	UI2	UI3	UI4	UI5
-47.79	-50.74	-47.00	-21.28	25.09

Using the hit in UI5, Formula 4.1 in Section 4.5, and the values of the standard track differences given in Table 1, the differences between the actual coordinate and predicted coordinate in UI1 - UI4 are the following:

UI1	UI2	UI3	UI4
0.000	-.014	-.013	.064

In this case the prediction is accurate to less than one wire spacing. If the $\theta_X = -.02$, then the X coordinate for the track are the following:

UI1	UI2	UI3	UI4	UI5
-8.33	-5.61	5.88	44.43	104.42

This track will miss the active area of UI5 because the X boundaries of the UI chambers are $\pm$ 52 cm. Hence, the most downstream UI chamber with a hit is UI4. Using the hit in UI4, Formula 4.1, and Table 1, we get the differences between the actual coordinate and predicted coordinate for UI1, UI2 and UI3 as the following:

UI1	UI2	UI3
-.010	-.008	-.046

Again very small. The X coordinates of a track with $\theta_X = 0.04$ and P = 3.33 Gev/c are

UI1	UI2	UI3	UI4	UI5
-21.21	-28.02	45.01	92.82	162.57

The track will not pass through the active area of UI4 or UI5. If we use the coordinate in UI3 to make predictions in UI1 and UI2, we get the difference between the actual coordinate and predicted coordinate as the following:

UI1	UI2	UI3
-.019	-.034	.000

For tracks with higher momentum which reach UI4 and UI5 with $\theta_X = .04$, good predictions can still be made at any chamber with a track of $\theta_X = -0.08$. This is because a positive track with $\theta_X = .04$ cannot have a large deflection in any of the UI chambers it reaches since it is bending away from the center of the magnet. The largest deflection in the UI chambers a track which bends away from the center of the CCM can have is about 26 cm, the half width of the UI chambers. In conclusion, a track with momentum P, $\theta_X = -0.08$ and $\theta_Y = 0.0$ can make a good prediction for a track of momentum near P, $\theta_Y = 0.0$ and any θ_X.

For some tracks with large Y slopes the above method does not make a prediction within 0.2 cm. This is illustrated with the following example. We can use a 2 Gev/c standard track with $\theta_X = -.08$ and $\theta_Y = 0.0$ to make a prediction for a 2 Gev/c track with $\theta_X = -.08$ and θ_Y between 0.01 and 0.06. Our spectrometer accepts tracks with θ_Y between $\pm$ .06. If a hit in UI4 is used to make predictions in UI1, UI2 and UI3, then the difference between the

actual and predicted values are the following. The first column gives the upstream Y slope for the track.

θ_Y	UI1	UI2	UI3
0.01	-.002	-.004	-.006
0.02	-.012	-.029	-.029
0.03	-.042	-.093	-.087
0.04	-.084	-.184	-.167
0.05	-.143	-.318	-.291
0.06	-.216	-.490	-.455

The differences for $\theta_Y = .05$ and .06 are greater than a wire spacing. These differences can be made smaller using the following procedure. Let $X_S(I,P,\theta_X,\theta_Y)$ be the X position at chamber I for a track of momentum P, upstream X slope θ_X, and upstream Y slope θ_Y. The track is assumed to come from the X,Y point (0,0) in the center of the target. The following quantity was stored for each of the standard tracks.

$$S_{DEV}(I,K) = X_S(I,P,-.08,.06) - X_S(I,P,-.08,0.0)$$

where P = 50/K, K runs from 1 to 50.

As stated before, the quantity below was stored.

$$S_X(I,K) = X_S(I,P,-.08,0.0) - S_0(I)$$

where

1. P = 50/K

2. $S_0(I)$ is the X projection in chamber I of a straight line track which originates in the center of the target and with $\theta_X = -.08$.

For a particular upstream track with upstream slope θ_X and θ_Y the standard track used in Formula 4.1 is :

$$S_X(I) = S_X(I,K) + S_{DEV}(I,K)(\theta_Y/.06)^2 \qquad (A.1)$$

We will state later how to get K. The .06 comes from the definition of S_{DEV} which uses a track with $\theta_Y = .06$.

We will show how this formula improves our prediction for the 2 Gev/c tracks with $\theta_X = -.08$ and θ_Y between .01 and .05. For the prediction we used Formula A.1 with $S_X(I,K)$ and $S_{DEV}(I,K)$ calculated for a 2 Gev/c track. Using the above with Formula 4.1, we get the following differences between the actual coordinates and predicted coordinates.

θ_Y	UI1	UI2	UI3
0.01	.004	.009	.007
0.02	.012	.025	.022
0.03	.011	.029	.026
0.04	.011	.034	.036
0.05	.007	.022	.025

We have improved our prediction so that for this case the difference is now less than 0.05 cm. Formula 4.1 along with the above standard track gives predictions which are accurate to 0.2 cm for all tracks of momentum P = 50/K.

We will now describe how to determine K and how the X predicting scheme works. Using a point in one of the chambers and an upstream X and Y track, the predicting scheme makes predictions in all the UI chambers. To do this, first a crude value of the momentum is determined using the standard track method. This is done by the following procedure. Let $S_X(I)$ be the standard track at chamber I for some momentum P_{STK}. For the trackfinder used to analyze the data, P_{STK} was 20 Gev/c. Let $X_0(I)$ be the upstream track whose momentum we are trying to determine projected into chamber I. Let X(I) be the X coordinate of the track at chamber I. As shown in

Appendix E, an approximate momentum for the track is

$$P = P_{STK} * S_X(I)/(X(I) - X_0(I)) \qquad (A.2)$$

This initial momentum, P, is used to determine which standard track is used. A first attempt at an index for the standard track is

$$N = 50(1/P + .01)$$

The number 50(1/P + .01) is computed and truncated to an integer N. (We note that the stored tracks had momentum P = 50/K; K=1, 50.) It turns out that N may not be the correct index for very low momentum tracks. Hence, the standard track with index N along with Formula A.2 is used to compute a more accurate value of P. For this next iteration $P_{STK} = 50/N$; and $S_X(I) = S_X(I,N)$. Three iterations are done to insure the correct track is found. After the correct momentum track is found, then the upstream Y slope is used along with Formula A.1 to compute the the standard track for this particular upstream slope and point in the magnet. This track along with Formula 4.1 is used to make predictions in all the UI tilted planes.

Given an upstream track and a point in the magnet, predictions can be made to an accuracy of 0.15 cm for all chambers upstream of the predicting chamber and for all values of upstream X and Y slopes accepted by our spectrometer. This is true for all tracks with momentum down to 1 Gev/c. For chambers downstream of the predicting chamber the error sometimes exceeds 0.2 cm. Although the stored standard tracks originated from the center of target, good predictions can be made for tracks which are as far away as 10 cm from the center of the target in either X or Y. Since almost all K_S and Λ s we accept project back to within 10 cm of the interaction, the above scheme will work to find tracks associated with neutral Vs.

A.2 Vertical Focusing

The bending of the tracks in the Y direction by the CCM must be taken into account in order to make accurate Y predictions in the magnet. This bending in Y is called vertical focusing. Because the tilted planes in the magnet are tilted 11 degrees away from vertical, the Y information is necessary to compute X at any individual tilted plane. Hence, accurate Y calculations are necessary for accurate X calculations during the downstream trackfinding in the CCM. Accurate Y information is also needed to match the U hit in a chamber with the V hit in the same chamber. The formula quoted below for vertical focusing is not used for the Y straight line trackfinding in the UI chambers.

In order to take into account vertical focusing, the following formula was derived.

$$Y(I) = \theta_Y*Z(I)+Y_{INT}+Y_1*\{[A(I)/P+B(I)]*Q*X_0(I)+[C(I)/P+D(I)]\}/P$$

Where

1. Y_{INT} is the intercept of the upstream y track. Y(I) is the Y calculated position of the track at chamber I.

2. Z(I) is the Z position of UI chamber I.

3. $Y_1 = \theta_Y*Z(1) + Y_{INT}$, i.e. the Y position of the straight line track projected into UI chamber 1.

4. P is the momentum of the track, calculated using the standard track technique.

5. Q is the sign of the charge of the particle, $Q = \pm 1$.

6. $X_0(I) = \theta_X * Z(I) + X_{INT}$, the undeflected X track at chamber I (X_{INT} is the intercept of the upstream X track.)

7. A(I), B(I), C(I) and D(I) are constants which are functions of the chambers. A(I) is almost zero and could have been ignored. These constants were derived using a magnet swimmer and map.

The above formula was compared with tracks swum through a CCM magnet map. The formula was able to make correct predictions to within .05 cm for all tracks down to 1.0 Gev/c accepted by our spectrometer. The above formula works even if the track is displaced by as much as 10 cm from the beam line at the center of the target. This formula was derived using the output from a magnet map. A derivation for some of the terms in this formula is given in the thesis of S. Pordes [43].

The predicting scheme was fairly fast although not much effort was made to speed it up. The predicting scheme added about 50 ms to the trackfinding time per event.

A.3 Downstream Trackfinding

The downstream trackfinding using the low momentum predicting scheme is very similar to the second pass trackfinder described in the analysis section. First, an upstream X and Y track are paired together with no initial attempt to match them. Next, the search for seed points starts with UI5 and proceeds to UI2. Each point in one of the UV planes in the seed chamber is used as a seed point. The

seed plane is the tilted plane with the fewer number of hits in that chamber. Using this point and the upstream track parameters, an approximate value of the momentum is calculated using the standard track method. If the momentum is less than 10 Gev/c, the correct standard track is found by the scheme described in Section A.1. The momentum, upstream track parameters, and the formula for vertical focusing are used to calculate Y for the track at the seed plane. If the momentum is greater than 10 Gev/c, the one standard track for muon finding is used and the Y is calculated at the seed plane just using the upstream Y track. Using the U hit and Y information, we compute X at the plane. Using the standard track and Y information, a prediction is made in the other tilted plane in the seed chamber. If no hit is within 0.4 cm of the prediction, the trackfinder goes on to the next hit in the seed plane. If there is a hit, then both the hits in the U and V planes are used to compute X at the chamber. Using this X point and the upstream track, a prediction is made in all the other tilted planes using the standard track and for tracks with momenta below 10 Gev/c the formula for vertical focusing. Next, a search is made for the hits. If the hits are within the windows, they are saved.

At this point we will give a short discussion about the windows. Table 2 gives the windows.

TABLE 2

	SEED CHAMBER			
	UI2	UI3	UI4	UI5
UI1	0.6	0.6	0.6	0.6
UI2	---	0.6	0.6	0.6
UI3	0.8	---	0.6	0.6
UI4	2.0	1.3	---	0.6
UI5	---	2.0	0.9	---

The column gives the predicting chamber. The rows give the chamber where the prediction is made. As an example, if a hit from UI2 is used to predict a hit in UI3, then the window is 0.8 cm. Hence, the absolute difference between predicted hit and the nearest hit must be less than 0.8 cm for the hit to be saved. No prediction is made from UI2 to UI5 because the distance between them is too large. The windows were arrived at by histogramming the difference between the predicted hit in a chamber and the nearest hit using tracks with 3 points required in the drift chambers to ensure they were real.

A search for hits is made in both tilted 80 cm planes. If the momentum of the track is greater then 3.33 Gev/c, then the upstream XY track is projected into the tilted 80 cm plane. If the momentum of the track is below 3.33 Gev/c, the upstream track along with a momentum dependent correction is projected into the tilted 80 cm planes. If there is a hit within 0.3 cm of the prediction, it is saved.

After searching for the hits for a track, a check is made to be sure 2 hits in the same chamber match up. If a track has a hit in both the U and V plane of a chamber, then the U hit must project to within 0.4 cm of the V hit. If not, then only the hit nearest the prediction is saved. Next, the track efficiency is calculated. The track efficiency is the total number of tilted plane hits divided by the number of planes the track goes through. One of the planes in the tilted 80 cm chambers just upstream of the CCM did not hold high voltage very well. As described in the Section 4.5, the two 80 cm tilted planes were merged as one plane so that the total number of

tilted planes the trackfinder saw was 11 planes not 12 (two tilted 80 cm planes and ten tilted UI planes).

The requirement a track needs to satisfy before it is saved are the following.

1. It has to have at least 5 tilted hits.

2. The track efficiency has to be greater than .6.

3. The track efficiency has to be greater than .7 if any of the following conditions are true.

   a) The seed chamber is UI2 or UI3.

   b) The track has no DC hit.

   c) The track has no hit in H Hodoscope and the track projection lies > 1.5 cm inside the border of an H element.

   d) The track has no hit in the tilted 80 cm planes

4. The track efficiency has to be greater than .8 if any of the following conditions are true.

   a) The track has no drift chamber hits but went through 3 drift chamber planes.

   b) The track has no hit in H hodoscope even through it is at least 1.5 cm inside an H element and no DC hit even though it went through 2 DC planes.

If the track passes these cuts, it is saved as a possible track candidate. There is a possibility that the track could be rejected by the weeding schemes described in the next section. We note that the above conditions are fairly loose so that almost all tracks could

be found.

A.4 Weeding

One of the major trackfinding problems was bogus tracks. Making the track requirements more stringent did not solve the bogus track problem. Other methods to remove bogus tracks had to be developed. Some bogus tracks were removed during the trackfinding and some were removed later. We will now describe some of the schemes used to remove the bogus tracks.

During the trackfinding, two tracks whose upstream X slopes differ by less than 2.4 mr are compared to see if one of them is bogus. This angle criterion was arrived at by observing the difference in the upstream slopes between 2 tracks which shared a tilted hit in either UI3, UI4 or UI5. A histogram of the difference in upstream slopes showed a spike between 0 and 2.4 mr and a long tail which started at 2.4 mr. Hence, if two tracks have upstream slopes differing by less than 2.4 mr and they share a hit, then probably one of the tracks is bogus.

In order to find which one of the tracks is bogus, the total number of shared hits in the UV planes in UI3, UI4, and UI5 is summed. UI2 is included if both tracks had momentum less than 9 Gev/c. One of the tracks is rejected if one of the following conditions is true in addition to the angle criterion.

1. They share 2 or more hits.

2. They share a hit in UI4 or UI5.

3. If neither track has a hit farther downstream than UI3 and they share one or more hits.

It turns out that the trackfinding does not change very much if only condition (1) is used to weed out tracks. The better track is decided by checking, in order, the number of tilted plane hits, the efficiency and finally the chi squared. The better track is kept and the worse track is removed.

After trackfinding is completed four more routines are used to remove bogus tracks. We will only describe one of these, the last one called. If only this routine is called instead of all four of them, then the result would not change very much. This routine gives the general philosophy of weeding.

The weeding is based on the idea that a track cannot share too many of its hits with other tracks. First, for each track the total number of UI UV hits which are not shared with any track are calculated. Next, the unshared efficiency is calculated. This is the total number of unshared hits divided by the total number of planes the track goes through. A track is classified as bogus if one of the following conditions is satisified.

1. The track has less than 3 unshared hits.

2. The track has less than 4 unshared hits and either the track does not have hits in all the planes it goes through or its upstream X track or Y track are shared by another track.

3. The unshared efficiency is less than 50%.

4. The unshared efficiency is equal to 50% and either the track shares one of its upstream tracks with another track or the track has less than 2 drift chamber hits.

Next, if one or more bogus track candidates is found, then only one track is removed. The track removed is the bogus track candidate with, in order, the fewest unshared hits, the fewest total tilted plane hits, the lowest regular track efficiency and the highest chi squared. If none or one bogus track candidates are found, the weeding stops. If more than one bogus track candidates are found, then the process starts over again with a new calculation of the number of unshared hits for a track. The process stops when one or zero bogus track candidates is found.

The algorithm for the other routines which weed is similar to this one. A downstream track must have enough independent quantities such as hits, upstream track and DC points so that the track looks real.

To help determine the weeding scheme, every event in the J/psi sample with a multiplicity greater than 7 or charge difference greater than 2 or less than -2 was scanned visually on graphics. This is approximately 400 events. A sample of 150 events with multipicity less than or equal 7 was also scanned. We conclude after visually scanning these tracks that bogus tracks were not a problem.

A.5 Track Fitting

All the tracks found using the procedure above, with 2 exceptions given in Section 5.3, were used to calculate the forward charge. It is possible the windows may have been too wide so that enough bogus tracks were found to bias our results. In this section we will discuss imposing tighter geometric requirements on the tracks by fitting them and recomputing the physics results to see if they are sensitive to the windows.

In order to impose tighter geometric cuts, we first fit the tracks using the procedure described in Section 4.6. The vertex, the 80 cm chambers and the UI chambers were used to fit the tracks. This procedure enabled accurate calculation of the momenta and upstream track parameters. Next, predictions were made in all the chambers by swimming the track with a magnet swimmer and magnet map. We then researched for all the points for the track with narrower windows. The windows were 0.2 cm for the 80 cm chambers and 0.3 cm for the UI Y planes. For the UI tilted planes we did this procedure with windows of both 0.3 cm and 0.4 cm. The windows for the drift chambers were 1.0 cm. If the hits were within the windows, the hits were saved. As was done in the trackfinding, the U hit of one plane was required to match with the V hit of the other plane in the chamber for both hits to be saved. Next, the track requirements stated in Section A.3 were imposed. The tracks which satisfied the track requirements were used to calculate the forward charge associated with the J/psi events. This determined how sensitive our result was to the trackfinding windows.

The table below gives the difference between the forward charge

using the above fitting procedure and the forward charge without the fitting procedure. The first column tells the size of the window in the UI tilted planes. The second column gives the difference for the J/psi data averaged over x_F while the next four columns gives the difference for the 4 bins defined in Table 1 of Chapter 5. The table below gives these differences for both charge sum and charge measure.

TABLE 3

FITTED FORWARD CHARGE MINUS UNFITTED FORWARD CHARGE

WINDOW	AVE	BIN 1	BIN 2	BIN 3	BIN 4
CHARGE SUM					
.3 cm	.017	.016	.009	.041	.009
.4 cm	.013	.007	.009	.033	.014
CHARGE MEASURE					
.3 cm	.012	.013	.001	.046	.004
.4 cm	.011	.010	.000	.038	.004

These changes are smaller than the statistical errors which we give below.

TABLE 4

STATISTICAL ERRORS ON THE FORWARD CHARGES

	AVE	BIN 1	BIN 2	BIN 3	BIN 4
CHARGE SUM	.037	.072	.064	.081	.084
CHARGE MEASURE	.027	.051	.048	.063	.062

In conclusion, fitting the tracks and using narrower windows does not change our physics result.

APPENDIX B

TRACKFINDING EFFICIENCY

The trackfinding efficiency was measured by determining the percentage of Y tracks with hits in the UI chambers which are matched up with an X track. This is done by first finding all Y tracks which have hits in the UI chambers. After downstream trackfinding is finished, we find which of these upstream Y tracks were not matched to a downstream track. The non matching could be caused either by the upstream X track not being found or a failure in the downstream trackfinder to find the track associated with this Y track. An estimation of the trackfinding efficiency will be the total number of Y tracks with a downstream match divided by the total number of Y tracks. The precise cuts on the Y tracks will be described later.

Since the physics in this thesis uses only vertex associated tracks, we are only interested in the efficiency for finding vertex associated tracks. Nonvertex associated tracks can come from halo muons or K_S or Λ s. We are not interested in the trackfinding inefficiency due to the failure to find nonvertex associated upstream X tracks. There is no definitive way of telling if a Y track came from a track which was not vertex associated. It is possible a Y track could just happen to point to the Y vertex while its upstream X partner does not. Hence, some work is done to find these nonvertex associated upstream X tracks.

Vertex and nonvertex associated tracks are found by first calling the trackfinder which uses the angle method. This is our regular upstream trackfinder used for the data analysis. The hits associated with the found track are removed from the hit buffer.

Next, two straight line trackfinders which use the road method are called on the remaining points. The road method does not require the tracks to come from the vertex to be found. These trackfinders only find tracks in the 80 cm chambers. The Y parameters of the found tracks are projected into the UI chambers to find hits in the Y UI planes. The first trackfinder which uses the road method requires the track to have hits in all four 80 cm X or Y planes. This four point road trackfinder is the same trackfinder which was used to find the primary vertex as described in the analysis section. Next, all hits associated with found 4 point tracks are removed from the hit buffer. Next, a track finder which requires the tracks to have 3 points in the 80 cm chambers is called. This trackfinder is very similar to the preceding one called. This finishes the upstream trackfinding.

This procedure does not do a very good job finding nonvertex associated muons. The high density of tracks in the central region means that many of the hits associated with halo muons get used for both real and bogus vertex associated tracks. These hits are removed from the track buffer and non vertex associated X tracks are not found, especially in the central region. This problem was solved in 2 ways. The first way was to put cuts on the Y tracks as described below. The second way is the following. If an unmatched Y track was found, then the upstream X track buffer was cleared. Next, the upstream X trackfinding was repeated with only the road method trackfinders called. Next, the downsteam trackfinder was called. If the Y track was still unmatched, then we assumed that it was unmatched because of trackfinding inefficiency.

The above procedure of calling just the road trackfinders does not find all the nonvertex associated tracks. These road trackfinders remove points from the hit buffer during the trackfinding. Sometimes the hits associated with halo tracks get used for other tracks. Hence, some halo tracks were still not found. No more work was done to find them.

The set of Y tracks used to find the trackfinding efficiency must satisfy the following conditions.

1. The track must point to within .6 cm from the primary vertex.

2. There must be no track with an intercept as close as 2.5 mm to this track. Any track whose intercept is as close as 2 cm to this track must not be matched to 2 or more upstream X tracks. This cut eliminates those Y tracks whose downstream link was found, but was not linked up with this Y track.

3. The tracks must have greater than or equal to 3 hits in the 80 cm chambers.

4. The track must have a hit at least as far downstream as UI3.

5. If the most downstream hit is in UI3, then the track must have hits in UI1 and UI2.

6. If the most downsteam hit is UI4 or 5, then the track can miss at most one hit in the UI chambers upstream of UI4 or 5, respectively.

The above set of Y tracks was divided into 3 classes according

to its most downstream hit in the UI chambers. In the table below we list the efficiency for those Y tracks whose most downstream hit was in UI3, UI4 or UI5. We combine the tracks for UI4 and UI5 together and give a total efficiency. This efficiency was done on 3 types of events: selected dimuons with mass greater than 2.4 Gev/c^2, events from a data run near the end of the experiment, and events from an interaction trigger. The dimuons with mass greater than 2.4 Gev/c^2 included the J/psi events. The greater than 2.4 Gev/c^2 dimuons automatically required 2 of the Y tracks to be matched up. This has a tendency of pushing the trackfinding efficiency up. No such requirements are on the regular dimuon data run events or the interaction events. The column header in the table below gives the UI chamber with the most downstream Y hit.

DIMUONS WITH MASS GREATER THAN 2.4 GEV/C^2

	UI3	UI4	UI5	UI4,5	TOTAL
MATCHED TRACKS	3219	6027	18,572	24,599	27,818
TOTAL TRACKS	3759	6332	19,031	25,363	29,122
EFFICIENCY	85.6%	95.2%	97.6%	97.0%	95.5%

REGULAR DIMUON RUN

	UI3	UI4	UI5	UI4,5	TOTAL
MATCHED TRACKS	2708	4306	14,561	18,867	21,575
TOTAL TRACKS	3189	4674	15,454	20,128	23,317
EFFICIENCY	84.9%	92.1%	94.2%	93.7%	92.5%

INTERACTION RUN

	UI3	UI4	UI5	UI4,5	TOTAL
MATCHED TRACKS	4169	6150	20,915	27,065	31,234
TOTAL TRACKS	4813	6446	21,388	27,834	32,647
EFFICIENCY	86.6%	95.4%	97.8%	97.2%	95.7%

In order to check how much of the inefficiency was due to halo

muons with the upstream X track not found, we tried requiring the absolute value of the Y slope to be greater than 5 mr. Since almost all halo muons are parallel to the beam line, this cut would eliminate almost all Y tracks which link to a halo muon. This cut raises the trackfinding efficiency by about .5%. Changing the number of required hits in the 80 cm chambers from 3 hits to 4 hits raises the measured trackfinding efficiencies about 0.3%. Hence, the systematic error associated with the above efficiencies is about 1%.

Some of the inefficiencies in the UI3 bin may be due to chamber inefficiencies coupled with the tracks not going through the active UV regions of the chambers. Some of these tracks may go into the nontriplet regions of UI3. The triplet region of UI3 comprises about 80% of the area of the chamber. If the track goes into the nontriplet region of UI3, then the track must be found by a matched hit in UI2. At this point the chamber inefficiencies in UI1 and UI2 may be hurting trackfinding, rather than the actual algorithm inefficiency.

The above numbers are the efficiency for finding the upstream X track times the efficiency for matching the X and Y track to form the downstream track. The true efficiency must be found by multiplying this above number times the efficiency for finding the Y track. By looking at the Y trackfinding by graphics, we estimate the Y trackfinding efficiency at least 99% for those tracks which come from the primary vertex. We estimate the trackfinding efficiency to be 95% or higher.

APPENDIX C

MONTE CARLO PROGRAM

The efficiency for finding a track of a particular charge, rapidity and transverse momentum has been determined by Monte Carlo methods. The evaluation was necessary to show that the efficiency for finding positive particles was the same as that for finding negative particles. The program simulates the trackfinding using the real chamber boundaries and measured efficiencies for the planes instead of searching for imbedded real data tracks.

The Monte Carlo program began by dividing the 2-dimensional rapidity, transverse momentum space into a 2-dimensional grid. Each grid element consisted of rapidity between y(i) and y(i) + .025 and transverse momentum between $p_T(j)$ and $p_T(j)$ + .05 Gev/c. There were two of these 2-dimensional grids, one for positive and one for negative tracks. In order to determine the intervals of p_T and Y for which the acceptance should be calculated, we have histogrammed the rapidity (Figure C.1) and p_T (Figure C.2) of the hadrons associated with the J/psi. (There is no acceptance correction). We have calculated the acceptance in rapidity frame between -0.6 and 4.9 in the CM frame and in p_T between 0 Gev/c and 2.5 Gev/c.

One number was determined for the efficiency of finding a track with its rapidity, p_T, and charge Q in a grid element. To determine the track efficiency in a grid element, we integrated over the rapidity and p_T of the grid element, and over the azimuthal orientation and the vertex position of the track. To do this, we randomly picked value of rapidity and transverse momentum in the grid. Next, we randomly picked a ϕ and a point in the target where

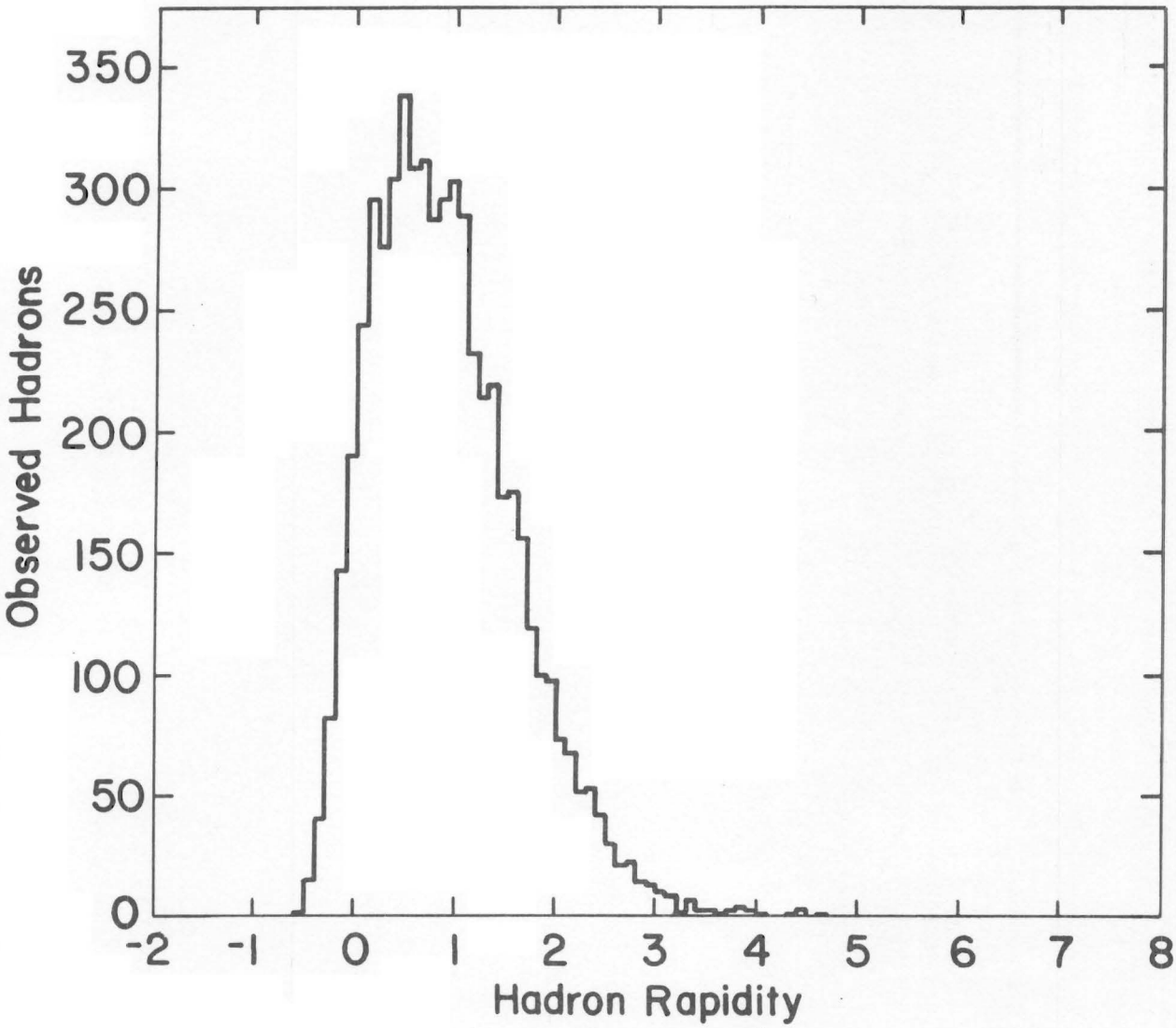

Figure C.1
Rapidity of hadrons associated with the J/psi
no acceptance correction

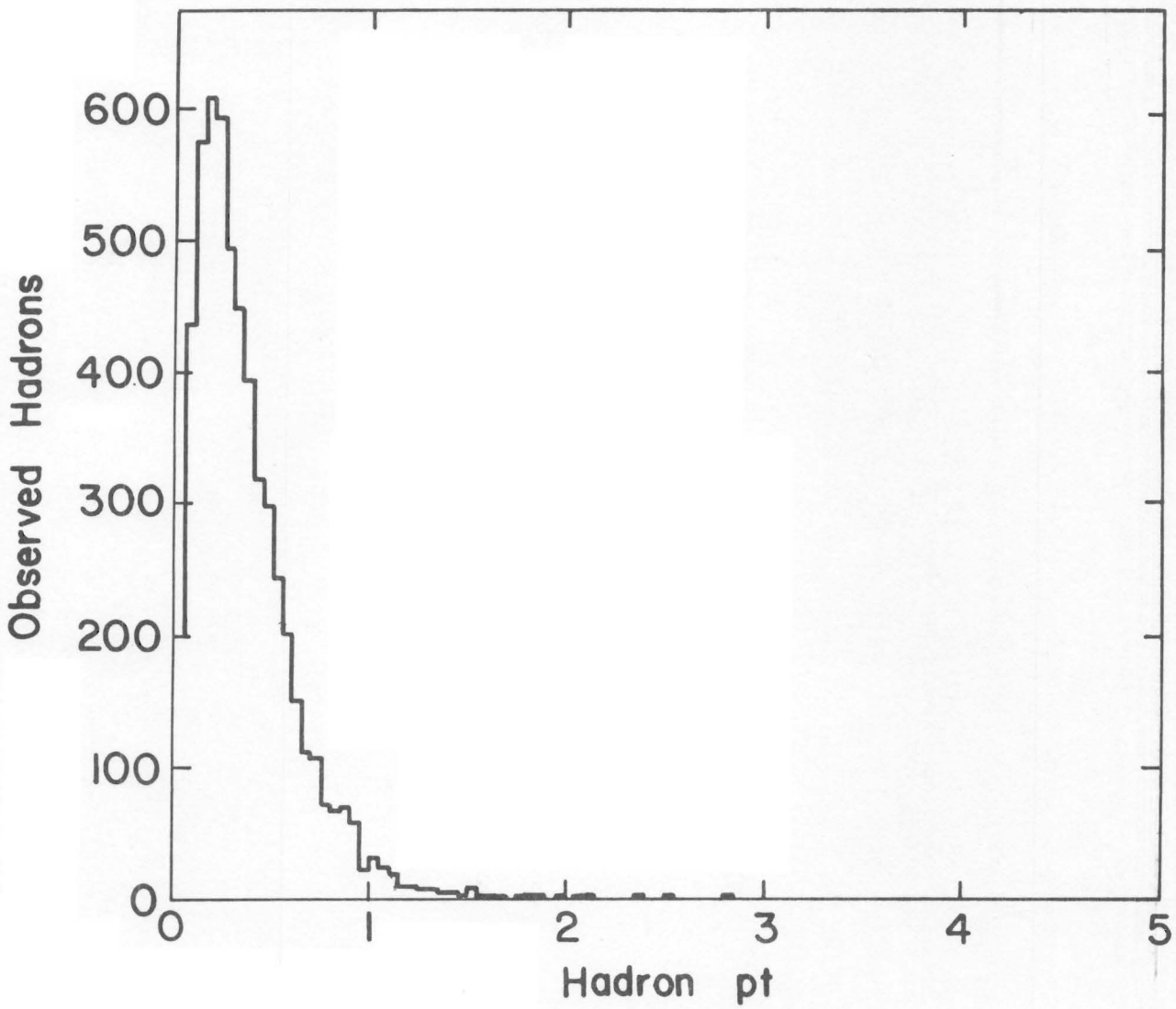

Figure C.2
Transverse Momentum of hadrons associated
with the J/psi no acceptance correction

the track came from. The region from which the Monte Carloed vertex was taken was determined by histogramming the vertex for a regular data run. This region comprises nearly all of the incoming beam. The above information determines a track with definite upstream track slope and intercept, momentum, and charge. Next, we simulate the trackfinding to determine whether this track would have been found. This is done by first determining which planes the track goes though. In the CCM and drift chambers, this is done by using a standard hard edge model of the CCM magnetic field. We randomly give the track a hit or miss in the planes it goes through using the calculated efficiencies of the planes. As stated in Appendix D on chamber efficiencies, the efficiency of a plane is a function of the position of the hit in the plane. The efficiencies of all the MWPC were lower in the region the beam went through. The efficiencies of the central beam wires away from the central beam region (Region 2) were lower for the UI chambers, but not for the 80 cm chambers. In this way we simulated the track as a set of hits in the MWPC and drift chambers. Next, using the algorithms in the trackfinder, we determined whether this track would have been found. For instance, if the simulated track had no matched hit in UI2, UI3, UI4 or UI5, it would not have been found. A track needs a matched hit in at least one of these chambers to be found. We followed about 2000 tracks for each grid element this way. This gives the trackfinding efficiency for a track with a pair of rapidity and transverse momentum values in the grid.

Figures 5.4 and 5.5 in Chapter 5 show the results of the program in the region of rapidity where the acceptance is rapidly changing. Sections 5.3 and 5.4 discuss the results of the Monte Carlo program.

This method for determining trackfinding efficiency assumes that all tracks with enough chamber information to be found, will be found. This is not quite correct, as the section on trackfinding efficiencies shows. The Monte Carlo program shows that the probability of finding a track which goes through all 5 U of I chambers is about 99%. The probability for a Y track which goes all the way though the UI chambers to be matched up is about 95%. Hence, this method does not give quite the correct absolute trackfinding efficiency, but is about 4% high.

The basic purpose of the Monte Carlo is to give a geometric acceptance and determine if there is a charge bias in our apparatus. The charge bias would be a difference in acceptance between positive and negative particles. This can arise from the lowered efficiency of the chambers in the beam region. Since the beam is negative, there could be a better acceptance for positive particles than negative particles. The Monte Carlo shows there is no charge bias. The acceptance for positive particles and negative particles is about the same.

APPENDIX D

CHAMBER AND H HODOSCOPE EFFICIENCY

This appendix concerns the efficiency measurement for the multiwire proportional chambers, the drift chambers, and the H Hodoscope. The MWPC planes were divided into three areas to determine the loss of efficiency due to the beam. The drift chambers had deadeners in the beam region, and the H Hodoscope had a gap for the beam.

D.1 MWPC Efficiencies

The principal objective was to choose a set of tracks that really penetrated all the proportional chambers without biasing the result. This selected reservoir of tracks was taken from the five tapes containing some 52,000 events including all dimuons with mass greater than 2.0 Gev/c^2. It had the advantage of testing the performance throughout the whole experiment. The efficiency measurement was also carried out on four individual runs distributed throughout the experimental period. The data from the beginning of the experiment indicated efficiencies smaller by 2-3%, but the remaining three all agreed with the average efficiencies.

The trackfinding method described in Sections 4.4 and 4.5 was used, but Drift Chamber 3 was used as a seed plane instead of the UI chambers. The X and Y projections of the upstream tracks from the vertex were found as before. If the Y projection of the upstream track extrapolated to within 4.5 cm of a hit in DC3, then this drift chamber point was used with the upstream information to predict hits in all the other planes. A requirement imposed here to assure real

tracks was that DC1 and DC2 must have X hits within 0.6 cm of the predicted points, and the hits in DC1, DC2 and DC3 must form a reasonably straight line. Two or more tracks sharing a single hit in a drift chamber were rejected to avoid double counting. In addition to these requirements, examination showed that a minimum of six hits in the UI tilted planes assured a real track. About 25,000 tracks met these criteria.

The procedure for finding the efficiency of a plane was the following. First, the total number of hits in the track was added up with the plane being looked at excluded. If this number of hits was high enough so that the track would be found, then the track was used to find the efficiency of that plane. Predictions were made in the 80 cm planes and UI Y planes using these tracks by straight line fitting. The upstream X and Y tracks and the DC1 point were used to make predictions in the tilted UI UV planes using the standard track technique. Next, the hit nearest the prediction in the plane was found. If the hit nearest the track was within the window, then the plane had a hit for that track. The window was ± 2 wire spacings for the 80 cm planes and Y UI planes and ± 3.5 wire spacings for the UV UI planes. The width of the window was wider for the UV plane because the predicting scheme for the UV planes does not use a fit to the track which was used in the straight line case. Some of the hits within this window were not associated with this track, but with other tracks or light ups. In order to take this into account, a control region about 2 cm away from the prediction was defined. This control region had the same total width as the window, i. e. 7 wire spacings for the UV planes and 4 wire spacings for the 80 cm planes

and Y UI planes. If the hit was not in the window, we tested to see if it was in the control region. The total number of times a hit lay in the control region should be nearly equal to the total number of times a hit not associated with a track lay in the window. The efficiency of a plane is the total number of hits in the track window minus the number of hits in the control region divided by the total number of tracks used for that plane. The subtraction of the control region lowered the calculated efficiencies by about 1% for the tilted UI planes and about .4% for the other planes.

To measure the chamber efficiencies in the beam region, we used data from two runs made immediately after the measurement of the beam profile. Events in these runs were triggered simply by a "clean beam" particle. The spectrometer magnet was on, so the beam profile in each plane as it was during the experiment was clearly delineated.

The UI planes were divided up into 3 regions with separate efficiencies calculated for each region (see Figure D.1). Region 1 consisted of the actual beam area. Upstream of the CCM this area was -1.8 cm $< X <$ 4.2 cm and -3.0 cm $< Y <$ 2.0 cm. This area included about 80% of the incoming beam. This region moves about 2 cm in the X direction by the time the track reaches UI5. It does not move in Y. Although the beam had a gaussian shape, we assumed a constant efficiency of the plane in the rectangular area. The efficiency of the beam region was studied in 1 cm slices, and the assumption the efficiency is constant in the rectangular area appears to be valid. The second region was defined by the wires in the beam region excluding Region 1. Region 3 was the rest of the plane. The efficiency increased monotonically from Region 1 to Region 3. The

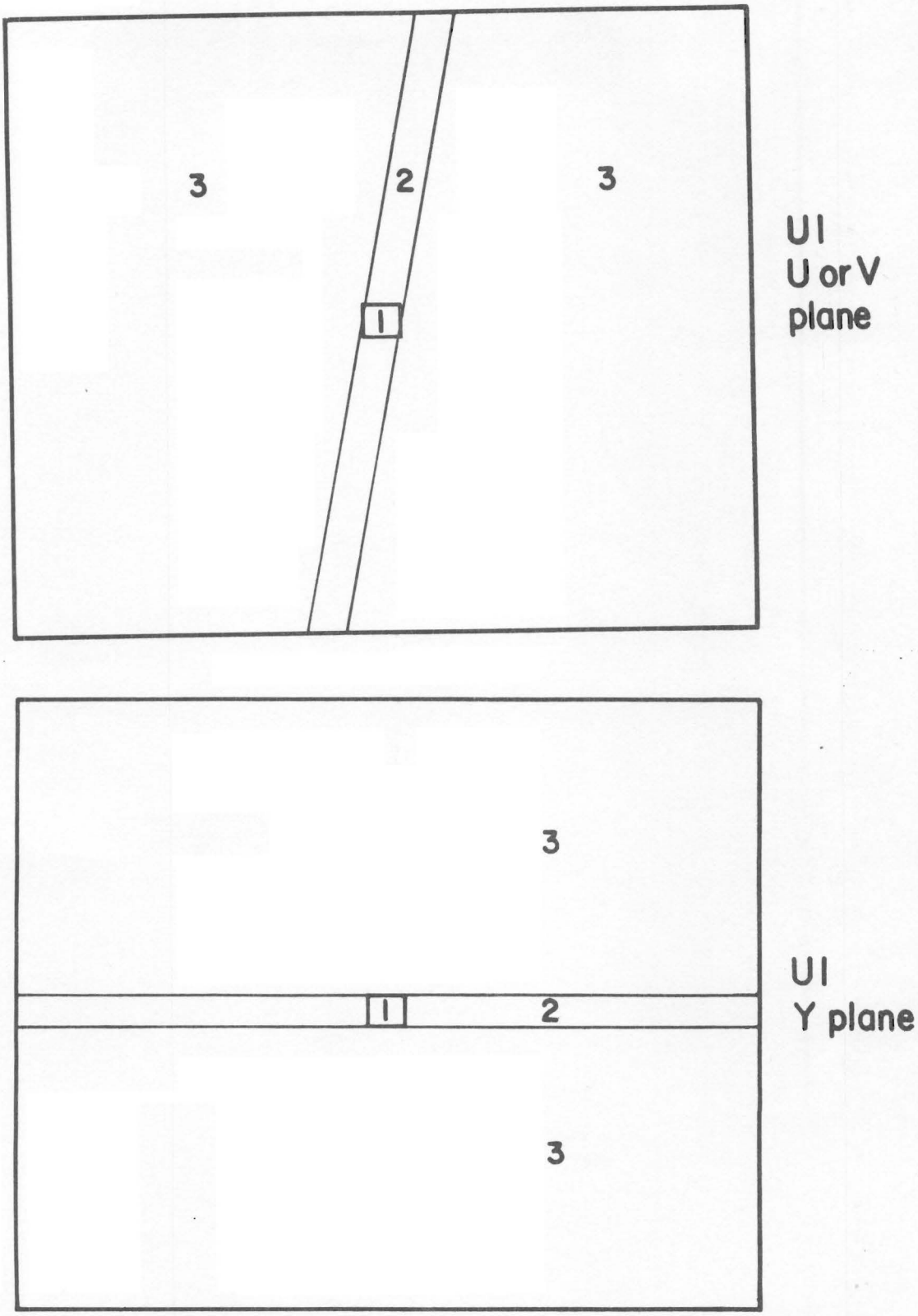

Figure D.1
The three regions in the UI chambers of different efficiency

drop of efficiency in Region 1 was probably due to a high concentration of electrons near the anode. The drop of efficiency in Region 2 was probably due to electronics which were not able to handle the high rate.

The 80 cm chambers also lost efficiency in Region 1 (see Figure D.2). They, however, appeared to have no loss of efficiency in Region 2. The electronics appeared able to handle the high rate in the beam region. The loss of efficiency in Region 2 for Plane 15, an 80 cm plane, was due to dead wires.

Table D.1 gives the measured efficiencies of the MWPC planes in the 3 regions. As stated before, Region 2 and 3 were merged into Region 3 for the 80 cm planes.

D.2 Drift chamber efficiency

The tracks used to measure the efficiency of the drift chambers were generated in a similar manner to those used to measure the MWPC efficiency. First the upstream trackfinding was done to find all straight line tracks. Next, points in DC1, DC2 and DC3 were used as seed points to find tracks. Drift chamber Y information was not required for a seed point, but if it existed it had to agree with the upstream track projected into the drift chamber to within 7.5 cm. Using the upstream track and seed point in the DC, the trackfinder made predictions in the tilted MWPC planes and the other 2 drift chambers. Hits in the other 2 drift chambers were not required, but all 10 tilted UI planes had to have a hit. A subset of these tracks was used to find the efficiency of the drift chambers.

To find the X efficiency of DC1, a track was tested to determine

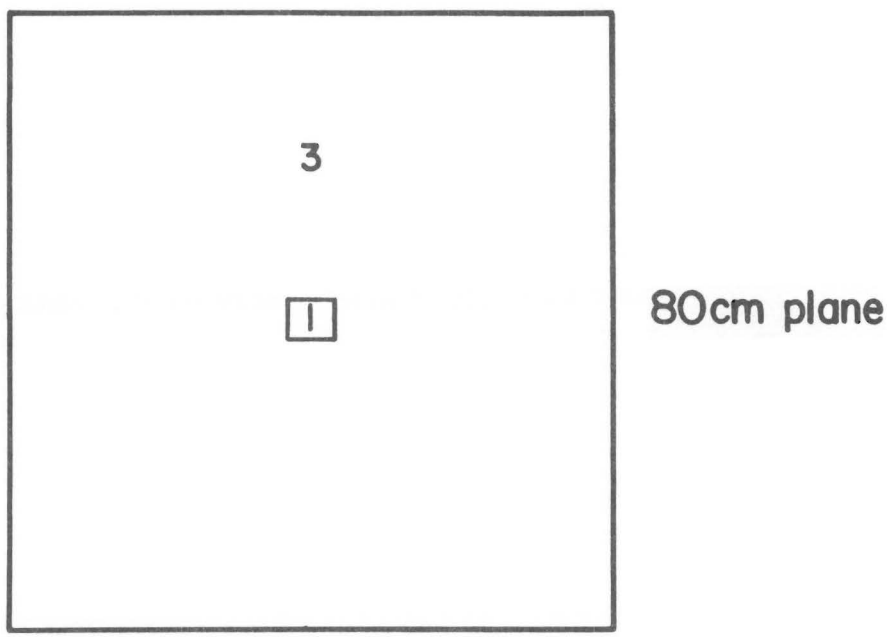

Figure D.2
The two regions in the 80 cm planes of different efficiency

if it had a hit in DC2 and DC3. If it did, then using the X point in DC2 and DC3 a straight line projection was made into DC1. A hit was searched for within 0.75 cm of the prediction. A control region 2 cm away from the prediction was defined. This control region served the same purpose in finding the efficiency of the drift chambers as it did in finding the efficiency of the MWPCs. To get the efficiency of DC2, an almost identical procedure was used. The only difference was hits were required in DC1 and DC3, while the prediction in DC2 was made by making a straight line projection of hits in DC1 and DC3 into DC2. To determine the efficiency of DC3, a slightly different procedure was used. A straight line using a point in DC1 and DC2 projected into DC3 did not make a very good prediction because DC1 and DC2 were so close together, but some distance from DC3. Instead the upstream track and DC2 point were used to make a prediction in DC3 using the standard track technique. Whether the track had a hit in DC1 or not did not affect the calculated efficiency of DC3. In this case the hit had to lie within 1.5 cm of the predicted value. Again a control region was defined to take care of accidentials. Because of our poorer method of making predictions into DC3, the systematic error in the measured efficiency for DC3 may be larger than that for DC1 and DC2.

The efficiency of the Y readout was determined at the same time as the X efficiency of the drift chambers. As stated before, to determine the X efficiency of the drift chambers, an X projection was made in the drift chambers. If a hit was within the window, then we determined whether this hit had Y information or not. The percentage of these X hits with Y information is given in Table 1 under the

column with the heading "no ydif cut". To get the efficiency of the Y readout, we required the Y hit to be within 7.5 cm of the straight line Y prediction.

As was stated in the apparatus section, the Y readout depended on magnetic cores. However, DC1 and DC2 were very close to the CCM and hence in its fringe fields. DC1´s magnetic cores were completely saturated. For that reason the Y information for DC1 was not even unpacked from the raw data. For DC2 the efficiency of the Y was reduced by a factor of 2.

We did not try to determine whether various parts of the drift chambers were less efficient than other parts. The drift chambers had beam deadeners in the beam region. There were 3 support wires. For the Monte Carlo evaluation the location of the beam deadeners and support wires were determined. Their effect was put into the Monte Carlo program by giving their region a 0% efficiency.

The DC efficiency was studied with a tape which consisted of about 5,000 tracks from about 10,000 dimuon events with mass greater than 2.2 Gev/c^2. Again this number gives an average performance of the drift chambers thoughout the run.

D.3 Efficiency of H Hodoscope

The tracks which were found to determine the efficiency of the MWPCs were also used to determine the efficiency of H. We required the tracks to have 8 hits in the tilted UI planes and 3 DC hits. If a prediction in H lay > 3 cm inside the border of an H element, then the counter was tested for a hit. The data used to find the efficiency of H came from the 5 tapes created in the second pass

which had dimuons with masses greater than 2 Gev/c^2. A total of about 17,000 tracks were used to find the efficiency of H. H did not have a hit for 9 of these tracks giving a total efficiency of H as 99.94%. Again the efficiency was the efficiency over the entire data run.

which had dimuons with masses greater than 2 Gev/c^2. A total of about 17,000 tracks were used to find the efficiency of H. H did not have a hit for 9 of these tracks giving a total efficiency of H as 99.94%. Again the efficiency was the efficiency over the entire data run.

TABLE D.1

MWPC Efficiencies

PLANE		REGION 1	REGION 2	REGION 3
7	80 cm Y	89.9		97.7
8	80 cm X	88.8		96.7
9	80 cm Y	90.0		98.5
10	80 cm X	90.0		97.1
11	80 cm Y	83.4		93.1
12	80 cm X	89.8		97.5
13	80 cm Y	86.4		97.6
14	80 cm X	88.3		98.1
15	80 cm V	47.0	60.4	72.3
16	80 cm U	94.8	96.5	96.5
17	UI1 U	82.6	87.8	91.1
18	UI1 Y	78.7	88.1	91.5
19	UI1 V	85.4	91.6	94.4
20	UI2 U	77.4	85.3	93.3
21	UI2 Y	82.8	87.3	93.2
22	UI2 V	82.7	88.1	93.0
23	UI3 U	83.4	89.7	90.0
24	UI3 Y	87.5	91.5	94.2
25	UI3 V	80.3	87.7	93.4
26	UI4 U	89.4	91.1	95.1
27	UI4 Y	89.8	89.5	94.4
28	UI4 V	85.9	90.9	94.7
29	UI5 U	77.0	88.8	91.1
30	UI5 Y	88.0	86.1	90.3
31	UI5 V	85.0	88.8	93.0

Drift Chambers Efficiencies

DC PLANE	ANODE	DELAY LINE NO YDIF CUT	DELAY LINE ABS(YDIF)<7.5
1	78.9		
2	80.8	22.9	21.0
3	75.1	68.9	63.8

APPENDIX E

STANDARD TRACK TECHNIQUE

In this appendix we will illustrate why the standard track method works for making track predictions. Figure E.1 illustrates a track being bent by the CCM. The circle represents the hard edge field. The small arc represents the track. The field of the CCM is assumed to be a hard edge so that the track arc is circular with radius r. X is normal to the incoming track and Z is in the direction of the incoming track. In this plot and only in this plot, z = 0 is at the edge of the hard edge circle. (The origin of our coordinate system is at the center of the CCM.)

The upstream slope and intercept for this track is 0. It passes through the points (x_1,z_1) and (x_2,z_2). We have

$$(r - x_1)^2 + z_1^{\ 2} = r^2$$

or

$$x_1^{\ 2} - 2x_1 r + z_1^{\ 2} = 0$$

Since $x_1^{\ 2} << z_1^{\ 2}$, this leads to the familiar sagitta relation.

$$x_1 = z_1^{\ 2}/2r = bpz_1^{\ 2}$$

where b is some constant and p is the momentum of the track. Therefore

$$(x_2/x_1) = (z_2/z_1)^2 = c$$

which is independent of r or the momentum of the track. The above statement shows the ratio of the deflection of a track at one chamber to that at another chamber is a constant, c. To find c, we do not use the formula $c = (z_2/z_1)^2$ because the CCM is not a perfect hard edge field. For the second pass trackfinder, c was evaluated by using tracks found in our data. For the full trackfinder, c was

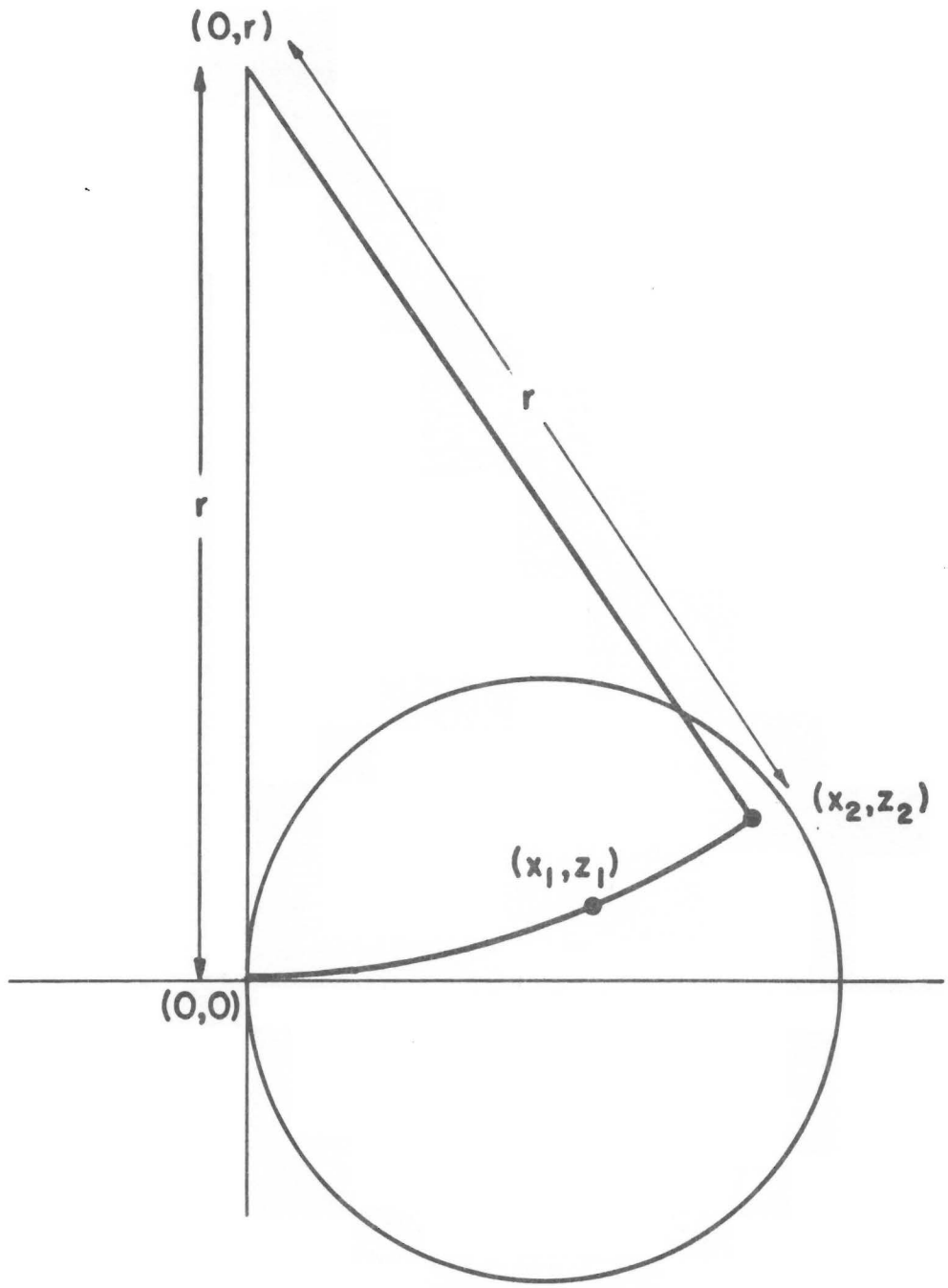

r is the radius of curvature of the particle track for a hard edge field

Figure E.1
Track bent by the CCM field

evaluated using a magnet swimmer and magnet map.

Equation 1 can be written in the form $p = d*x_1$ where p is the momentum and d is a constant determined from a magnet swimmer and magnet map. Although this formula does not give a precise calculation of the momentum of a track, it was used for two purposes. During the trackfinding for the second pass, this formula was used along with the seed point and upstream track to calculate a momentum. If this momentum was less than 6 Gev/c, then the seed point was not used to find a downstream track. This formula was also used to help find the correct standard track during the low momentum trackfinding.

APPENDIX F

UNIVERSITY OF ILLINOIS MULTIWIRE PROPORTIONAL CHAMBERS

In this section we will discuss the UI MWPCs in more detail than given in the equipment section. We will also discuss some aspects of building the chambers and their operations. We will not discuss the chamber electronics. Six chambers were built, five for the experiment and one spare.

Ulrich Kruse was in charge of building these chambers. Robert Downing designed the chambers. Vaidas Simaitis designed the prestressing. The workers included Howard Budd, John Cooper, Sandra Cooper, Tom Graff, Patrick Lukens, Harold Scott, and Keith Thorne.

F.1 Description of the Frames and Wire Planes

Figure F.1 is a cross section view of the upper part of the chambers in the plane X = 0. The figure illustrates the order of the wire planes and the frames which hold the wires. Figure F.2 is a view of a chamber looking downstream. None of the support pieces which keep the chamber upright and hold the electronics are shown. The frames for the cathode and the anode planes were 1/4 inch G-10 with no more than 3 mils of variation in thickness at any point. The outer dimensions of the frames were 60 in by 48 in. The inner dimensions were 50 in by 38 in. Two holes, one at the top left and the other at the top right, were precision drilled and surveyed relative to the wires. The pins which went through these holes were used to survey the chambers for the experiment.

The anode planes consisted of 0.8 mil gold plated tungsten wire with a wire tension of 40 gm. The breaking point of this wire is

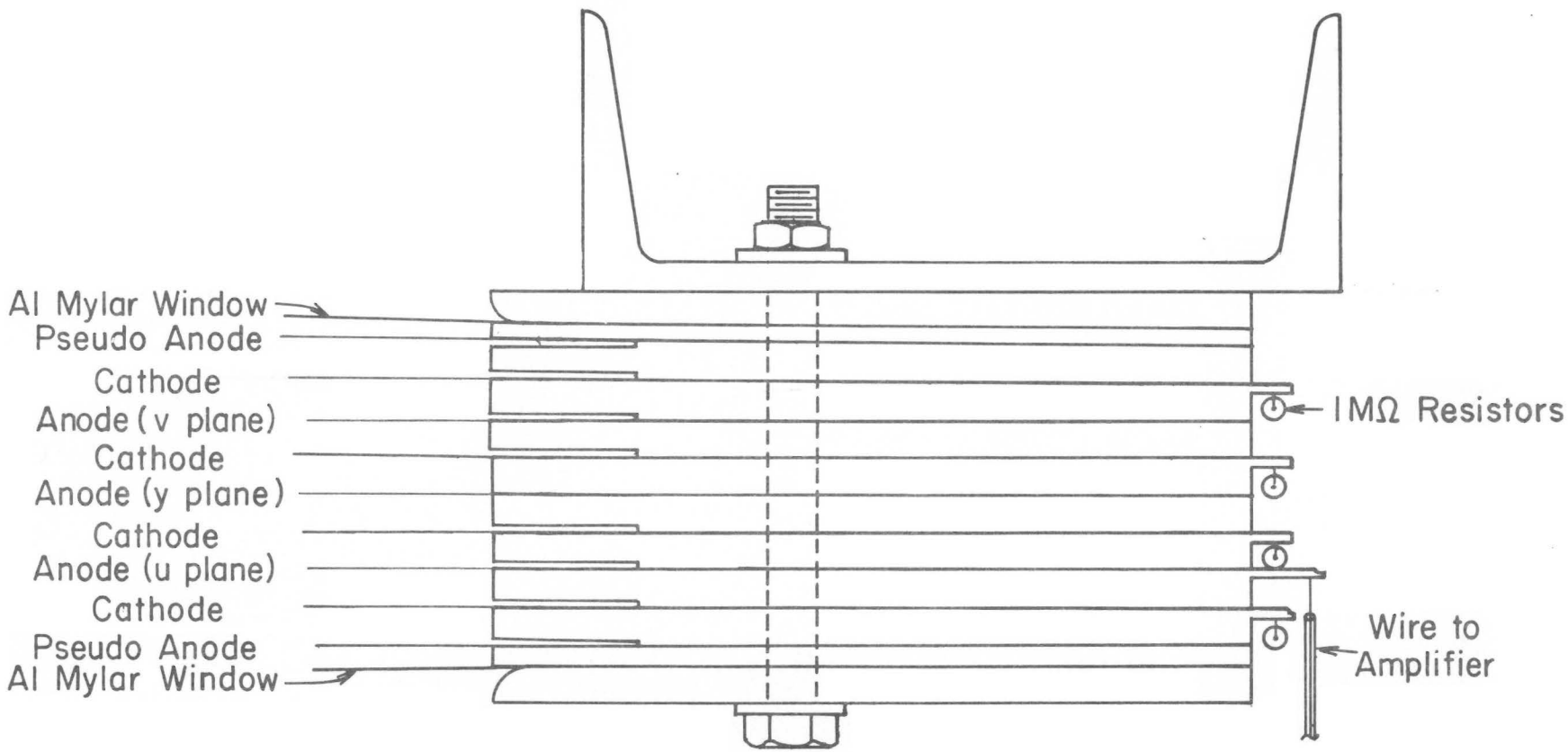

Figure F.1
Cross section view of upper part of UI MWPCs in the plane X = 0

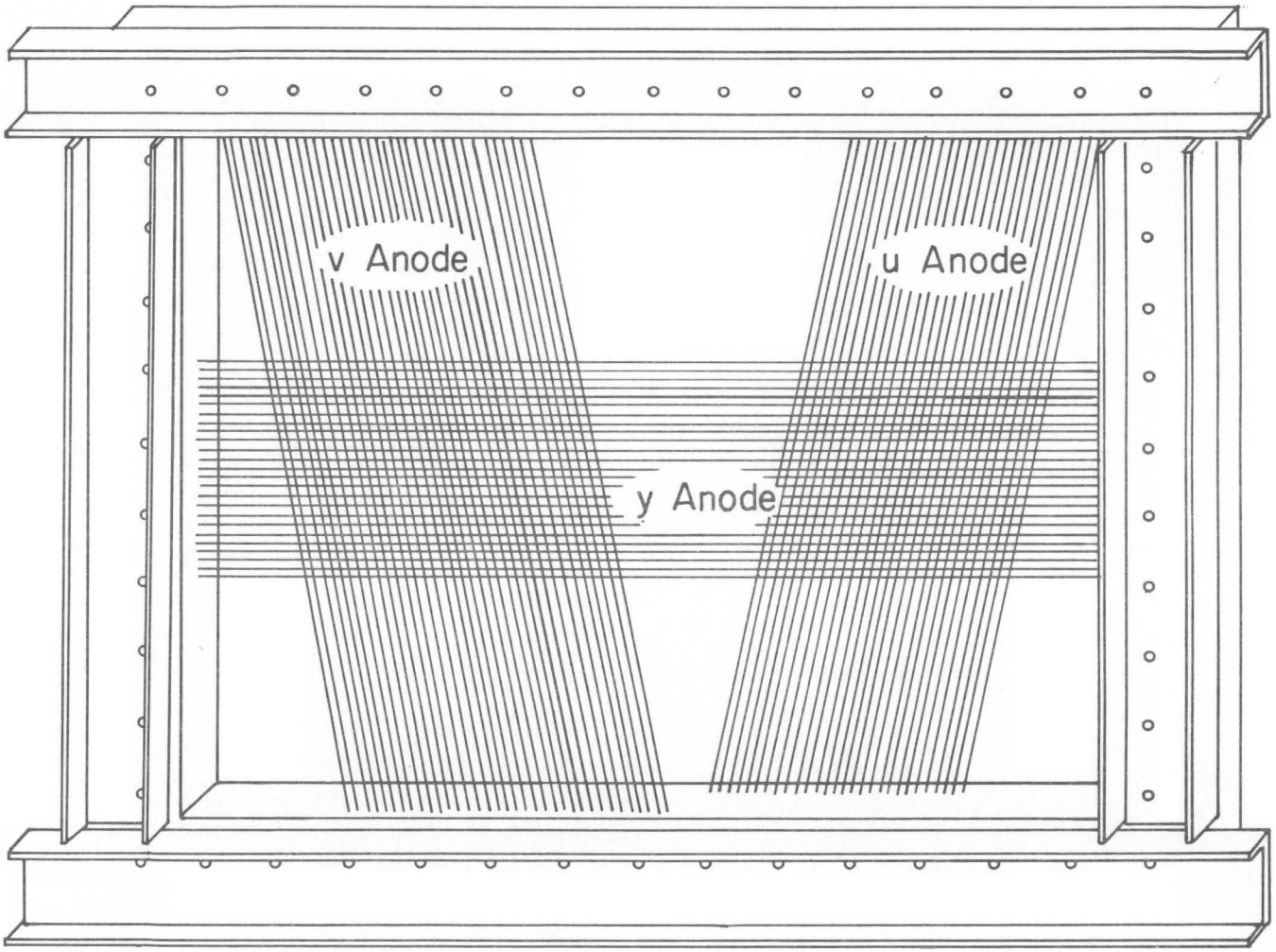

Figure F.2
View looking downstream of UI MWPC

about 75 gm. The low wire tension successfully avoided breakage of anode wires but necessitated support wires to stabilize the geometry. These will be described later.

The U and V anode wires were tilted 11 degrees from the vertical in opposite directions. The wire spacing for these planes was 1.96 mm. The wires for the Y plane were horizontal with a spacing of 2 mm.

The 3 outermost wires on the anode planes were 7, 4 and 2.5 mil beryllium-copper wire with the 7 mil wire being at the edge of the plane. These wires are called guard wires. Their purpose is to prevent breakdown from taking place at the edge of the anode plane. The wire tension on the 7, 4, 2.5 mil wires was 300 gm, 200 gm and 60 gm, respectively.

The cathode plane consisted of 4 mil beryllium-copper wires with a wire tension of 200 gm. The wire spacing for the cathode plane was 1 mm. The wires were vertical with a length of 38 inches.

Approximately 25 cathode wires were soldered in parallel to one printed circuit board pad. This pad was connected to a high voltage bus by a 1 megohm 1/4 watt resistor. This resistor is a current limiting resistor which prevents the entire electrostatic energy of the chamber from discharging into a short, if one should occur. The chamber is more likely to be severely damaged if all the charge in the chamber discharges through the short. In the event of a discharge, these resistors should not short out the chamber voltage, which is 4000 volts. It was found that 1 MΩ carbon resistors rated at 1/2 watt or higher would have been better. In spite of the large amount of current the chambers drew in the beam region, about 70 μa,

the inefficiency in the beam region was shown not to be due to the large size of the resistors. Hence, we feel that the value of 1 MΩ was a suitable choice.

The pseudo anode plane consisted of 4 mil beryllium-copper wire with a wire spacing of 2 mm and wire tension of 200 gm. The pseudo anode makes the voltage characteristics of the tilted (outer) anodes similar to the Y anode. Without the pseudo anode the outermost cathodes may be pulled slightly inward toward the tilted anode planes. This would make the plateau region of the tilted planes smaller.

The pseudo anode wires were glued onto a 1/8 inch aluminum frame. Except for the thickness, this frame had the same dimensions as the cathodes and anodes. The wires made electrical contact to this frame by being soldered to another wire which was electrically attached to the aluminum frame by 2 screws and conducting epoxy. The pseudo anode frame made mechanical contact with the window frames. Since the window frames made contact with the chamber body, the voltage of the pseudo anode was the same as the chamber body, i. e. ground.

The window was a laminate of 2 mils of mylar on the outside and 1 mil of aluminum on the inside. The purpose of the aluminum was to prevent moisture from leaking though the mylar. The window was glued onto a 1/4 inch aluminum frame. This frame has the same dimensions as the cathode and anode frames.

F.2 Support Wire

When voltage is applied to a chamber, the charges on the anode

wires cause them to repel each other. If there is no restoring force, this configuration is unstable with the wires being displaced from the center of the plane. For large chambers the anode wires will alternate with one wire closer to one high voltage plane and the next wire closer to the other high voltage plane. The restoring force is provided by the wire tension. For a fixed wire tension, there is a critical length above which the instability will set in. This critical length is given in the formula below derived in Sauli (44).

$$L_c = \frac{s}{CV_0}\sqrt{4\pi\varepsilon_0 t}$$

where

1. $C = 2\pi\varepsilon_0/[(\pi l/s) - \ln(2\pi a/s)]$

2. t is the tension of the anode wire, 40 gm.

3. s is the wire spacing, 2mm.

4. l is the distance between the cathode plane and the anode plane, 6.25 mm.

5. a is the wire radius, .01 mm.

Plugging in all the numbers gives 80 cm. Hence, the anode wires needed support wires in order to prevent this instability.

The configuration of the support wire was the same as that given in Charpak et. al. (45) (See Figure F.3). The support wire consisted of a number 26 polyvinyl chloride insulated copper wire.

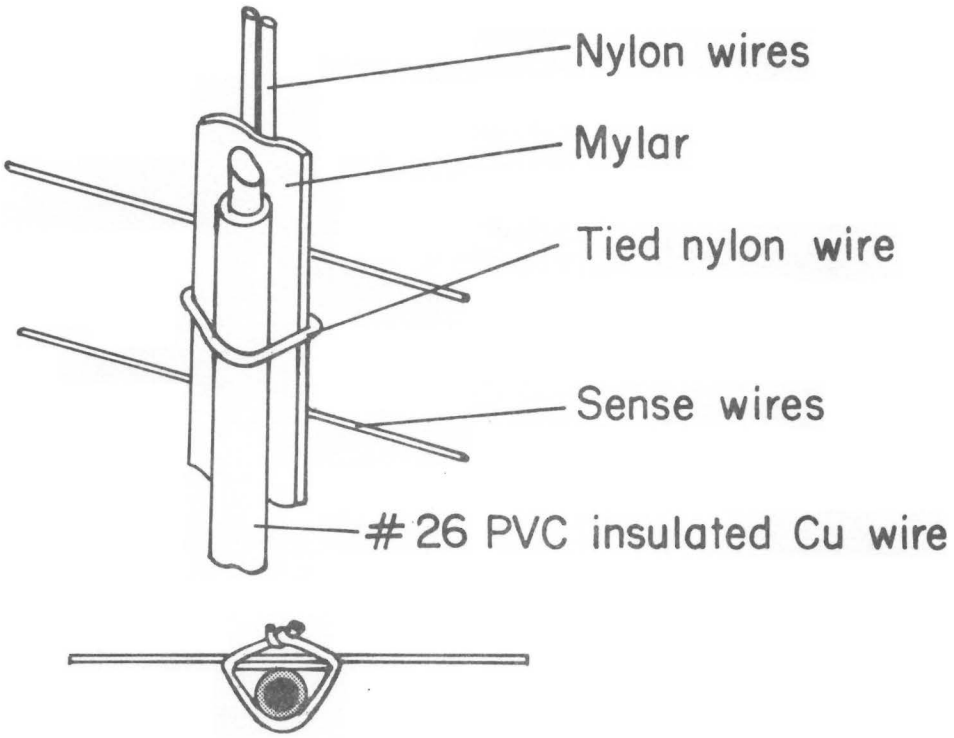

Figure F.3
Support wire configuration

In order to reduce the dead region around the support wire, this wire was at - 2500 volts while the chambers were operating. Between the support wire and the anode wires was a mylar strip 5 mil thick and 50 mil wide. This mylar strip prevented breakdown between the insulated support wire, which is at - 2500 volts, and the anode wires which were near ground. The anode wires lay on top of and perpendicular to the mylar strip. Two 4-mil diameter nylon wires lay on top of the anode wires, pressed the anode wires to the mylar strip, and prevented the electrostatic instability from taking place. This configuration was tied together every 6 cm using the same nylon wires which lay on top of the anode wires (see Figure F.3).

The support wire configuration was installed using the following procedure. Figure F.4 illustrates the machining done to the G - 10 frames for the support wire. The copper wire is first inserted into the groove perpendicular to and at the inner edge. It is then fed into the groove which goes out to the outer edge of the frame. The wire in the groove had its insulation removed with the exception of 1/4 inch of it at the inner edge. No insulation was removed from the support wire in the open region of the frame. The wire was hung over pullies and loaded with 1700 gm. After several hours the groove was filled with APCO R-313 epoxy. Next, a mylar strip 50 mils wide and 5 mils thick was stretched for about 12 hours with 1400 gm tension to remove all the kinks. Then, 1100 gm of weight was removed and the mylar strip was held under 300 gm of tension for about 20 hours. The mylar strip was placed over the copper wire with 300 gm of tension. It was then glued into place in the milled section beyond the groove where the support wire sits. Next, the plane was wound with anode

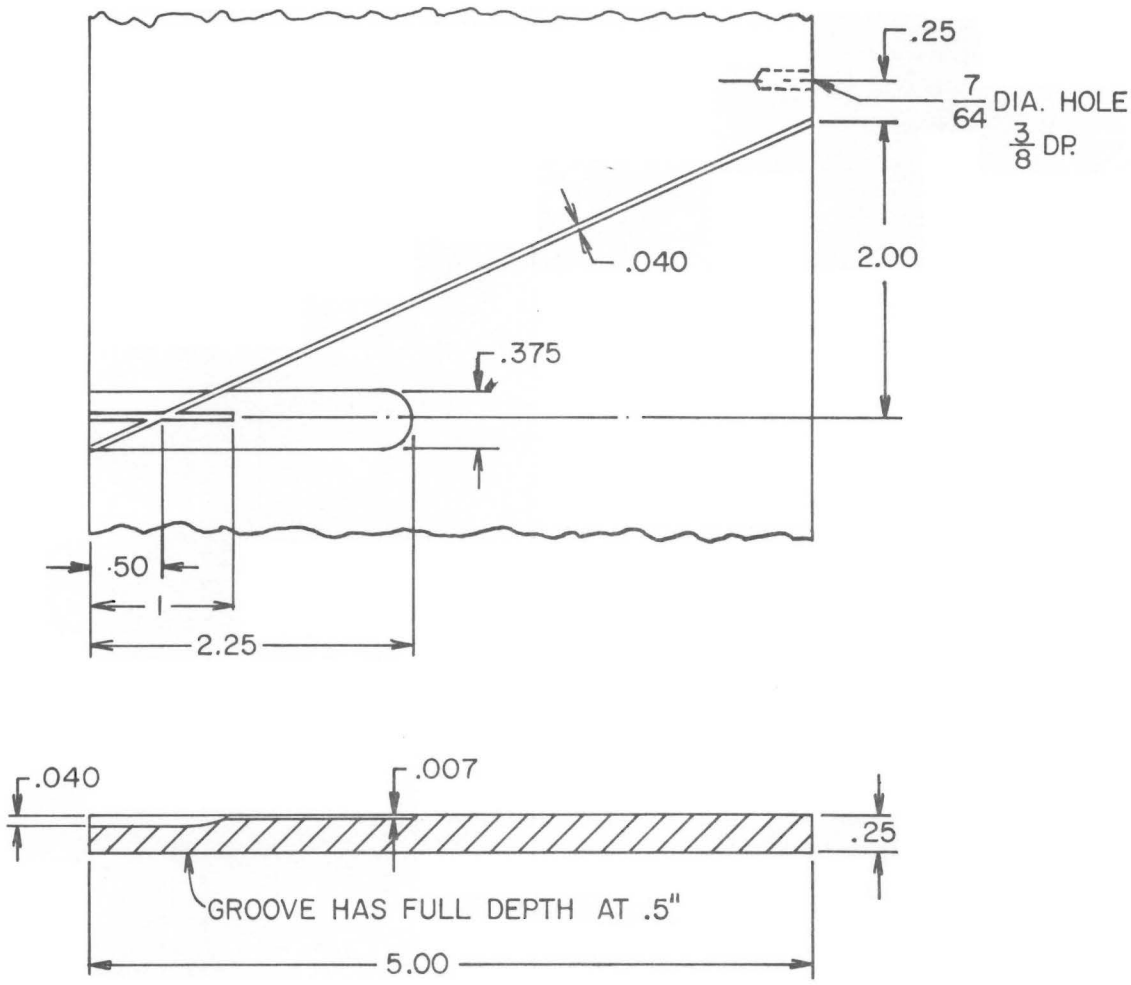

CROSSING GROOVES: .040 ± .002 DP. x .040 WIDE

MILLED SECTION: 2-1/4" LG. x 3/8" WIDE x .007 DP.

Figure F.4
Machining done to the G-10 frames for the support wire
(All units in inches)

wires. After the plane was wound, two 4 mil nylon wires were placed above the mylar strip. They were each put under a tension of 250 gm. The nylons were given about 30 hours to stretch, after which they were glued into place using the region beyond where the mylar strip was glued and where no machining took place. The copper support wire at the outer edge was soldered to a post glued into the frame so that the wire could later be connected to high voltage. All gluing for the support wire was done with APCO R-313 epoxy.

The tilted anodes had one horizontal support wire. The support wire for the V plane was 4 inches above the center of the plane while the support wire for the U plane was 4 inches below the center of the plane. The Y plane had 2 vertical support wires. One was left of the center of the plane by 8.5 inches while the other was right of the center of the plane by 8.5 inches.

The support wire was connected to high voltage in order to increase the efficiency of the area around it. Figure F.5 shows the efficiency as a function of the high voltage of the support wire. The data for this plot was taken using a ruthenium beta source on one side of the chamber and 2 one-inch scintillation counters on the other side. The source was pointing at one of the Y anode support wires. An event required a coincidence in the scintillation counters and a hit on the U plane. The coordinate at the bottom of Figure F.5 gives the hit wire in the U plane. The vertical axis gives the efficiency of the Y plane for a hit on a particular U wire. The plot of efficiency of the Y plane vs the U hit wire is the plot of the efficiency of the Y plane across the support wire. We can see that the dead region around the support wire becomes very small if the

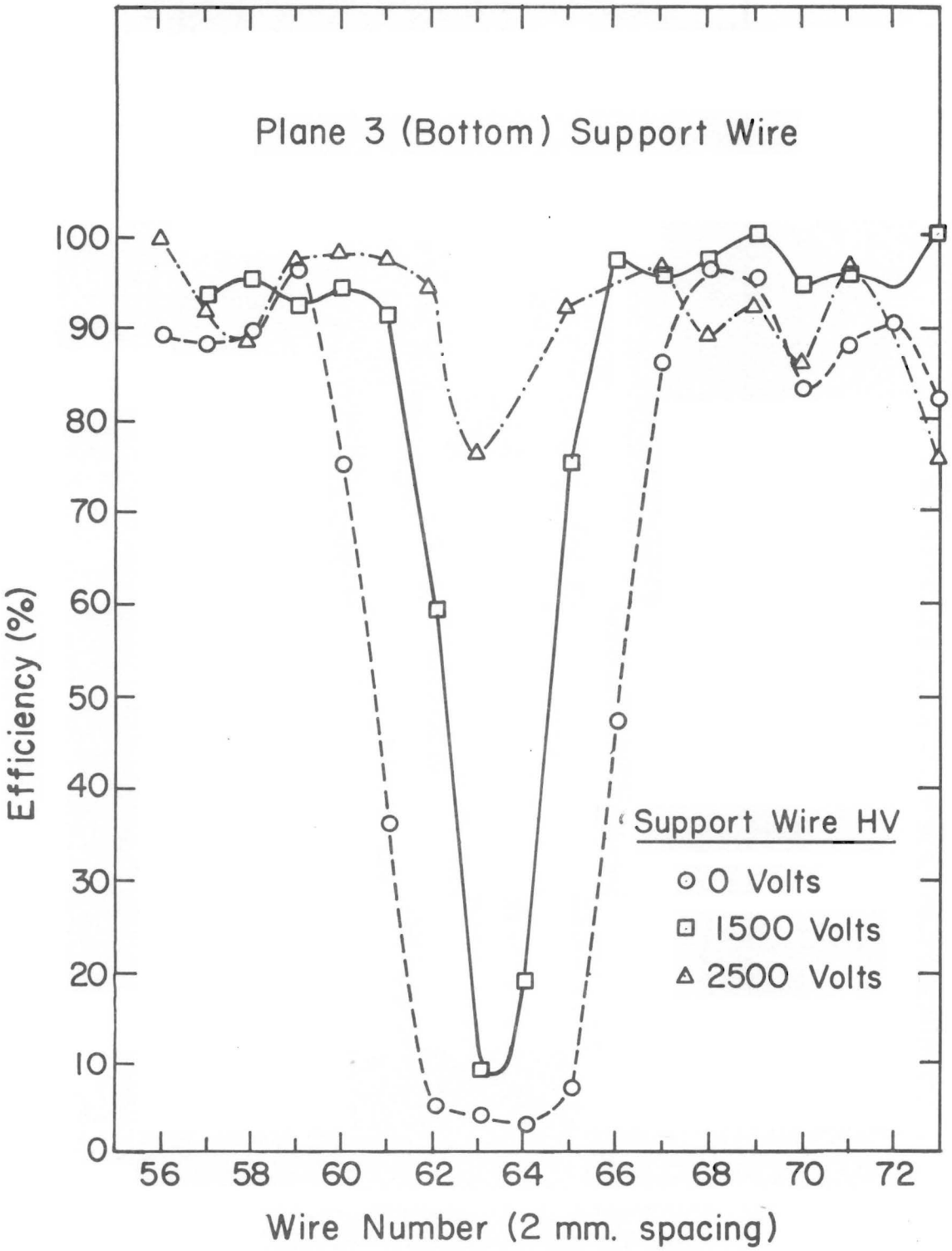

Figure F.5
Chamber efficiency near support wire

support wire voltage is below - 2000 volts. We set the support wire voltage at - 2500 volts for the run.

F.3 Prestressing

All the frames were prestressed before they were wound to insure that their wires were at the correct tension. The total force on the cathode frames from the wires was 240 kg (1200 wires times 0.2 kg tension). This force caused the middle of the frame to deflect about 150 mils. However, the total amount each cathode wire stretched during the winding was 75 mils. Hence, the cathode wires would not have the correct tension if the cathode frame was not prestressed into its final configuration before gluing the wires onto the frame. The anode frames were also prestressed before winding, although it was not as crucial.

To prestress the frames the following procedure was used. The frame was put on a 1/2 inch thick upright aluminum prestress plate. Screws which were only finger tight supported the chamber frame on the prestress plate. Two one-inch wide bars held the frame at the bottom. These bars were 10 inches on either side of the center of the frame. These bars are illustrated in Figure F.6. Point A in Figure F.6 indicates their position for the cathode, pseudo anode and tilted anode. Point B in Figure F.7 indicates their position for the Y anode. Next, one inch wide bars pressing on the top of the frames were loaded with weight. These bars also were each 10 inches away from the center of the frame. Point A′ in Figure F.6 indicates their position for the cathode, pseudoanode and tilted anode. Point B′ in Figure F.7 indicates their position for the Y anode. The sum of the

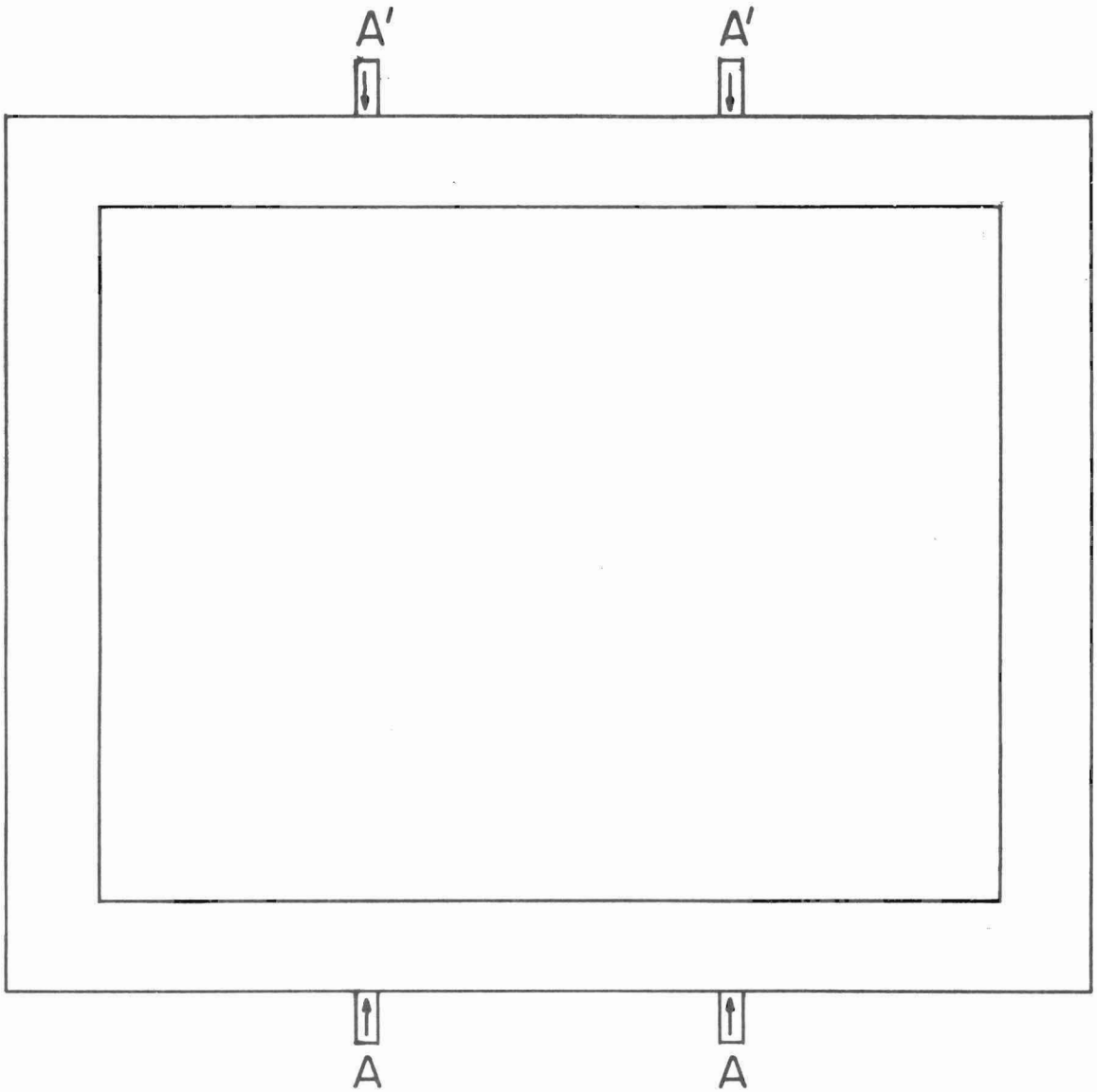

Figure F.6
Prestress points for the cathode,
pseudo anode and tilted anode frame

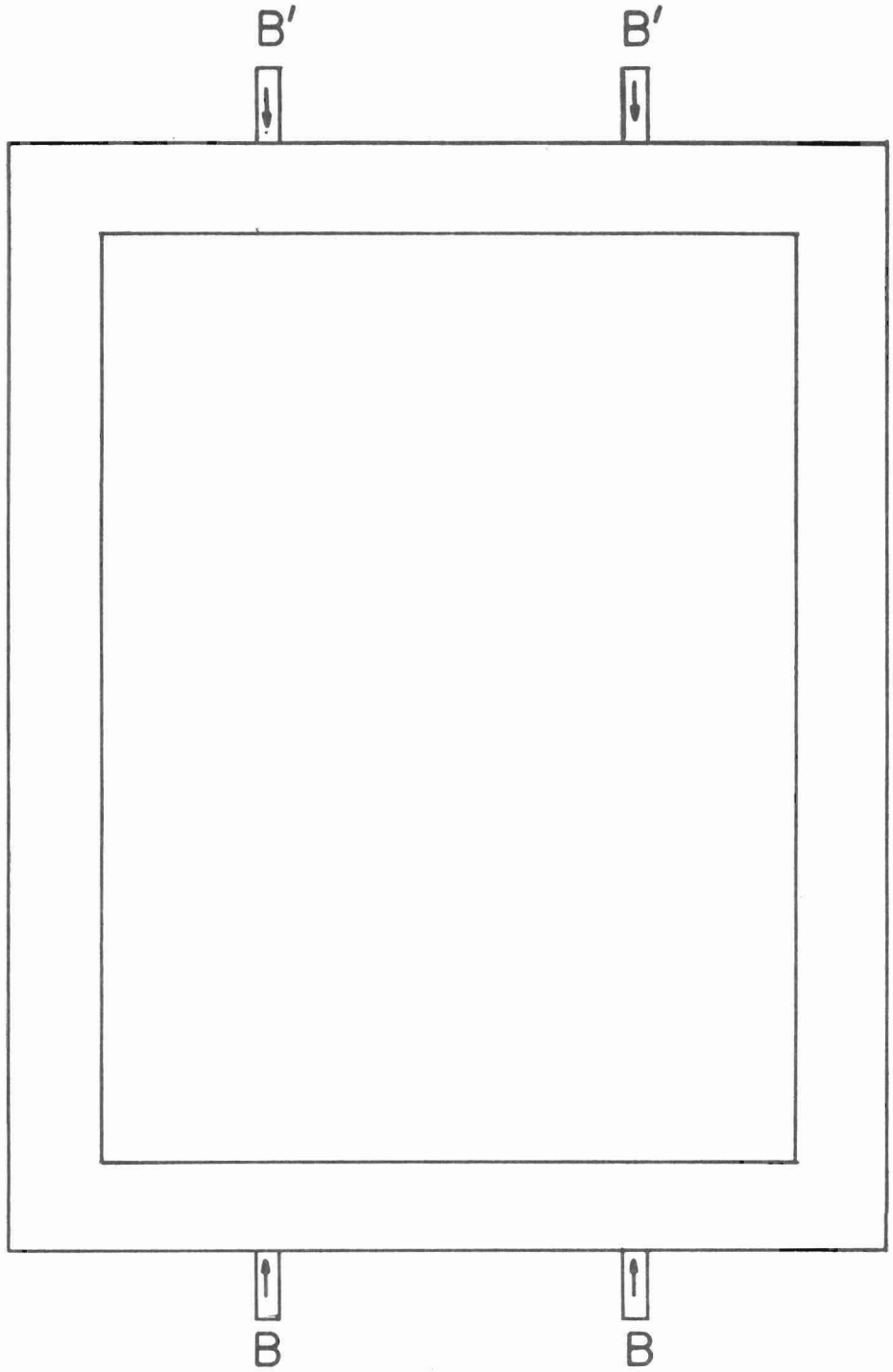

Figure F.7
Prestress points for the Y anode frame

weight on both bars was approximately equal to the total load on the frame due to the wires. For the cathode, pseudo anode and Y anode the weight on each bar was 103 kg, 51.5 kg and 9.4 kg, respectively. For the tilted anode the amount of weight on the two bars was different. To prestress the V anode with the same wire orientation shown in Figure F.1, the left bar was loaded with 13.9 kg and the right bar was loaded with 6.3 kg. In order to counteract the torque on the frame, the right hand edge near the bottom was held fixed while the left hand edge at the top was moved 9 mils to the right. After the weights were hung on these bars, the bars were fixed in position. The weights were removed and the frames were ready to be wound.

The prestressing of the frames succeeded in keeping the wire tension of the planes the same as the wound wire tension. The tension of the cathode wires near the edge was 200 gm, the same as the wound tension. The tension in the middle of the plane was about 185 gm. Hence, the prestressing was able to keep the cathode wire tension within 7% of its wound value.

F.4 Winding

The prestress plates with the chamber frames on them were bolted onto a rotating frame of a winding machine. One plate was put on one side while another plate was put on the other side so that two planes were wound at once. One end of the wire was taped to the edge of the chamber frame. The winding frame rotated to wind the wires onto the chamber frame. The wire spacing was determined using a stepping motor and a lead screw. Using this method, we were able to get wire

spacings of 1., 1.96 and 2 mm.

The 200 gm tension for the cathode wire was maintained by a weight on a pulley. The 40 gm tension for the anode wires was maintained by a hysteresis motor. The wire tension was measured during the anode wind by a Schmidt guage made by Electromatic Equipment Co. Both methods worked well in maintaining the wires at a constant tension. The one sigma variation in the anode tension was about 2%. The variation in cathode wire tension due to the winding was less than 2%. The only variation in the cathode wire tension was the 7% change due to the prestressing.

F.5 Gluing

The wires were glued to the G-10 frames using APCO R-313 from Applied Plastics Company. This epoxy was able to hold the wire tension and had only a 12 hour setting time. For gluing the wires onto the aluminum pseudo anodes, an epoxy which sets softer than APCO is needed because temperature variations could cause the bond between the aluminum and the epoxy to weaken. We chose 3 M structural epoxy to glue the wires onto aluminum. It does not set so hard as APCO epoxy does.

The procedure for gluing the wires onto the chamber frame is the following. The epoxy is first put on mylar strips which are 5/16 in wide and longer than the width of the chamber frame. The mylar strip with the epoxy is put on the chamber frame by means of a "guillotine". The guillotine consists of 2 jacks attached by a long bar so that the distance between the jacks is greater than the length of the frame. Next, the mylar strip is attached at the ends to the

long bar so that the mylar strip rests under the long bar. The side of mylar with the epoxy faces down. The two jacks are placed next to the edge of the of the chamber frame so that the mylar strip is over the region of the wires which needs epoxy. Next, the jacks lower the mylar onto the wires creating a band of epoxy about 5/16 of an inch wide. The mylar is cut loose from the bar and left on the wires with the epoxy. This method causes minimal movement of the wires during the gluing process.

In order to tell how accurately the wires were placed after they were wound and glued, we measured the wire spacing of a tilted anode with a traveling microscope. A total of 26 wire spacings were measured. The average wire spacing was 1.961 mm with a one sigma variation of .021 mm, about 1%. The largest variation was .041mm. Sauli [44] states that a 1% variation in the wire spacing will induce a 15% variation in the gas gain at the wire.

The wires of cathode and pseudo anode plane put enough force on the frames so that they would bow outward if they were not supported. The bowing of the frames caused a kink in the wire at the epoxy joint. To prevent the bowing from happening, the cathode and pseudo anode frames were always supported so that at no point from the time the planes were wound until the time the chambers were assembled were the planes allowed to bow. We felt preventing the frames from bowing would lessen the chance a wire would break.

F.6 Cleaning

The planes were cleaned and stacked in a clean room to reduce the contamination getting on the wires. The people cleaning the

frames wore hoods to prevent hair and lint from getting on the planes.

First, all lint was removed from the wires. Next, the wires were sprayed with ethanol using dry nitrogen. Cathode wires were wiped with amylacetate and trichloroethylene in regions where they were dirty. The inner edges of the planes were sprayed with trichloroethylene and ethyl alcohol. After being sprayed, the planes were dried with dry nitrogen.

F.7 Flattening

The 1/r electric field around the wire becomes stronger if the entire anode plane moves toward either cathode plane, even though the distance between the cathode planes remains constant. This will induce a higher gas gain for those wires and will reduce the width of the plateau.

In order to keep the anode centered between the cathodes, we flattened the chambers. The procedure for flattening the chambers was the following. First, the chamber was stacked, but the bolts were not yet tightened. Next the chamber was put on a granite block with the channel side (see Figure F.1 and F.2) up. The bolts were kept off the granite block by resting the chamber on 1/2 inch square bars. Next, the plane was loaded with 800 lbs of lead bricks. The bolts were then tightened while the chamber lay on the granite block.

After the chambers were flattened, the chambers were surveyed to determine how far the anode plane was from the mid-point between the two cathodes. The average deviation was about 12 mils with the maximal deviation about 25 mils.

F.8 Sealing

RTV-11 was used to make the chambers gas tight. After the planes were stacked, the outer edge where all the frames came together was covered with RTV. This region is shown in the upper part of Figure F.2. The bolts and nuts used to hold the frames together were covered with RTV to prevent gas leaks through the bolt holes.

F.9 Chamber Operations

We operated the chambers at 3950 volts. Because the tilted anodes had a wire spacing of 1.96 mm while the Y anode had a wire spacing of 2 mm, the plateau of the tilted anode planes started about 50 volts higher than the plateau of the Y anode. To correct this, the inner cathode planes which sandwiched the Y plane were put on a different high voltage power supply from the outer cathodes. The high voltage of the outer cathode planes was set about 80 volts higher than the inner cathodes. This arrangement made the efficiency of the tilted anode planes nearly the same as the Y anode planes.

If one of the 2 power supplies turned off, then one cathode next to the tilted anode would have 0 volts while the other would have -4000 volts. The cathode with - 4000 volts would attract the anode and cause the two planes to touch. This would destroy the chamber. To prevent this from happening, the two power supplies were connected with two 100-volt back-to-back Zener diodes connected in series. If the voltage difference between the cathodes became greater than 100 volts, then the Zener diodes would conduct. This prevented the difference between the cathode plane from becoming greater than 100

volts.

The gas we used was 80% argon, 20% CO^2, and .5% freon. We found the plateau width was maximized by using .4% freon. Since we could get premixed gas with .5% freon, we decided to use .5% freon instead of 0.4% freon. The 0.1% difference had little effect on the plateau. This mixture has the advantage of being nonflammable and not causing build up of contamination on the cathode wires during high intensity running.

The typical intensity for E610 was 2.5-3.0 million particles per 1.5 second spill. In the beam region the chambers drew about 70 μa. The whole chamber drew about 200 μa. The efficiencies for the chambers are given in the Appendix D.

The chamber wires did not break during their operation. The chambers were first used for E610 at Fermilab. A year and half later they were used for E673. During this time none of the 6 chambers built broke any wire. The chambers always held high voltage and never had to be repaired.

APPENDIX G

EQUIPMENT FILE

The equipment file for E610 given in this section contains all the constants used in the analysis program. We have removed from the printout quantities which do not relate to the position of equipment.

The chamber constant section has the alignment constants for all the wire planes in E610. FIDLO and FIDHI are the address numbers of the lowest and highest wires of a chamber. XCENT and YCENT are the X and Y coordinates of the point which is both closest to the XY origin and on the line parallel to and half way between the FIDLO wire and FIDHI wire. ZCENT gives the Z coordinate of the wire plane. THETW gives the angle in degrees between the vertical and the wires of the plane. A plane with THETW = 0 has vertical wires. WSPACE gives the wire spacing of the planes. The wire spacing for each UI plane was individually measured. Those values are recorded in the equipment file.

Several numbers used in the analysis are not recorded in the equipment file. They are the following. The Z center of the magnet 1E41 is -5137.9 cm. The Z center of the magnet used to steer electrons into individual lead glass blocks is -1440 cm. The drift chambers cells are active between -76 cm and 76 cm in Y.

******* CHAMBER CONSTANTS ********

IPLN	FIDLO	FIDHI	XCENT	YCENT	ZCENT	THETW	WSPACE
BEAM CHAMBERS							
1	2	96	.120	.160	-13194.900	0.000	.211667
2	98	192	.139	0.000	-6152.790	0.000	.211667
3	194	288	-.740	.120	-4069.720	0.000	.211667
4	290	384	-.580	-.020	-4067.220	90.000	.211667
5	386	480	.060	.010	-960.890	0.000	.211667
6	482	575	.040	-1.100	-958.110	90.000	.211667
80 CM CHAMBERS							
7	2	513	0.000	-3.053	-567.780	90.030	.158750
8	514	1025	.050	0.000	-555.080	.094	.158750
9	2	513	0.000	-3.010	-517.140	90.110	.158750
10	514	1025	-.240	0.000	-504.440	.040	.158750
11	2	513	0.000	-2.900	-466.500	90.150	.158750
12	514	1025	.380	0.000	-453.800	.060	.158750
13	2	513	0.000	-2.950	-416.020	89.850	.158750
14	514	1025	2.120	0.000	-403.320	-.090	.158750
15	2	513	.973	.973	-372.360	44.782	.158750
16	514	1025	-.777	.777	-359.660	-45.100	.158750
UNIV OF ILLINOIS CHAMBERS							
17	1	528	-.020	.004	-249.770	-11.483	.196100
18	1	480	0.000	-.001	-248.500	89.820	.199900
19	1	528	-.063	-.013	-247.230	11.120	.196109
20	1	528	.165	-.033	-181.470	-11.305	.196400
21	1	480	0.000	-.120	-180.200	89.930	.200100
22	1	528	-.117	-.023	-178.930	11.088	.196400
23	1	528	.059	-.012	-91.470	-11.281	.196102
24	1	480	0.000	-.150	-90.200	89.910	.199700
25	1	528	-.106	-.021	-88.930	11.281	.196020
26	1	528	.199	-.041	46.030	-11.264	.196089
27	1	480	0.000	.029	47.300	89.944	.199800
28	1	528	.105	.022	48.570	11.263	.196000
29	1	528	.022	-.008	170.530	-10.960	.195970
30	1	480	0.000	.001	171.800	90.210	.199900
31	1	528	-.053	-.011	173.070	11.630	.196100
DRIFT CHAMBERS							
32	1	60	1.139	0.000	340.600	-.020	4.000000
36	1	60	-1.846	0.000	402.800	-.080	4.000000
40	1	60	.402	0.000	812.000	-.020	4.000000
PROPORTIONAL TUBES							
51	1	194	-10.410	-1.340	958.800	-.060	.793750
52	1	194	-10.210	-1.320	961.800	59.570	.793750
53	1	194	-11.190	-1.510	965.000	-60.270	.793750

***** PASSIVE EQUIPMENT ******

	XLO	XHI	YLO	YHI	ZLO	ZHI	NAME
1	-1000.00	1000.00	-156.00	500.00	-1351.18	3000.00	MUON LAB
2	-6.59	6.59	-4.48	3.14	-744.91	-737.29	TARGET
3	-303.00	297.00	-156.00	174.00	431.00	744.00	CERENKOV
4	-66.68	51.12	-44.45	50.80	946.14	958.84	TUFTS PB GLASS
5	-15.24	0.00	-3.18	3.18	-8.26	-7.30	TUFTS PB HOLE
6	-103.00	97.00	-100.00	100.00	958.84	969.00	P-TUBE FRAME
7	-74.70	74.70	-67.50	67.50	969.00	1060.50	UI & L PB GLAS
8	-230.00	230.00	-156.00	109.00	1125.00	1215.00	ABSORBER 1
9	-375.00	375.00	-156.00	209.00	1215.00	1465.00	ABSORBER 2
10	-64.40	64.40	-82.15	82.15	220.00	320.00	CCM Y'S & RADI

****** HODOSCOPES ******

	XLO	XHI	YLO	YHI
1 BEAM HODOSCOPE 1			Z COORDINATE -13168.20	
1	-9.990	-7.450	-10.230	10.090
2	-7.450	-4.910	-10.230	10.090
3	-4.910	-2.370	-10.230	10.090
4	-2.370	.170	-10.230	10.090
5	.170	2.710	-10.230	10.090
6	2.710	5.250	-10.230	10.090
7	5.250	7.790	-10.230	10.090
8	7.790	10.330	-10.230	10.090
2 BEAM HODOSCOPE 2			Z COORDINATE -6129.93	
1	-7.520	-5.620	-10.160	10.160
2	-5.620	-3.710	-10.160	10.160
3	-3.710	-1.800	-10.160	10.160
4	-1.800	.100	-10.160	10.160
5	.100	2.000	-10.160	10.160
6	2.000	3.910	-10.160	10.160
7	3.910	5.820	-10.160	10.160
8	5.820	7.720	-10.160	10.160
3 BEAM HODOSCOPE 3			Z COORDINATE -4034.52	
1	-8.080	-6.170	-10.070	10.250
2	-6.170	-4.260	-10.070	10.250
3	-4.260	-2.360	-10.070	10.250
4	-2.360	-.460	-10.070	10.250
5	-.460	1.450	-10.070	10.250
6	1.450	3.360	-10.070	10.250
7	3.360	5.260	-10.070	10.250
8	5.260	7.160	-10.070	10.250
4 BEAM HODOSCOPE 4			Z COORDINATE -4033.26	
1	-10.610	9.700	-7.530	-5.620
2	-10.610	9.700	-5.620	-3.720
3	-10.610	9.700	-3.720	-1.820
4	-10.610	9.700	-1.820	.090
5	-10.610	9.700	.090	2.000
6	-10.610	9.700	2.000	3.900
7	-10.610	9.700	3.900	5.800
8	-10.610	9.700	5.800	7.710

	XLO	XHI	YLO	YHI
5 BEAM HODOSCOPE 5			Z COORDINATE	-925.40
1	-7.580	-5.680	-10.130	10.180
2	-5.680	-3.770	-10.130	10.180
3	-3.770	-1.870	-10.130	10.180
4	-1.870	.040	-10.130	10.180
5	.040	1.940	-10.130	10.180
6	1.940	3.850	-10.130	10.180
7	3.850	5.750	-10.130	10.180
8	5.750	7.660	-10.130	10.180
6 BEAM HODOSCOPE 6			Z COORDINATE	-924.14
1	-10.120	10.200	-8.690	-6.790
2	-10.120	10.200	-6.790	-4.880
3	-10.120	10.200	-4.880	-2.980
4	-10.120	10.200	-2.980	-1.080
5	-10.120	10.200	-1.080	.830
6	-10.120	10.200	.830	2.740
7	-10.120	10.200	2.740	4.640
8	-10.120	10.200	4.640	6.540

7 HADRON HODOSCOPE Z COORDINATE 763.00

	XLO	XHI	YLO	YHI
1	-240.000	-220.950	-102.000	-.400
2	-223.100	-204.050	-102.000	-.400
3	-206.200	-187.150	-102.600	-1.000
4	-193.000	-174.000	-103.100	-1.000
5	-177.000	-158.000	-103.100	-1.500
6	-160.250	-140.500	-103.350	-1.750
7	-143.750	-125.500	-103.100	-1.500
8	-126.500	-106.750	-103.850	-2.250
9	-109.500	-90.250	-103.100	-1.500
10	-92.250	-73.000	-103.350	-1.750
11	-74.750	-55.750	-103.600	-2.000
12	-57.750	-38.250	-103.100	-1.500
13	-41.250	-22.000	-103.350	-1.750
14	6.700	25.750	-103.350	-1.750
15	22.750	41.750	-103.600	-2.000
16	39.250	58.250	-103.850	-2.250
17	56.500	75.750	-103.350	-1.750
18	73.250	92.500	-102.850	-1.250
19	89.750	109.250	-103.350	-1.750
20	106.250	125.250	-103.350	-1.750
21	124.250	143.500	-103.100	-1.500
22	140.250	159.500	-103.100	-1.500
23	157.250	177.000	-103.100	-1.500
24	173.750	192.500	-104.100	-2.500
25	189.500	208.550	-103.100	-1.500
26	205.400	224.450	-103.100	-1.500
27	221.700	240.750	-101.900	-.300
28	-240.500	-221.450	4.200	105.800
29	-222.500	-203.450	1.500	103.100
30	-207.100	-188.050	1.500	103.100
31	-190.000	-170.950	1.500	103.100
32	-176.000	-157.000	1.000	102.600
33	-159.500	-139.750	1.000	102.600
34	-142.500	-123.750	1.250	102.850
35	-126.500	-107.500	.750	102.350
36	-109.750	-90.500	.750	102.350
37	-92.500	-73.500	1.000	102.600
38	-75.500	-56.750	1.000	102.600
39	-58.250	-39.250	1.000	102.600
40	-41.750	-22.700	1.000	102.600
41	6.700	25.750	1.000	102.600
42	22.250	42.000	.750	102.350
43	38.750	58.250	1.000	102.600
44	56.250	75.250	1.000	102.600
45	72.500	92.000	1.250	102.850
46	87.250	107.750	1.250	102.850
47	105.000	124.250	1.000	102.600
48	122.000	141.250	1.000	102.600

	XLO	XHI	YLO	YHI
49	138.750	158.000	1.500	103.100
50	156.250	176.000	1.500	103.100
51	171.750	190.800	1.500	103.100
52	188.300	207.350	1.000	102.600
53	204.600	223.650	1.000	102.600
54	220.500	239.550	4.200	105.800

8 MUON HODOSCOPE Z COORDINATE 1469.20

	XLO	XHI	YLO	YHI
1	0.000	0.000	0.000	0.000
2	0.000	0.000	0.000	0.000
3	0.000	0.000	0.000	0.000
4	0.000	0.000	0.000	0.000
5	-257.700	-227.220	-149.600	-27.680
6	-229.500	-196.480	-149.700	-27.780
7	-197.500	-167.020	-150.250	-28.330
8	-168.400	-137.920	-150.100	-28.180
9	-139.100	-111.160	-150.800	-28.880
10	-112.000	-84.060	-146.400	-24.480
11	-85.200	-57.260	-139.900	-17.980
12	-58.600	-43.360	-135.200	-13.280
13	-44.100	-28.860	-131.200	-9.280
14	-29.900	-14.660	-127.600	-5.680
15	-15.600	-.360	-127.200	-5.280
16	0.000	15.240	-127.200	-5.280
17	14.000	29.240	-127.700	-5.780
18	28.200	43.440	-130.700	-8.780
19	43.000	58.240	-134.800	-12.880
20	56.900	84.840	-139.600	-17.680
21	83.400	111.340	-146.000	-24.080
22	110.700	138.640	-150.000	-28.080
23	137.500	167.980	-150.000	-28.080
24	166.600	197.080	-150.000	-28.080
25	196.100	226.580	-149.900	-27.980
26	225.400	255.880	-150.000	-28.080
27	0.000	0.000	0.000	0.000
28	0.000	0.000	0.000	0.000
29	0.000	0.000	0.000	0.000
30	0.000	0.000	0.000	0.000
31	0.000	0.000	0.000	0.000
32	0.000	0.000	0.000	0.000
33	0.000	0.000	0.000	0.000
34	0.000	0.000	0.000	0.000
35	-258.400	-227.920	27.900	149.820
36	-228.600	-198.120	28.000	149.920
37	-199.600	-169.120	28.000	149.920
38	-170.200	-139.720	28.400	150.320
39	-141.000	-110.520	28.000	149.920
40	-111.500	-83.560	24.700	146.620
41	-84.700	-56.760	17.600	139.520
42	-58.100	-42.860	12.700	134.620
43	-43.900	-28.660	9.000	130.920
44	-29.900	-14.660	5.800	127.720
45	-15.900	-.660	5.000	126.920
46	0.000	15.240	5.000	126.920
47	14.100	29.340	5.700	127.620
48	28.100	43.340	9.000	130.920
49	42.500	57.740	12.400	134.320

	XLO	XHI	YLO	YHI
50	56.600	84.540	17.600	139.520
51	83.600	111.540	24.700	146.620
52	110.300	140.780	27.900	149.820
53	139.800	170.280	28.000	149.920
54	169.200	199.680	27.700	149.620
55	198.500	228.980	28.200	150.120
56	228.300	258.780	27.800	149.720
57	0.000	0.000	0.000	0.000
58	0.000	0.000	0.000	0.000
59	0.000	0.000	0.000	0.000
60	0.000	0.000	0.000	0.000

9 MUON PRIME HODOSCOPE Z COORDINATE 1514.80

1	-200.000	0.000	-36.200	-17.700
2	0.000	200.000	-36.200	-17.700
3	-200.000	0.000	-17.700	.400
4	0.000	200.000	-17.700	.400
5	-200.000	0.000	.400	18.500
6	0.000	200.000	.400	18.500
7	-200.000	0.000	18.500	36.700
8	0.000	200.000	18.500	36.700

***** CERENKOV PARAMETERS *****

CERENKOV COUNTER Z COORDINATE 700.00

	XLO	XHI	YLO	YHI
1	-314.000	-254.000	-114.000	-4.000
2	-254.000	-194.000	-115.000	-5.000
3	-194.000	-138.000	-118.000	-8.000
4	-138.000	-75.000	-119.000	-9.000
5	-75.000	-15.000	-118.000	-8.000
6	-1.000	61.000	-119.000	-9.000
7	61.000	119.000	-118.000	-8.000
8	119.000	181.000	-116.000	-6.000
9	181.000	241.000	-113.000	-3.000
10	-320.000	-260.000	-4.000	106.000
11	-260.000	-200.000	-5.000	105.000
12	-200.000	-141.000	-8.000	102.000
13	-141.000	-77.000	-9.000	101.000
14	-77.000	-17.000	-8.000	102.000
15	0.000	60.000	-9.000	101.000
16	60.000	119.000	-8.000	102.000
17	119.000	177.000	-6.000	104.000
18	177.000	237.000	-3.000	107.000

****** LEAD GLASS ARRAYS ******

	XPLO	XPHI	YPLO	YPHI	ZTHICK
1 MAIN ARRAY			Z COORDINATE		969.00
1	-78.563	-63.583	-68.980	-53.980	35.000
2	-63.583	-48.343	-70.410	-55.300	45.000
3	-48.343	-32.953	-70.410	-55.250	45.000
4	-32.953	-17.723	-70.410	-55.330	45.000
5	-17.723	-2.493	-70.410	-55.230	45.000
6	-2.493	12.747	-70.250	-55.010	45.000
7	12.747	27.987	-70.410	-55.250	45.000
8	27.987	43.397	-70.410	-55.250	45.000
9	43.397	58.742	-70.410	-55.250	45.000
10	58.742	73.687	-68.950	-53.910	35.000
11	-78.863	-63.833	-53.980	-39.090	35.000
12	-63.833	-48.343	-55.300	-40.250	45.000
13	-48.343	-32.953	-55.250	-40.010	45.000
14	-32.953	-17.713	-55.330	-40.120	45.000
15	-17.713	-2.418	-55.230	-39.930	45.000
16	-2.418	12.972	-55.010	-39.850	45.000
17	12.972	28.257	-55.250	-40.010	45.000
18	28.257	43.557	-55.250	-40.010	45.000
19	43.557	58.817	-55.250	-40.010	45.000
20	58.817	73.787	-53.910	-39.060	35.000
21	-78.863	-63.738	-39.090	-24.100	35.000
22	-63.738	-48.343	-40.250	-25.010	45.000
23	-48.343	-33.103	-40.010	-24.690	45.000
24	-33.103	-17.688	-40.120	-24.960	45.000
25	-17.688	-2.293	-39.930	-24.740	45.000
26	-2.293	12.947	-39.850	-24.530	45.000
27	12.947	28.337	-40.010	-24.850	45.000
28	28.337	43.577	-40.010	-24.770	45.000
29	43.577	58.817	-40.010	-24.690	45.000
30	58.817	73.867	-39.060	-24.050	35.000
31	-78.713	-63.888	-24.100	-9.320	35.000
32	-63.888	-48.498	-25.010	-9.690	45.000
33	-48.498	-33.258	-24.690	-9.450	45.000
34	-33.258	-17.863	-24.960	-9.770	45.000
35	-17.863	-2.443	-24.740	-9.510	45.000
36	-2.443	12.937	-24.530	-9.210	45.000
37	12.937	28.337	-24.850	-9.770	45.000
38	28.337	43.577	-24.770	-9.530	45.000
39	43.577	58.817	-24.690	-9.450	45.000
40	58.817	74.017	-24.050	-8.970	35.000
41	-79.193	-64.068	-9.320	5.660	35.000
42	-64.068	-48.673	-9.690	5.630	45.000
43	-48.673	-33.253	-9.450	5.790	45.000
44	-33.253	-17.793	-9.770	5.550	45.000
45	-17.793	-2.473	-9.510	5.790	45.000

	XPLO	XPHI	YPLO	YPHI	ZTHICK
46	-2.473	12.917	-9.210	6.030	45.000
47	12.917	28.312	-9.770	5.550	45.000
48	28.312	43.552	-9.530	5.710	45.000
49	43.552	58.892	-9.450	5.850	45.000
50	58.892	74.087	-8.970	5.790	35.000
51	-78.863	-63.738	5.660	20.630	35.000
52	-63.738	-48.598	5.630	20.840	45.000
53	-48.598	-33.258	5.790	21.030	45.000
54	-33.258	-17.713	5.550	20.870	45.000
55	-17.713	-2.393	5.790	21.030	45.000
56	-2.393	12.947	6.030	21.270	45.000
57	12.947	28.337	5.550	20.710	45.000
58	28.337	43.577	5.710	20.950	45.000
59	43.577	58.817	5.850	21.110	45.000
60	58.817	74.017	5.790	20.670	35.000
61	-78.863	-63.908	20.630	35.560	35.000
62	-63.908	-48.698	20.840	36.110	45.000
63	-48.698	-33.283	21.030	36.270	45.000
64	-33.283	-17.753	20.870	36.270	45.000
65	-17.753	-2.448	21.030	36.410	45.000
66	-2.448	12.947	21.270	36.510	45.000
67	12.947	28.187	20.710	36.110	45.000
68	28.187	43.577	20.950	36.350	45.000
69	43.577	58.972	21.110	36.560	45.000
70	58.972	74.177	20.670	35.560	35.000
71	-78.913	-63.833	35.560	50.640	35.000
72	-63.833	-48.623	36.110	51.320	45.000
73	-48.623	-33.083	36.270	51.350	45.000
74	-33.083	-17.713	36.270	51.430	45.000
75	-17.713	-2.168	36.410	51.510	45.000
76	-2.168	12.912	36.510	51.750	45.000
77	12.912	28.092	36.110	51.270	45.000
78	28.092	43.502	36.350	51.510	45.000
79	43.502	59.032	36.560	51.670	45.000
80	59.032	73.997	35.560	50.320	35.000
81	-79.013	-63.758	50.640	65.720	35.000
82	-63.758	-48.543	51.320	66.590	45.000
83	-48.543	-33.053	51.350	66.800	45.000
84	-33.053	-17.863	51.430	66.590	45.000
85	-17.863	-2.473	51.510	66.720	45.000
86	-2.473	12.767	51.750	67.070	45.000
87	12.767	28.007	51.270	66.510	45.000
88	28.007	43.427	51.510	66.750	45.000
89	43.427	58.687	51.670	66.910	45.000
90	58.687	73.537	50.320	65.480	35.000

	XPLO	XPHI	YPLO	YPHI	ZTHICK
91	-79.013	-63.763	65.720	80.800	35.000
92	-63.763	-48.733	66.590	81.600	35.000
93	-48.733	-32.953	66.800	81.810	35.000
94	-32.953	-17.863	66.590	81.600	45.000
95	-17.863	-2.473	66.720	81.730	45.000
96	-2.473	12.767	67.070	82.080	45.000
97	12.767	28.007	66.510	81.520	45.000
98	28.007	43.247	66.750	81.760	35.000
99	43.247	58.527	66.910	81.920	35.000
100	58.527	73.537	65.480	80.520	35.000

2 TUFTS ARRAY Z COORDINATE 950.00

	XPLO	XPHI	YPLO	YPHI	ZTHICK
1	-62.353	-3.933	-73.370	-66.940	6.350
2	-2.663	55.757	-73.380	-66.970	6.350
3	-62.353	-3.933	-66.940	-60.430	6.350
4	-2.663	55.757	-66.970	-60.495	6.350
5	-62.353	-3.933	-60.430	-53.920	6.350
6	-2.663	55.757	-60.495	-54.015	6.350
7	-62.353	-3.933	-53.920	-47.420	6.350
8	-2.663	55.757	-54.015	-47.540	6.350
9	-62.353	-3.933	-47.420	-40.910	6.350
10	-2.663	55.757	-47.540	-41.065	6.350
11	-62.433	-4.013	-40.910	-34.400	6.350
12	-2.663	55.757	-41.065	-34.585	6.350
13	-62.353	-3.933	-34.400	-27.890	6.350
14	-2.663	55.757	-34.585	-28.105	6.350
15	-62.353	-3.933	-27.890	-21.380	6.350
16	-2.663	55.757	-28.105	-21.635	6.350
17	-62.353	-3.933	-21.380	-14.880	6.350
18	-2.663	55.757	-21.635	-15.155	6.350
19	-62.353	-3.933	-14.880	-8.370	6.350
20	-2.663	55.757	-15.155	-8.650	6.350
21	-75.053	-16.633	-8.370	-1.860	6.350
22	-2.663	55.757	-8.650	-2.120	6.350
23	-75.053	-16.633	-1.860	4.675	6.350
24	-2.663	55.757	-2.120	4.410	6.350
25	-62.353	-3.933	4.675	11.235	6.350
26	-2.663	55.757	4.410	10.945	6.350
27	-62.353	-3.933	11.235	17.795	6.350
28	-2.663	55.757	10.945	17.475	6.350
29	-62.353	-3.933	17.795	24.355	6.350
30	-2.663	55.757	17.475	24.010	6.350
31	-62.353	-3.933	24.355	30.925	6.350
32	-2.663	55.757	24.010	30.540	6.350
33	-62.353	-3.933	30.925	37.485	6.350
34	-2.663	55.757	30.540	37.070	6.350
35	-62.353	-3.933	37.485	44.045	6.350
36	-2.663	55.757	37.070	43.600	6.350
37	-62.353	-3.933	44.045	50.605	6.350
38	-2.583	55.837	43.600	50.130	6.350
39	-62.353	-3.933	50.605	57.165	6.350
40	-2.823	55.597	50.130	56.665	6.350
41	-62.353	-3.933	57.165	63.730	6.350
42	-2.663	55.757	56.665	63.195	6.350
43	-62.353	-3.933	63.730	70.290	6.350
44	-2.823	55.597	63.195	69.730	6.350
45	-62.353	-3.933	70.290	76.855	6.350
46	-2.983	55.437	69.730	76.260	6.350
47	-62.353	-3.933	76.855	83.310	6.350
48	-2.583	55.837	76.260	82.700	6.350

REFERENCES

1. S. Hahn, Thesis, University of Illinois, 1983
2. J.J. Aubert et al, Phys. Rev. Lett. 33 1404 (1974)
3. J.E. Augustin et al, Phys. Rev. Lett. 33 1406 (1974)
4. S.D. Drell and T.M. Yan, Annals of Physics 66,578 (1974)
5. D. Sivers, Nuc. Phys. B106, 95 (1976)
6. K.J. Anderson et al Phys. Rev. D21, 3075 (1980)
7. M. Binkley et al, Phys. Rev. Lett. 37, 578 (1976)
8. S. Zaninotte et al, Proceedings of 15 Moriond Conf. (1980)
9. A. Donnachie and P.V. Landshoff, Nuc. Phys. B112, 223 (1976)
10. S. Nandi and H.R. Schneider, Phys. Rev. D18, 756(1978)
11. A.S. Ito et al, Phys. Rev. D23, 604 (1981)
12. J. Badier et al, Phys. Lett. 89B, 145 (1979)
13. J.J. Aubert et al, CERN preprint CERN-EP/81-161
14. M. Gluck and E. Reya, Phys. Lett. 83B 98 (1979)
15. C.O. Escobar et al, Preprint CBPF-NF-032J (1980)
16. Y. Kinoshita and K. Kinoshita, Preprint BI-TP 77/11 (1977)
17. J.C. Collins and D.E. Soper, Phys. Rev. D16, 2219 (1981)
18. G.E. Hogan et al, Phys. Rev. Lett. 42,948 (1979)
19. Badier et al, Inter. Conf on H.E.P. Madison (1980)
20. C.E. Carlson and R. Suaya, Phys. Rev D14, 3115 (1976)
21. C.E. Carlson and R. Suaya, Phys. Rev D15, 1416 (1977)
22. M. Gluck et al, Phys Rev D17, 2324 (1978)
23. L.M. Jones and H.W. Wyld, Phys. Rev. D17, 1782 (1978)
24. V. Barger et al , Zeit. fur Phys. C6, 169 (1980)
25. M. Gluck and E. Reya, Phys. Lett. B72, 326(1978)
26. G.R. Farrar, Nuc. Phys. B77, 429 (1974)

27. V. Barger and R.J.N. Phillips, Nucl. Phys. B73, 269 (1974)

28. I.R. Kenyon, Rep. Prog. Phys. 45, 1261 (1982)

29. G. Matthiae, Rivista del Nuovo Cimento 4, 3(1981)

30. W. Aithenhead et al, Phys. Rev. Let. 45, 157 (1980)

31. K.W. Lai and R.L. Thews, Phys. Rev. Let. 44 1731 (1980)

32. T. Weiler, Phys. Rev. Let. 44 304 (1980)

33. K.J. Anderson et al, Phys. Rev. Lett. 42 944 (1979)

34. B. Cox, XXI Inter. Conf on H.E.P. at Paris (1982)

35. V. Cerny et al, Phys. Let. 76B 645 (1980)

36. P. Schoessow, Thesis, Univerity of Illinois, 1983

37. M. Atac et al, Nucl. Inst. Meth. 140 461 (1977)

38. M. Atac and J. Urish, Nucl. Inst. Meth. 156 163 (1978)

39. C.J. Maxwell and M.J. Teper, Z. Physik C 7, 295 (1981)

40. B. Pietrzyk et al, Phys. Lett. 113B 105 (1982)

41. Ph. Charpentier, Proceeding of 18 Moriond Conf. (1983)

42. D.W. Duke and M.J. Teper, Nuc. Phys. B166 84 (1980)

43. S. Pordes, Thesis, Harvard University, 1976.

44. F. Sauli, CERN preprint CERN 77-09, (1977)

45. G. Charpak et al, Nucl Instr and Meth 97, 377(1971)

VITA

Howard S. Budd graduated from Pennsylvania State University in 1971 with a Bachelor of Science degree in both mathematics and physics. In 1972 he received a Master of Science degree in mathematics at the University of Illinois. He has held teaching assistantships in the mathematics and physics departments and research assistantships in the physics department at the University of Illinois.